NTNU

Norwegian University of
Science and Technology

Experimental and Numerical Studies of Plain and Reinforced Concrete Plates Subjected to Blast Loading

Eivind Hillestad

Jon Eide Pettersen

Master of Science in Mechanical Engineering
Submission date: June 2016
Supervisor: Tore Børvik, KT
Co-supervisor: Martin Kristoffersen, KT

Norwegian University of Science and Technology
Department of Structural Engineering

Department of Structural Engineering
Faculty of Engineering Science and Technology
NTNU- Norwegian University of Science and Technology

ACCESSIBILITY

OPEN

MASTER THESIS 2016

SUBJECT AREA:	DATE:	NO. OF PAGES:
Computational Mechanics	10.06.2016	18 + 158 + 20

TITLE:

Experimental and Numerical Studies of Plain and Reinforced Concrete Plates Subjected to Blast Loading

Eksperimentelle og numeriske studier av armerte og uarmerte betongplater utsatt for eksplosjonslast

BY:

Eivind Hillestad and
Jon Eide Pettersen

SUMMARY:
The main objective in this thesis was to determine how the behavior of concrete structures subjected to blast loads may be predicted. An experimental study was conducted, in which 50 mm thick plain and reinforced concrete plates were subjected to blast loading in the SIMLab shock tube facility at NTNU. An attempt was made to replicate the shock tube experiments in finite element simulations using the Karagozian and Case Concrete Damage Model (K&C) in LS-DYNA, and the Concrete Damaged Plasticity Model (CDP) in Abaqus.

The mechanical and stochastic properties of the concrete were found through material testing, and the K&C and CDP models were calibrated by inverse-modelling the material tests. Two stochastic methods, dubbed the random element strength and the mesoscale methods, were developed and employed in the simulations in an attempt to recreate the stochastic behavior of concrete. They were both able to capture the variation in compression strength that was observed in the cube compression tests, and the mesoscale method also produced highly erratic and realistic crack patterns.

The numerical simulations revealed that the K&C and CDP models were capable of predicting crack patterns that correlated reasonably well with the results from the shock tube experiments. However, it was generally seen that the extent of cracking was overestimated in both models, and the simulated displacement histories were not in perfect correlation with observations from the experiments. Introducing random element strength into the plate simulations caused little change in the simulated displacement history. However, the crack patterns became more irregular, and were thus in closer agreement with some of the real crack patterns. Furthermore, employing the mesoscale method caused a reduction in the predicted plate capacity, but the results were considered to be promising due to the highly irregular crack patterns and realistic modes of fracture predicted by the method.

RESPONSIBLE TEACHER: Professor Tore Børvik

SUPERVISOR(S): Professor Tore Børvik and Postdoc Martin Kristoffersen

CARRIED OUT AT: SIMLab, The Department of Structural Engineering, NTNU

Institutt for konstruksjonsteknikk
Fakultet for ingeniørvitenskap og teknologi
NTNU- Norges teknisk- naturvitenskapelige universitet

TILGJENGELIGHET

ÅPEN

MASTEROPPGAVE 2016

FAGOMRÅDE:	DATO:	ANTALL SIDER:
Beregningsmekanikk	10.06.2016	18 + 158 + 20

TITTEL:

Eksperimentelle og numeriske studier av armerte og uarmerte betongplater utsatt for eksplosjonslast

Experimental and Numerical Studies of Plain and Reinforced Concrete Plates Subjected to Blast loading

UTFØRT AV:

Eivind Hillestad og
Jon Eide Pettersen

SAMMENDRAG:
Hovedmålet med denne avhandlingen var å fastlå hvordan oppførselen til betongstrukturer utsatt for eksplosjonslast kan beregnes. Det ble utført eksperimenter i shocktuben til SIMLab ved NTNU, hvor 50 mm tykke uarmerte og armerte betongplater ble utsatt for eksplosjonslast. Det ble forsøkt å gjenskape eksperimentene i simuleringer med elementmetoden, og i den anledning ble to materialmodeller undersøkt: Karagozian & Case Concrete Damage-modellen (K&C) i LS-DYNA, og Concrete Damaged Plasticity-modellen (CDP) i Abaqus.

De mekaniske og stokastiske egenskapene til betongen ble fastslått ved hjelp av materialtester, og K&C og CDP modellene ble kalibrert ved å inversmodellere testene. Det ble forsøkt å gjenskape den tilfeldige oppførselen til betong i simuleringene ved å implementere to forskjellige stokastiske metoder; en mesoskalametode og en metode med tilfeldig elementstyrke. Begge metodene klarte å fange variasjonen i trykkfasthet som ble observert i terningtrykk-testene, og mesoskalamodellen produserte dessuten tilfeldig orienterte og realistiske sprekkmønstre.

Elementanalysene viste at begge materialmodellene var i stand til å forutse sprekkmønstre som stemte godt overens med de mønstrene som ble dannet i eksperimentene i shocktuben. Derimot var det tydelig at mengden sprekker ble overestimert i begge modellene, og det ble observert at det simulerte forskyvningsforløpet ikke korrelerte perfekt med de eksperimentelle målingene. Det ble ikke observert en signifikant endring i forskyvningsforløpet til platene når tilfeldig elementstyrke ble tatt med i analysene, men sprekkdannelsen ble mer vilkårlig, og simuleringene stemte dermed kvalitativt bedre overens med responsen i flere av testplatene. Mesoskalamodellen predikerte lavere kapasitet i platene enn hva som ble observert i eksperimentene, men resultatene ble likevel ansett som lovende ettersom intrikate sprekkmønstre og kvalitativt realistiske bruddtilstander ble gjenskapt av metoden.

FAGLÆRER: Professor Tore Børvik

VEILEDER(E): Professor Tore Børvik og Postdoktor Martin Kristoffersen

UTFØRT VED: SIMLab, Institutt for konstruksjonsteknikk, NTNU

Department of Structural Engineering
FACULTY OF ENGINEERING SCIENCE AND TECHNOLOGY
NTNU – Norwegian University of Science and Technology

MASTER'S THESIS 2016

for

Eivind Hillestad and Jon Eide Pettersen

Experimental and Numerical Studies of Plain and Reinforced Concrete Plates Subjected to Blast Loading

1. INTRODUCTION

Protection of engineering structures against blast loading has received a lot of attention in recent years. The newly proposed coastal highway route E39 seeks to connect Trondheim to Kristiansand along the coast without using any ferry connections. One of several critical points is the crossing of the Sognefjord, where a submerged floating tunnel has been suggested as a means of crossing. Internal blast loading (due to e.g. an accident or a terrorist attack) of a structure like this can be extremely critical, and it is important to verify that the structure is able to withstand a realistic blast load, or at least minimise the damage as a breach could have disastrous consequences. Reinforced concrete will most likely be used for this construction due to the scale of the structure. Also, more or less any cross-sectional profile may be cast in concrete and can easily be adjusted to the correct buoyancy. Computational methods are now available to predict both the loading and structural response in these extreme loading situations, and experimental validation of such methods is necessary in the development of safe and cost-effective structures. In this study blast experiments will be performed, and the data will be used for validation and verification of some frequently used computational methods involving blast loading.

2. OBJECTIVES

The main objective of the research project is to determine how plain and reinforced concrete plates behave under blast loading, and to validate to which extent this can be predicted using computational tools.

3. A SHORT DESCRIPTION OF THE RESEARCH PROJECT

The main topics in the research project will be as follows;

1. A comprehensive literature review should be conducted to understand the blast load phenomenon, blast load design, shock tube facilities, constitutive and failure modelling of concrete materials exposed to extreme loadings, and explicit finite element methods.
2. Casting of reinforced and plain concrete plates of 50 mm thickness and of a specified material quality (B20) and accompanying material tests (cylindrical and cubic compression tests).
3. Proper constitutive relations and failure criteria are chosen and calibrated based on the material tests.
4. Experimental work on components:
    a. The SIMLab Shock Tube Facility will be used to expose the plates to simulated blast loading, as opposed to explosive detonations. The shock tube experiments will be used to investigate typical dynamic responses and failure modes of plated structures exposed to blast loading.
5. Digital Image Correlation (DIC) will be used to measure the 3D transverse displacement fields of the plates in the shock tube experiments.
6. Non-linear FE numerical simulations of the shock tube and field experiments will be performed, and the numerical results shall be compared and discussed based on the experimental findings.

Supervisors: Tore Børvik (NTNU), Martin Kristoffersen (NTNU)

The thesis must be written according to current requirements and submitted to the Department of Structural Engineering, NTNU, no later than June 11th, 2015.

NTNU, January 15th, 2016

Tore Børvik
Professor

Acknowledgements

This thesis has been written during the spring semester of 2016 at SIMLab/SFI-CASA at the Department of Structural Engineering with Professor Tore Børvik and Postdoc Martin Kristoffersen as supervisors. Steady progress has been facilitated by weekly meetings with the supervisors, and their support, guidance and encouragements during the process is greatly appreciated by the authors.

As novices in the field of concrete, the authors wish to thank Engineers Steinar Seehus and Gøran Loraas for great assistance and instructions during production of the concrete plates. Sincere gratitude is also directed towards Senior Engineer Trond Auestad, who directed the shock tube experiments with a steady hand and conducted the tensile testing of the rebar material.

Thanks to Dr. David Morin for invaluable help with creating the Abaqus subroutine and PhD candicates Lars Edvard Dæhli and Joakim Johnsen for getting it to work properly. We also wish to express gratitude towards Dr. Torodd Berstad for help with the analyses in LS-DYNA.

Vegard Aune and Egil Fagerholt were helpful with calibrating and running the DIC analyses, and for this we are grateful.

Finally, we wish to thank the ferry-free E39 project and SFI-CASA for financing the concrete specimens and the shock tube experiments.

10/06/2016, Trondheim, Norway

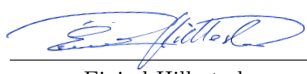

Eivind Hillestad

Jon Eide Pettersen

Abstract

The main objective in this thesis was to determine how the behavior of concrete structures subjected to blast loads may be predicted. An experimental study was conducted, in which 50 mm thick plain and reinforced concrete plates were subjected to blast loading in the SIMLab shock tube facility at NTNU. An attempt was made to replicate the shock tube experiments in finite element simulations using the Karagozian and Case Concrete Damage Model (K&C) in LS-DYNA, and the Concrete Damaged Plasticity Model (CDP) in Abaqus.

The mechanical and stochastic properties of the concrete were found through material testing, and the K&C and CDP models were calibrated by inverse-modelling the material tests. Two stochastic methods, dubbed the random element strength and the mesoscale methods, were developed and employed in the simulations in an attempt to recreate the stochastic behavior of concrete. They were both able to capture the variation in compression strength that was observed in the cube compression tests, and the mesoscale method also produced highly erratic and realistic crack patterns.

The numerical simulations revealed that the K&C and CDP models were capable of predicting crack patterns that correlated reasonably well with the results from the shock tube experiments. However, it was generally seen that the extent of cracking was overestimated in both models, and the simulated displacement histories were not in perfect correlation with observations from the experiments. Introducing random element strength into the plate simulations caused little change in the simulated displacement history. However, the crack patterns became more irregular, and were thus in closer agreement with some of the real crack patterns. Furthermore, employing the mesoscale method caused a reduction in the predicted plate capacity, but the results were considered to be promising due to the highly irregular crack patterns and realistic modes of fracture predicted by the method.

Table of Contents

Nomenclature

Abbreviations

1D, 2D, 3D	=	One, two and three-dimensional
3pt	=	Three-point (bending)
Bij	=	Concrete of ij MPa nominal compressive strength
BC	=	Boundary Condition
C3D4	=	4-node linear tetradron element
C3D8R	=	8-node linear brick element with reduced integration
C-4	=	Plastic explosive
CT	=	X-ray Computed Tomography
CASA	=	Centre for Advanced Structural Analysis
CDF	=	Cumulative Density Function
CDP	=	The Concrete Damaged Plasticity Model
CLIS	=	Constrained Lagrange in Solid
CPU	=	Central Processing Unit
DIC	=	Digital Image Correlation
DIF	=	Dynamic Increase Factor
DOF	=	Degree of Freedom
DPDC	=	Dynamic Plastic Damage Concrete material model
FEA	=	Finite Element Analysis
FEM	=	Finite Element Method
FPZ	=	Fracture Process Zone
FSI	=	Fluid-structure interaction
HCP	=	Hydrated Cement Paste
HJC	=	Holquist-Johnson-Cook material model
K&C	=	Karagozian & Case material model
LEFM	=	Linear Elastic Fracture Mechanics
NS	=	Norwegian Standard
NTNU	=	Norwegian University of Science and Technology
P-ij	=	Plain plate tested at driver pressure of ij bar
PDF	=	Probability Density Function
P-I	=	Pressure-Impulse
PMMA	=	Poly(methyl methacrylate) (polymer)
R-ij	=	Reinforced plate tested at driver pressure of ij bar
RHT	=	The Riedel-Hiermaier-Thoma Model
SIMLab	=	Structural Impact Laboratory at NTNU
SFI	=	Centre for Research-based Innovation
SFT	=	Submerged Floating Tunnel
SF	=	Scaling Factor
SDOF	=	Single Degree of Freedom
TNT	=	Trinitrotoluene (explosive)

Roman letters

A	=	Area
A_s	=	Cross-sectional area of rebar
a	=	Width of plate
$\bar{A}$	=	Power law hardening constant
a_{0y}, a_{1y}, a_{2y}	=	K&C yield surface constants
a_0, a_1, a_2	=	K&C maximum stress surface constants
a_{1f}, a_{2f}	=	K&C residual stress surface constants
a_r	=	Reduced side dimension
B	=	Depth of beam
$\bar{B}$	=	Power law hardening constant
b	=	Depth of plate
b'	=	Friedlander decay coefficient
b_r	=	Reduced side dimension
$\boldsymbol{C}$	=	Damping matrix
c_d	=	Dilatation wave speed
$\boldsymbol{D}$	=	Degree of freedom vector
D	=	Plate stiffness
D'	=	Reinforced plate stiffness
D_c	=	Diameter of cylinder
D_r	=	Equivalent plate stiffness of rebar
D_{max}	=	Maximum aggregate diameter
D_{min}	=	Minimum aggregate diameter
d	=	Damage indicator
d'	=	Distance from plate surface to rebar
d_r	=	Rebar wire diameter
E	=	Elastic modulus
E_c	=	Elastic modulus of concrete
E_s	=	Elastic modulus of steel
Ef	=	Frictional energy
Ei	=	Internal energy
Ek	=	Kinetic energy
Ev	=	Viscous energy
(E)	=	Rarefaction wave
F	=	Force
$f(\boldsymbol{\sigma}, R(p))$	=	Yield function
f	=	Coefficient of friction
f_c	=	Compressive strength
f_t	=	Tensile strength
$\bar{f}(x)$	=	The probability of something being x
$\bar{F}(x)$	=	The probability of something being less or equal to x
g	=	Plastic potential function
h	=	Thickness
h_e	=	Smallest element length
h_r	=	Linear plastic hardening modulus
$h_{r,eq}$	=	Rebar equivalent plate thickness
I	=	Second moment of area
i	=	Plate boundary fixity ratio
i_{r+}	=	Specific positive impulse
J_2	=	Second deviatoric stress invariant
$\boldsymbol{K}$	=	Stiffness matrix
K	=	SDOF equivalent stiffness
L	=	Length
l	=	Distance from midplane of plate to rebar
L_e	=	Characteristic element length
$\boldsymbol{M}$	=	Mass matrix

M	=	Moment
M_e	=	SDOF equivalent mass
m_p	=	Plastic moment capacity
n	=	Number of samples in a set
$\bar{n}$	=	Power law hardening exponent
P	=	Pressure
P_a	=	Atmospheric pressure
P_f	=	Shock tube firing pressure
P_r	=	Peak reflected pressure
P_{so}	=	Peak incident pressure
P_u	=	Ultimate pressure load capacity
p	=	Hydrostatic pressure
$\bar{p}$	=	Effective hydrostatic pressure
$\bar{q}$	=	von Mises equivalent stress
q_0	=	Static pressure load
R, R_1	=	Stand-off distance
$R(p)$	=	Hardening function
$\boldsymbol{R}^{ext}$	=	External force vector
r_f	=	Rate enhancement factor
T	=	Natural vibration period
T'	=	Tensile force in rebar
t	=	Time
t_+	=	Positive impulse duration
t_-	=	Negative impulse duration
t_d	=	Dynamic load duration
t_n, t_{n+1}	=	Time step n and $n+1$
U, U_1	=	Detonation energy
W, W_1	=	TNT-equivalent mass
$w(x, y)$	=	Transverse deformation field
w_e	=	Midpoint displacement
w_{mn}	=	Plate displacement field coefficients
x_i	=	Value of sample i
Z	=	Scaled distance
Z'	=	Equivalent plastic moment arm

Greek letters

α	=	Pressure sensitivity constant
β	=	Yield surface shape function (CDP-model)
γ	=	Yield surface shape constant
Δt	=	Time increment
Δt_{cr}	=	Critical time step
σ_{ij}	=	Stress component $i\ j$
$\Delta\sigma$	=	The von Mises yield function
$\Delta\sigma_m$	=	Ultimate stress
$\Delta\sigma_r$	=	Residual stress
$\Delta\sigma_y$	=	Yield stress
$\boldsymbol{\varepsilon}$	=	Strain matrix
ε_{ij}	=	Strain component $i\ j$
ε	=	Total strain
ε^e	=	Elastic strain
ε^p	=	Plastic strain
ε_v	=	Volumetric strain
$\bar{\varepsilon^p}$	=	Equivalent plastic strain

$\tilde{\varepsilon}_c^{pl}$	=	Compressive equivalent plastic strain
$\tilde{\varepsilon}_t^{pl}$	=	Tensile equivalent plastic strain
$\eta(\lambda)$	=	Damage function in K&C-model
θ_p	=	Principal stress direction
λ	=	Blast scaling parameter
$\dot{\lambda}$	=	The plastic parameter
$\bar{\mu}$	=	Mean value
μ_f	=	Average cube compression strength
μ_i	=	Average element compression strength
μ_i^T	=	Average element tensile strength
ν	=	Possion's ratio
ρ	=	Mass density
$\boldsymbol{\sigma}$	=	Stress matrix
σ_0	=	Yield stress
$\sigma_{1,2}$	=	1st and 2nd principal stress
σ_c	=	Compressive stress
σ_{eq}	=	Equivalent stress
σ_i	=	Standard deviation in element compression strength
σ_i^T	=	Standard deviation in element tensile strength
σ_f	=	Standard deviation in cube compression strength
σ_Y	=	Flow stress
$\bar{\boldsymbol{\sigma}}$	=	Effective stress matrix
$\hat{\bar{\sigma}}_{max}$	=	Maximum principal effective stress
$\bar{\sigma}$	=	Standard deviation
τ_{xy}	=	In-plane shear stress
$\phi(\boldsymbol{\sigma})$	=	Equivalent stress function

Chapter 1

Introduction

In 2013, the Norwegian government announced that within 20 years, the coastal highway route (E39) should be rid of its seven ferry connections [1]. The alternatives to ferry connections have traditionally been bridges and subsea rock tunnels, however several of the mighty fjords along the Norwegian coast present significant challenges to these existing alternatives. With its 4 km width and depth of nearly 1300 meters, Norway's biggest fjord, the Sognefjord, is considered to be one of the most difficult crossing points along the entire coastal route. It is simply too deep and wide for traditional crossing alternatives to be feasible, hence several new concepts and solutions are currently in development. One such concept, which never before has been realized, is the submerged floating tunnel (SFT).

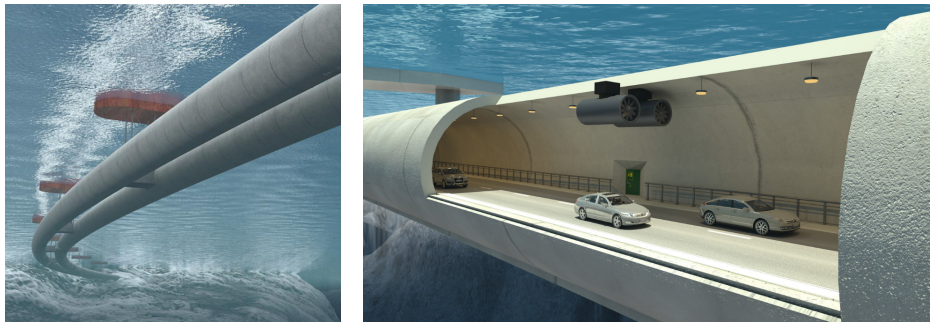

(a) ***(b)***

Figure 1.1: *Illustrations of what a submerged floating tunnel might look like in (a), and its cross section in (b) [2].*

As illustrated in Figure 1.1, the SFT is a long and slender concrete structure that floats under water. A major uncertainty associated with such a design is the structural response in the case of a critical event, such as an internal explosion.

Recent events exemplify this, as in 2015 when a tank truck containing over 16000 liters of petrol accidentally exploded inside a subsea rock tunnel in Bremanger, Norway. The tunnel suffered great damage, and was partly flooded with water [3]. Moreover, terrorist attacks serve as an additional reminder of how devastating a blast load scenario can become in account of the loss of civilian lives and structural failure. If a powerful internal explosion, be it accidental like the one in Bremanger or a terrorist attack, were to take place inside an SFT, the consequences could be disastrous. Thus, it is of great importance to take this into account during the structural design of an SFT.

This thesis builds on the preceding Master's thesis by Haug and Osnes in 2015 [4], and revolves around the behavior of concrete plates subjected to blast loading. The main objective is to determine how well blast load induced damage in concrete structures can be predicted using numerical methods. Since full scale or even scaled testing of concrete structures is a costly affair, the only realistic alternative to assessing the blast response of large concrete structures is through numerical simulations.

Concrete is a brittle, pressure dependent and rate dependent material, making it challenging to model. There are several material models available for concrete, but with an exceeding amount of material constants as the complexity of the model increases. Calibration of concrete models can therefore be difficult, and the effect of changing different parameters may not always be obvious. Consequently, there are numerous uncertainties regarding blast simulations of concrete. In their work, Haug and Osnes found that the well-known Holmquist-Johnson-Cook (HJC) model required an enormous amount of tuning, and struggled to get reasonable results from the model. They did, however, obtain promising results with the Karagozian and Case (K&C) model available in the commercial software LS-DYNA, and recommended it for further assessment. Finally, they concluded that material models for concrete are not as mature and reliable as constitutive relations for metallic materials.

Motivated by the findings of Haug and Osnes, the K&C model will be thoroughly investigated in this thesis. An additional material model, namely the CDP model in the commercial software Abaqus, will also be studied. Since there is a certain randomness to the nature of concrete, stochastic methods are developed and employed in several of the simulations. In terms of experiments, the SIMLab Shock Tube Facility provides a safe alternative to explosive detonations, and will thus be used for experimental testing of reinforced and plain concrete plates. Moreover, in order to achieve better basis for comparison between the experimental results and the simulations, Digital Image Correlation (DIC) will be employed to measure the deformation of the plates during testing. Although flat concrete plates subjected to blast loads in a shock tube represents a simplification of almost any realistic explosion scenario, it serves as a great way to validate the numerical models. If a numerical model is incapable of recreating the results from the shock tube experiments, there is no reason to believe that it should be accurate in more complex problems, such as an explosion inside an SFT.

Finally it should be noted that the work presented within this thesis is the authors' first encounter with concrete as an engineering material. Consequently, the convoluted subtleties involved in the design and manufacturing of concrete are not accounted for in this thesis, and the treatment of concrete is thus purely phenomenological.

An overview of the different chapters in this thesis is presented below.

Chapter 2 - Literature Review: A brief overview of related experimental and numerical studies on concrete subjected to explosions will be given. Furthermore, the most central findings from the preceding Master's thesis by Haug and Osnes is presented.

Chapter 3 - Background Theory: Relevant background theory for this thesis will be discussed in brief. This includes an introduction to blast theory, the SIMLab shock tube, structural response to blast loads, finite element analysis and solvers, material mechanics and finally some statistics.

Chapter 4 - Concrete: A detailed presentation of concrete will be given, with an emphasis on the internal structure and mechanical properties. Furthermore, typical failure modes for concrete plates and the size effect in concrete is discussed, before the material models employed in this thesis are presented.

Chapter 5 - Introductory Experimental Work: This chapter documents the introductory experimental work carried out prior to the blast experiments. It includes the casting of concrete test specimens and plates, testing of the fresh concrete mix and material testing of the cured concrete specimens. Finally, the rebar steel is tested in uniaxial tension, and two material models for the steel are calibrated and validated.

Chapter 6 - Shock Tube Experiments: Blast experiments on four concrete plates are performed in the SIMLab shock tube facility, whereof two are reinforced and two are plain. Finally, the results are discussed.

Chapter 7 - Preliminary Analysis: Analytical calculations of plates subjected to pressure loading are performed, and the boundary conditions in the shock tube assembly are studied. Next, the material tests are simulated in both Abaqus and LS-DYNA, and the simulations are compared with the experimental results from Chapter 5. In the following, two stochastic methods are developed and studied in further detail. The results are summarized and discussed lastly.

Chapter 8 - Simulations of Concrete Plates in Abaqus: The shock tube experiments are attempted recreated in Abaqus. Mesh effects, the performance of element erosion and the effects of employing one of the stochastic methods will be studied in detail. Finally, the results are summarized and discussed.

Chapter 9 - Simulations of Concrete Plates in LS-DYNA: The shock tube experiments are attempted recreated in LS-DYNA. Mesh effects, strain rate dependence and both stochastic methods will be studied in detail. Finally, the results are summarized and discussed.

Chapter 10 - Capacity Study: The plate capacity predicted by the Abaqus and LS-DYNA models is studied in closer detail. The effect of impulse is also investigated.

Chapter 12 - Concluding Remarks: A summary of results and conclusions is given.

Chapter 13 - Further Work: Topics for further work are suggested.

Chapter 2

Literature Review

Due to its low cost and high strength, concrete has been widely used for protective structures throughout history. Consequently, a lot of work has been done to assess the performance of concrete subjected to explosions, projectiles, warheads and other weapons. The advent of advanced numerical simulation tools has also made it possible to recreate the behavior of concrete structures in a simulation, and considerable effort has therefore gone into the development of reliable material models for concrete. In the following, a handful of some of the recent experimental and numerical studies on concrete subjected to explosions will be given.

2.1 Related research

In 1995, Toutlemonde et al. [5] subjected circular, simply supported plates to quasi-static and dynamic pressure using a shock tube, and found that the failure load was higher when the load was dynamic. Woodson and Baylot [6] conducted four experiments in 1999, where they subjected a two-story quarter-scale concrete building to a 15.625 lbs (7.087 kg) C-4 charge at a stand-off distance of 3.5 ft (1.07 m). Different arrangements of wall cladding was used for the different tests to study how the structural response of the building was affected. Eulerian finite volume simulations were performed to determine the loading on the structure, and the response was subsequently simulated in the finite element code DYNA3D.

Magnusson and Hallgren [7] subjected high strength reinforced concrete beams to shock waves generated by an explosive charge inside a shock tube, and compared the dynamic response with quasi-static tests. In [8], Magnusson constructed Single Degree of Freedom (SDOF) models of the beams and obtained good correlation with the experiments.

In 2008, Schenker et al. [9] studied the effect of adding aluminium foam to mitigate blast loads on concrete plates. They detonated hemispherical surface charges of

1000 kg TNT at a standoff distance of 20 m to two reinforced concrete plates, one of which was fitted with aluminium foam panels. Two such tests were performed, one with high strength concrete (B100) and one with regular concrete (B30). Thiagarajan et al. [10] subjected simply supported, reinforced 1652×857×101.6 mm slabs to shock waves using a large shock tube. The response of the plates was simulated in LS-DYNA using the Winfrith and K&C concrete models, and it was concluded that both models performed reasonably well at predicting the deflection histories of the slabs.

Wang et al. [11] performed an experimental and numerical study of simply supported reinforced concrete plates under close-in explosions in 2013. 1000×1000×40 mm plates were subjected to blasts from TNT-charges of 0.2-0.53 kg at a stand-off distance of 400 mm, and the concrete that was used had a compression strength of 39.5 MPa. The Riedel-Hiermaier-Thoma (RHT) material model was used to model the response of the concrete. Li and Hao [12] later used the experiments by Wang et al. to calibrate the K&C concrete model in LS-DYNA to study spalling in reinforced concrete columns.

2.2 Master thesis from 2015

In 2015, Haug and Osnes [4] conducted five shock tube experiments on 50 mm thick concrete plates in the SIMLab shock tube facility. They used concrete of approximately 55 MPa uniaxial compressive strength and 4.14 MPa average tensile splitting strength. Of the five plates, two developed significant damage from the experiments. One plate was also perforated by projectiles prior to loading in order to study the effect of initial damage to the plate. A summary of the experiments is shown in Table 2.1.

Plate nr.	*Peak pressure* [bar]	*Damage*
1	7.4	Only minor surface cracks.
2	7, 11.99 & 12	Was subjected to three blasts, only surface cracks appeared.
3	6.62	Was first perforated by four 7.62 mm bullets before the blast. No additional damage appeared.
4	29*	Complete failure.
5	18.78	Deep cracks through the thickness.

*The pressure curve in this experiment experienced strong secondary reflections and did not resemble a Friedlander curve.

Table 2.1: *Tests performed by Haug and Osnes in 2015.*

Figure 2.1 shows plate 1, 2 and 5 after the experiments. The left, vertical crack of plate 1 developed during tightening of the bolts that clamped the plate to the shock tube, and only minor additional surface cracks appeared during the blast.

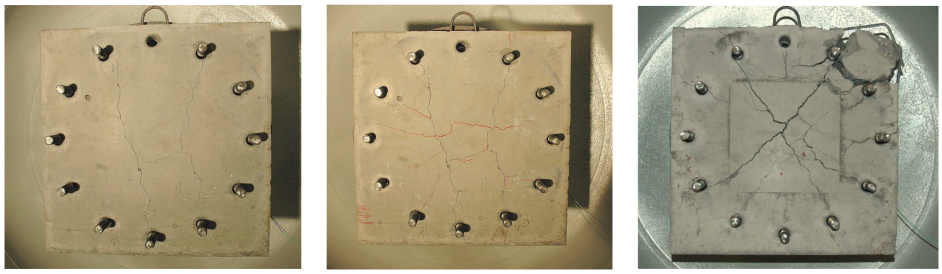

(a) Plate 1 ***(b)*** Plate 2 ***(c)*** Plate 5

Figure 2.1: *Plate 1, 2 and 5 after testing in the shock tube.*

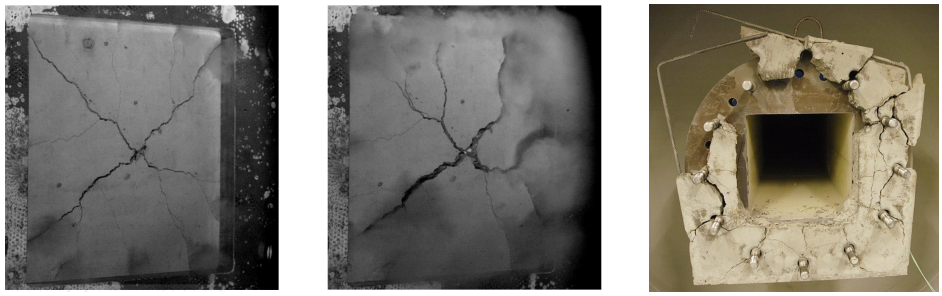

(a) 7.71 ms ***(b)*** 12.63 ms ***(c)*** After test

Figure 2.2: *Damage evolution of plate 4 during testing in the shock tube. It is seen that pressure escapes through the cracks once they penetrate the concrete plate.*

For plate 2, some superficial cracks appeared even though it was subjected to three blasts. In testing plate 4, significant damage was achieved. In this test, a shock tube driver length of 2 m was used in conjunction with a driver pressure of 78 bar, which resulted in a peak reflected pressure of 29 bar. The damage evolution of the plate is seen in Figure 2.2, and it can be seen that the plate was totally obliterated. For plate 5, the driver length was adjusted down to 0.77 m while using the same driver pressure as for plate 4, and this caused deep cracks in the plate.

The experiments were simulated by Finite Element Analysis (FEA) in IMPETUS, LS-DYNA and Europlexus, using the Holmquist-Johnson-Cook (HJC) model, the K&C Concrete Damage Model (CDM) and the Dynamic Plastic Damage Concrete (DPDC) model, respectively. They mainly focused on the HJC-model in IMPETUS, and found that the model required extensive tuning in order to produce results that were comparable to the experimental results. Even after tuning, the model overestimated the strength of the plates in most cases. The simulations in LS-DYNA with the K&C-model gave reasonable results without any tuning, and it was concluded that this model was the most promising for simulation of concrete plates subjected to blast loads.

Using Europlexus, Haug and Osnes also investigated the effect of fluid-structure interaction (FSI) for this particular problem. The DPDC-model was used to model the concrete for these simulations. While the simulations were able to capture some FSI-effects, they could not capture pressure loss from air leaking through the cracks of the plate. This behavior was observed in the experimental results. They suggested that refining the mesh and improving the boundary conditions may give better results, but conclude that this would be very comprehensive due to the high computational cost of the FSI-simulations.

In their thesis, Haug and Osnes suggest a number of areas in which further work could be performed, such as simulating the material tests to validate the numerical models or incorporating some sort of statistical distribution of strength into the simulations. Also, as simplified boundary conditions were employed in all of their simulations, Haug and Osnes emphasize that further work should include a more detailed study of the boundary conditions.

Chapter 3

Background Theory

In this chapter, some of the underlying theory for this thesis will be presented in brief. The purpose of this chapter is to introduce basic concepts that are essential to the understanding of the rest of this thesis. As some of these subjects are too comprehensive to be explained in detail, the reader will be referenced to more specific literature where applicable.

3.1 Blasts and explosions

The following section will briefly explain some of the basics of blast mechanics.

3.1.1 The formation of a shock wave

An explosion is defined as a sudden, almost instantaneous, release of energy. The source of this energy may be chemical or nuclear, as in the case of most bombs, or be caused by incidents such as a pressure vessel failure or even a meteor strike [13]. The energy is usually released in the form of high pressure and high temperature gases. Upon detonation, a disequilibrium forms between the high pressure gases in the detonation and the undisturbed air around it, causing the high pressure gas to expand rapidly.

In air, the speed of sound increases with increasing air pressure. Because the pressure in the detonation gases is high, the speed of sound will be higher in this region than in the surrounding air. Hence, the pressure waves inside the detonation gases will catch up with the surrounding air, causing a shock wave to form [14]. A shock wave is a sharp discontinuity that propagates through the air with a velocity greater than the speed of sound. For a charge that detonates in mid-air, the shock wave will propagate outwards in a spherical shape.

For a stationary object, an incoming shock wave will be experienced as a sharp increase in pressure followed by a gradual decline towards atmospheric pressure. In many cases, a negative pressure phase will follow the shock wave, causing the pressure to drop to less than atmospheric pressure before it returns to normal. At contact with an object, the shock wave will be reflected and amplified. It is the reflected wave that determines the loading on the object, and it is thus the magnitude of this wave that is most interesting when calculating the response of the object. The pressure-time relation for an incoming and reflected shock wave is depicted in Figure 3.1.

For engineering purposes the negative phase of the shock wave is often neglected, and the positive phase is idealized by the Friedlander curve. The Friedlander curve is expressed as

$$P(t) = P_a + P_r \left(1 - \frac{t}{t_+}\right) e^{\left(\frac{-b't}{t_+}\right)} \tag{3.1}$$

where P_a is the ambient pressure, P_r is the peak reflected pressure and b is the decay coefficient. Both the magnitude and duration of the shock wave are important when evaluating the effect of the shock wave on a structure. A measure that takes both into account is the specific positive impulse, defined as the area under the reflected pressure curve in Figure 3.1, i.e.

$$i_{r+} = \int_{t_a}^{t_a+t_+} P_r(t)dt. \tag{3.2}$$

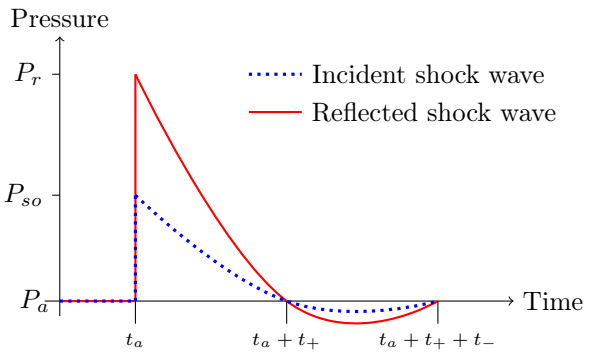

Figure 3.1: *Idealized shock wave, figure adopted from Aune et al. [13].*

3.1.2 Blast parameters

The strength of an explosion is determined by the amount of energy that is released in the detonation. For chemical explosives, the energy is determined by the heat of detonation of the explosive multiplied by the mass of the charge. The heat of detonation varies from explosive to explosive. TNT, for example, has a heat of

detonation of 4100-4900 kJ/kg, while C-4 is around 5860 kJ/kg. It is convenient to denote the charge size in TNT-equivalent mass. By this convention, 1 kg of C-4 is equivalent to around 1.4 kg TNT.

The strength of the shock wave diminishes with the cube of the distance from the charge. The distance from the charge to the position where the shock wave is measured is called the stand-off distance. With this in mind, it is possible to scale the shock wave parameters based on the stand-off distance and the size of the charge, so-called cube-root or Hopkinson-Crantz scaling. For a detonation of total energy U at a distance of R and another detonation of energy U_1 at distance R_1, the following relationship can thus be established [15]:

$$\frac{R}{R_1} = \left(\frac{U}{U_1}\right)^{\frac{1}{3}} \tag{3.3}$$

For chemical explosions, the TNT-equivalent mass W and W_1 may be used instead of the energy, and by setting W_1 equal to unity, a scaled distance Z and a scaling parameter λ can be introduced, i.e.,

$$Z = R_1 = \frac{R}{W^{\frac{1}{3}}} = \lambda R. \tag{3.4}$$

This means that the peak pressures obtained from a charge of weight W at distance R and a charge of weight $\lambda^3 W$ at distance λR will be the same, assuming that the blast environment is unchanged. The scaled distance Z is also often used to characterize the type of loading into close-in, near-field or far-field detonations. A close-in (or contact) detonation is characterized by very high pressure and short load duration, unevenly distributed over the structure. Such detonations lead to highly localized damage. A far-field detonation, on the other hand, features a plane shock wave and causes more global damage. A near-field detonation is somewhere in between, with non-uniform pressures and a mix of local and global damage. The different loading regimes are usually given by [13]:

$$\begin{aligned} Z &\leq 0.5 \quad \text{Close-in} \\ 0.5 < Z &\leq 2.0 \quad \text{Near-field} \\ Z &> 2.0 \quad \text{Far-field} \end{aligned}$$

In 1984, Kingery and Bulmash [16] conducted a study where they detonated a large number of charges of different sizes in air and on the ground, and measured the shock waves at different stand-off distances. From these measurements, empirical functions that relate the peak pressures, specific impulses and shock wave arrival times and velocities to the scaled distances were established. Using these relations, it is possible to calculate the resulting shock wave from a charge of known size and stand-off distance from a hemispherical (ground) charge or spherical (air) charge.

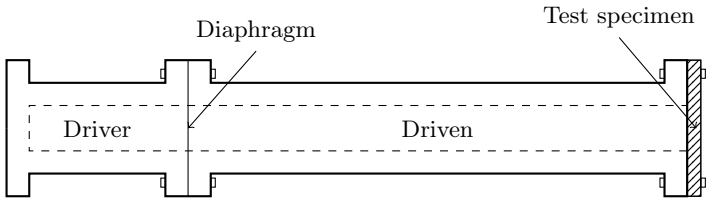

Figure 3.2: *Section view of an idealized shock tube.*

3.1.3 The shock tube

A shock tube is essentially a long, closed tube that is internally divided by a diaphragm, as illustrated in Figure 3.2. By pumping air into the driver section, energy is stored. When the pressure reaches a critical value, the diaphragm is removed and the energy is suddenly released. The sudden release of energy results in the formation of a shock wave that travels down the length of the tube and hits the test specimen that is mounted in the far end. The shock tube is sufficiently long that a plane shock front hits the test specimen, which replicates the shock wave generated in a far-field detonation [17]. Because of the inherent dangers and legislative issues of working with explosives, the shock tube is thus a very practical tool when investigating the effect of shock waves on structural elements. Also, the shock waves generated in a shock tube are repeatable and well understood from a theoretical standpoint, which is essential for scientific work.

Figure 3.3 shows how the pressure waves propagate inside a shock tube after detonation. At $t = 0$, the pressure in the driver is high and the pressure in the driven is low. Right after detonation, at $t = t_1$, the high pressure gas in the driver will cause a shock wave to travel down the tube towards the test specimen, while a rarefaction wave travels through the high pressure gas towards the left end of the shock tube. The rarefaction wave is then reflected and, if the driver is sufficiently short, catches up with the shock wave, causing the shock wave to decrease in strength and velocity and increase in duration [18]. Finally, the shock wave hits the test specimen and is reflected back towards the driver end. The contact surface in Figure 3.3 denotes the transition between the gas in the driver and the gas in the driven part of the shock tube. As seen from the figure, the shock wave initially travels faster than the contact surface before the rarefaction wave catches up.

For experiments where the rarefaction wave catches up with the incident shock wave, the reflected shock wave is often similar to the ideal shock wave in Figure 3.1, and may be accurately described by the Friedlander curve. For some combinations of driver length and driver pressure, however, the rarefaction wave does not catch up with the incident shock wave. In such cases, the reflected pressure consist of several peaks instead of one large peak. Aune et al. [18] conducted experiments in the shock tube facility at SIMLab, and found that the deviation between real shock tube behavior and ideal behavior increased with increasing driver pressure and volume. Further discussions on the ideal behavior versus the real behavior of

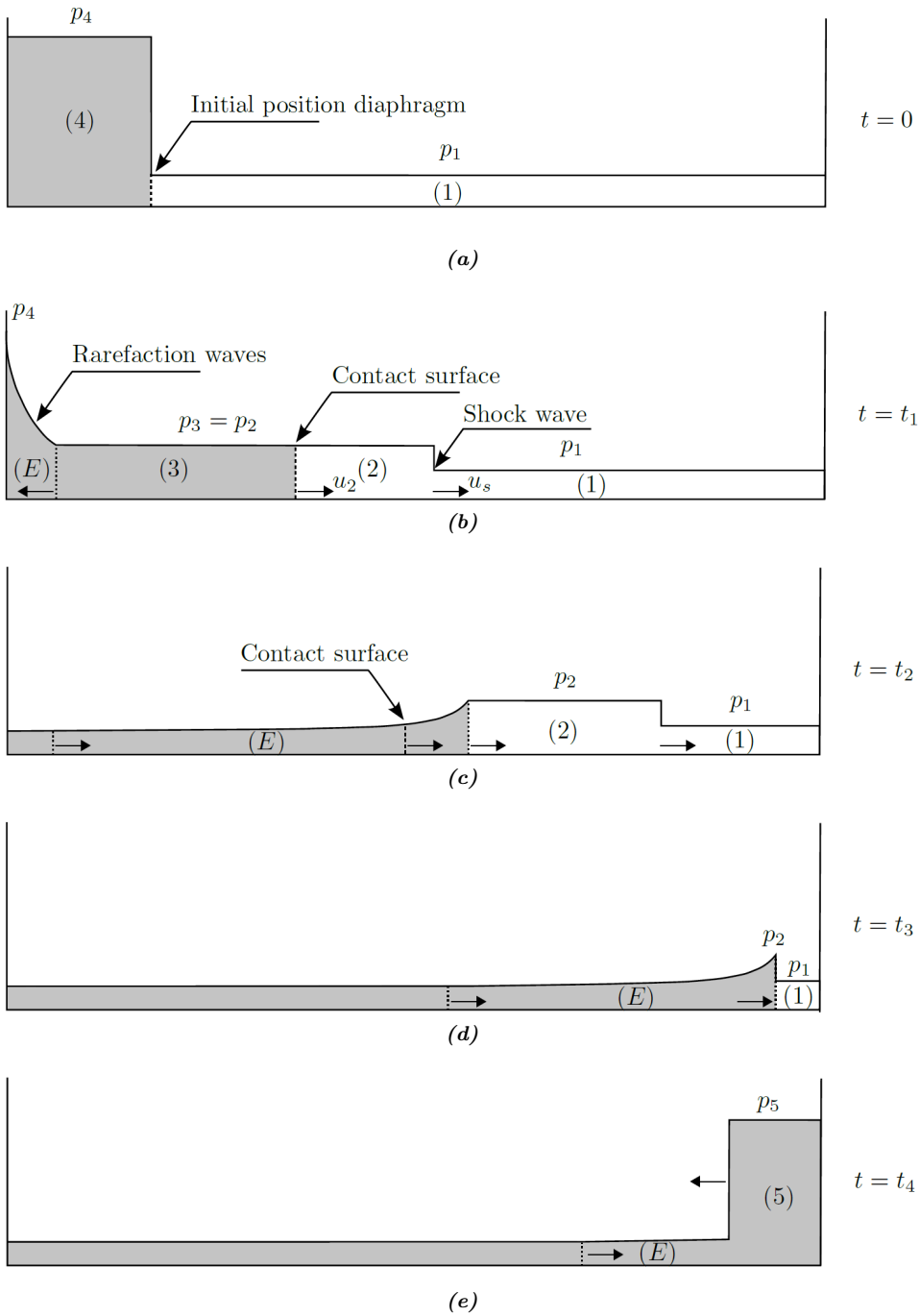

Figure 3.3: *Pressure distribution in shock tube from (a) right before detonation to (e) shock wave is reflected by target [18].*

the shock tube will follow in Chapter 6.

3.1.4 Structural response to blast loads

In the field of protective structure engineering, it is common to evaluate the structural response to blast loads by the use of Pressure-Impulse (P-I) diagrams. P-I, or iso-damage diagrams as they also are called, indicate the required combinations of load and impulse to achieve the same level of deformation (or damage) in a structure. An idealized P-I diagram is shown in Figure 3.4. The asymptotes indicate that the structural response can be divided into three parts; impulsive, quasi-static and dynamic. The P-I diagram shows that in the impulsive regime, the same amount of damage will be achieved for the same impulse, regardless of the magnitude of the pressure. Conversely, only the pressure determines the amount of damage in the quasi-static regime. In the dynamic regime, the response is highly dependent of the loading history [15].

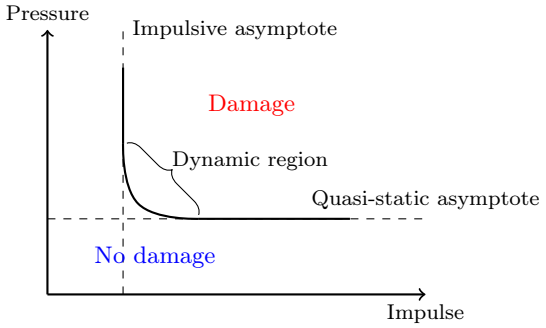

Figure 3.4: *Pressure-Impulse diagram, adopted from [15].*

An illustration of the loading regimes is given in Figure 3.5. For the impulsive case, the load acts in a much shorter time period than the deformation, meaning that the load is removed almost before the structure has time to respond. Since only the impulse determines the amount of deformation, the loading history does not influence the structural response in this region. In the quasi-static region, the load acts in a much longer time period than the displacement. Hence, only the magnitude of the load and stiffness of the structure determines the deformation. The dynamic region lies between the impulsive and quasi-static regions, and the response is more complex in this region, as it depends on both the load shape and load history.

From structural dynamics, it is known that there is a strong relationship between the natural frequency of a structure and its response to transient loads [15]. Therefore, the ratio of the load duration t_d and natural frequency period T is often used to categorize the loading regimes. Baker et al. [19] uses the following distinction:

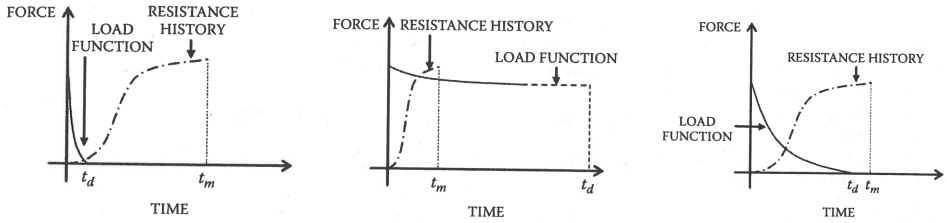

(a) Impulsive ***(b)*** Quasi-static ***(c)*** Dynamic

Figure 3.5: *Illustration of loading regimes for structures subjected to blast loads [15].*

$$\begin{aligned} \frac{t_d}{T} &< 0.0637 && \text{Impulsive} \\ 0.0637 < \frac{t_d}{T} &< 6.37 && \text{Dynamic} \\ \frac{t_d}{T} &> 6.37 && \text{Quasi-static} \end{aligned}$$

Haug and Osnes [4] performed single degree of freedom (SDOF) calculations on similar concrete plates as have been tested in this thesis, and concluded that the loading regime for the shock tube tests could be characterized as quasi-static. However, they assumed fully clamped boundary conditions and used a stronger concrete mix. As will be shown later, the clamped boundary condition assumption is too stiff, meaning that the calculated natural frequency period is probably a high estimate.

3.2 Finite Element Analysis

Finite element analysis (FEA) is perhaps the most important numerical tool for evaluating the response of a structure subjected to any kind of loading. For complex problems, it is not possible to use analytical methods, and the solution field must be approximated by means of discretization, i.e. splitting it into a finite number of elements. Elements are connected at locations called nodes, and the unknown values, e.g. displacements, are solved at these nodes. The behavior of each element is well-known, and is only governed by the displacements of the nodes.

In the following, a brief presentation of the aspects of FEA that are most relevant to this thesis will be given. See [20, 21] for further information regarding finite element analysis.

3.2.1 Nonlinear FEA

Concrete plates subjected to blast loading is a highly nonlinear problem. The material response is particularly nonlinear, with vast changes in stiffness occurring during deformation. Contact between the various parts in the shock tube clamping assembly introduces nonlinearities due to the opening and closing of gaps and sliding contact with frictional forces. Furthermore, deformations may be large enough to be considered nonlinear, i.e. equilibrium equations must be established with respect to the deformed geometry [20]. To account for nonlinearities such as these, nonlinear finite element analysis must be employed.

3.2.2 Explicit FEA

In nonlinear dynamic problems, direct integration of the equations of motion is required. The dynamic equation of motion can be written as

$$\boldsymbol{M}\ddot{\boldsymbol{D}} + \boldsymbol{C}\dot{\boldsymbol{D}} + \boldsymbol{K}\boldsymbol{D} = \boldsymbol{R}^{ext}, \tag{3.5}$$

where $\boldsymbol{M}$, $\boldsymbol{C}$ and $\boldsymbol{K}$ are the mass, damping and stiffness matrices respectively. $\boldsymbol{R}^{ext}$ is the external force vector and $\boldsymbol{D}$ is the vector containing the unknown degrees of freedom.

Two types of direct time integration schemes are available, and the one most suitable for wave propagation problems created by blast or impact loading is the explicit method [20]. All unknown quantities at time step t_{n+1} are obtained in terms of known quantities at time step t_n, therefore there is no need for equation solving in explicit FEA. Consequently, each time step is computationally inexpensive. However, as this method is only conditionally stable, very small time steps are required to ensure a stable solution. When damping is neglected, the maximum stable time increment Δt_{cr} is given by

$$\Delta t_{cr} = \frac{L_e}{c_d}, \tag{3.6}$$

where L_e is the characteristic length of the smallest element in the FE model, and the dilation wave speed c_d is given by

$$c_d = \sqrt{\frac{E}{\rho}}. \tag{3.7}$$

E and ρ are the stiffness and material density, respectively, and it is seen that altering either will change the stable time increment. Moreover, since the stable time increment is proportional to the characteristic element length, mesh refinement has adverse effects on the computational time in explicit FEA. That is, simulations become more demanding not only because of the increased number of elements, but

also due to the reduction in critical time increment size. Typically, in explicit finite element solvers a time step slightly below Δt_{cr} is employed to guarantee a stable solution.

Due to the large amount of time increments required, explicit finite element solvers often use reduced integration elements to reduce the computational time. When using reduced integration, the elements may exhibit spurious deformations, called zero energy or hourglass modes. This is usually dealt with by adding artificial resistance to the elements against hourglass modes, which may lead to energy being dissipated in unphysical phenomena. More importantly, this may be very difficult to detect due to dissipative processes like plastic deformation, making the solution appear reasonable despite being incorrect. This difficulty should be addressed by the analyst by performing an energy balance check [20].

3.2.3 Finite element solvers

In order to simulate blast loaded concrete plates, the finite element solver one wishes to employ must be capable of nonlinear analysis with explicit time integration. The two solvers used in this thesis, Abaqus and LS-DYNA, both meet this criterion.

Haug and Osnes [4] achieved promising results in their simulations on concrete plates in LS-DYNA. Moreover, several authors suggest in different articles that the LS-DYNA solver provides strong capabilities when it comes to blast loaded concrete [22–24]. LS-DYNA was therefore an obvious candidate for further assessment in this thesis. It is a general-purpose finite element program, and offers a large database of material models, contact algorithms and element formulations. Moreover, it is frequently employed in crash and impact simulations due to its strong capabilities in highly nonlinear and transient dynamic analysis with explicit time integration.

The motivation behind using Abaqus for simulating concrete was quite different. In fact, it was chosen for the exact opposite reason, namely the *lack* of documentation and papers in which Abaqus is employed for simulating concrete subjected to blast loads. Widely used in industrial applications with broad capabilities in multiple areas, this came as a surprise to the authors. It offers a much more conservative material database compared with that of LS-DYNA, and is generally more restrictive in its use. However, Abaqus offers the possibility of implementing user defined Fortran subroutines, which, for instance, can be used to add custom material models to the solver.

3.3 Materials mechanics

A very brief presentation of the most central aspects of the theory of plasticity will be given. For the sake of understanding, simple explanations with the use of generalized equations has been emphasized. Following is a comparison of coupled

and uncoupled damage modelling, before mesh dependence and material softening is discussed. The reader is referred to [25], [26] and [21] for a deeper understanding of this vast subject.

3.3.1 Theory of Plasticity

The theory of plasticity aims to provide a comprehensive and accurate description of the behavior of plastic materials, such as most metals, from the onset of yielding to fracture. To achieve this, it has three main ingredients: A yield criterion, a flow rule and a work-hardening rule (albeit, a fracture criterion is needed to capture fracture, but this will be disregarded in this context). The yield criterion is a relation governing the transition from elastic to plastic response in the material. It states that plastic deformation will occur in a material once the yield function equals zero, i.e.

$$f(\boldsymbol{\sigma}) = 0 \tag{3.8}$$

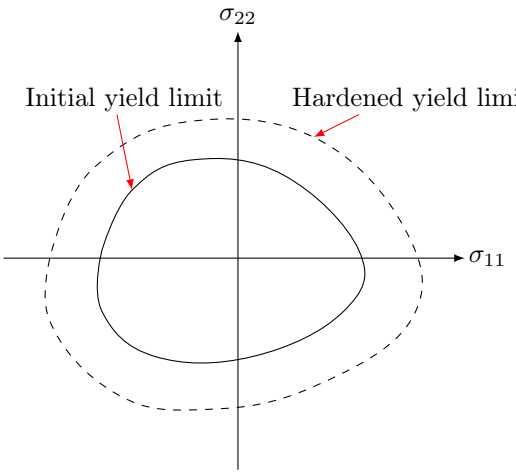

Figure 3.6: *A generic yield surface in two dimensional space. The solid line represents the initial yield limit, while the dashed line shows how work-hardening expands the yield limit in space. This is called isotropic hardening [27]. If the state of stress lies inside the area enclosed by the yield limit, i.e.* $f(\boldsymbol{\sigma}) < 0$ *, the material response will be elastic. The state of stress it not permitted to lie outside the enclosed area, hence* $f(\boldsymbol{\sigma}) \not> 0$*.*

For convenience, a graphical representation of a generic yield function in two dimensional space is provided in Figure 3.6. In addition to the initial yield limit, a hardened yield limit is included in the figure. Once a plastic material is plastically deformed it will harden, causing an increase in yield strength. This can be accounted for in the material model by introducing a hardening function, which is typically a function of the accumulated (or equivalent) plastic strain. Temperature

can be included, and, if desired, strain rate sensitivity can be taken into account, however this would make the material model viscoplastic, which is beyond the scope of discussion in this section.

$$R = R(p) \tag{3.9}$$

With this, a generalized yield function where hardening is accounted for can be established:

$$f = f(\boldsymbol{\sigma}, R) = \varphi(\boldsymbol{\sigma}) - \sigma_Y(R), \tag{3.10}$$

in which $\varphi(\boldsymbol{\sigma})$ is the equivalent stress σ_{eq}, which is defined differently in the various yield criteria, such as the Von Mises criterion (very often employed for metals) and the Drucker-Prager yield criterion (typically used for concrete and soils). The flow stress, σ_Y, is defined as $\sigma_Y = \sigma_o + R$, where σ_o is the yield stress. Stress-strain curves for three different characteristic material responses is given in Figure 3.7, wherein the total strain $\varepsilon = \varepsilon_e + \varepsilon_p$ is measured along the x-axis. The effect of hardening is clearly demonstrated.

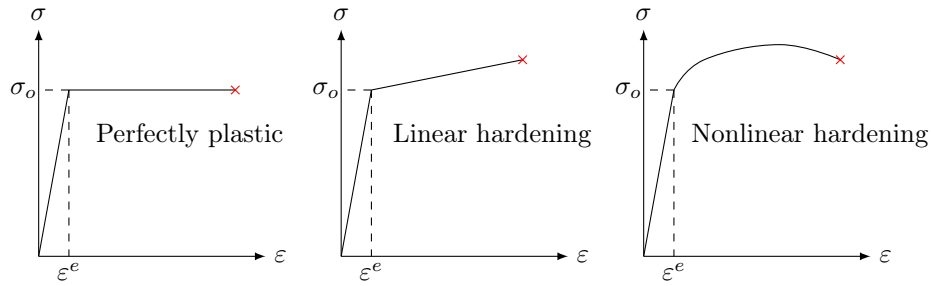

Figure 3.7: *Typical stress-strain curves in 2D-space. The leftmost relation shows the response of a material model where hardening is not taken into account. Linear hardening is depicted in the centre, while a typical elastic-plastic behavior is shown in the rightmost figure. The red cross marks the fracture point, while ε_e and ε_p are the elastic and plastic strains, respectively.*

It is assumed that during plastic deformation (plastic flow), plastic work is dissipated as heat. The main objective of the flow rule is to ensure that this dissipated energy is is non-negative [21] since, clearly, negative dissipation would violate the laws of thermodynamics, and thus be physically impossible. In the most general case, the plastic flow rule is defined by

$$\dot{\boldsymbol{\varepsilon}}^p = \dot{\lambda}\frac{\partial g}{\partial \boldsymbol{\sigma}} \tag{3.11}$$

where $g = g(\boldsymbol{\sigma}) \geq 0$ is the plastic potential function and $\dot{\lambda}$ is a non-negative scalar denoted the plastic parameter [21]. In many material models, the plastic potential function g is assumed to be equal to the yield function f. In this case, the plastic flow rule is called the associated flow rule. An interpretation of the associated flow

rule is that the plastic strain increment vector is normal to the yield surface, thus it is often called the normality rule. Consequently, the normality rule implies that the shape of the yield surface determines the direction of plastic flow. While it works very well for metals, the normality rule can be in serious error for materials such as concrete and soils where the material behavior differs greatly. In such cases, the assumption of associated flow is incorrect [27]. The alternative is to use a non-associated flow rule, i.e. one where the plastic potential function differs from the yield function.

3.3.2 Damage modelling

Material damage is caused by propagating microcracks and voids in a material [28]. This gives a reduction in the load-carrying area, and with further loading the microcracks will coalesce. At some critical point, the capacity of the material is reached, and the material fractures. Damage models aim to capture these phenomena, i.e. the deterioration of the mechanical properties of a material caused by growing cracks.

There are many different ways of incorporating damage in a material model. A procedure employed in several continuum damage models is to first represent the damage state of a material in terms of damage variables, and then to describe the mechanical behavior of the damaged material and the further development of the damage by the use of these damage variables [28]. If the evolution of damage is interacting with the plastic behavior in the material model, the damage model is defined as coupled [21]. If this is not the case, i.e. the damage has no coupling back to the material response, then the damage model is said to be uncoupled.

In many damage models, an attempt is made to capture the deteriorating effects of damage by reducing the stiffness of individual elements. While it may be successful in capturing the material response, the approach can have some adverse effects. One such effect is that when elements become very soft they tend to deform excessively. A remedy for this is to delete the affected elements by means of element erosion, a technique frequently employed in impact and blast simulations. The technique requires some sort of criterion in order to trigger the element deletion, e.g. to activate deletion once the maximum principal plastic strain is greater than some critical value. In fact, element erosion is employed in this thesis with that very criterion. The drawback of element erosion is that it is merely a numerical tool, and as such violates multiple conservation laws. It should therefore be exercised with care.

3.3.3 Mesh dependence

Material softening occurs if the damage evolution in the material model exceeds the work-hardening, or if the plastic behavior is softening. This leads to strong mesh sensitivity and slow convergence in finite element simulations of plastic behavior

due to the localization of strains [21]. Moreover, in some cases the mesh dependence becomes pathological, which implies that all deformation localizes in narrow bands of the same size as the smallest elements, h_e, and the plastic dissipation goes to zero when $h_e \to 0$ [21]. The correct interpretation of this is that mesh refinement renders the solution totally useless. What's more, such instabilities may occur in elastic-plastic materials employing a non-associated flow rule even if they exhibit work-hardening.

A remedy for mesh dependence is to employ some sort of regularization scheme, which is often done differently in various finite element solvers. Another way to avoid it is to make the model rate dependent [21].

3.4 Statistics

Whenever a scientific observation is made, some form of uncertainty is included. This uncertainty may be due to the nature of what is observed, the observation equipment or even the observer oneself. In any case, it is practical to quantify this uncertainty, and this is where statistics come into play.

As concrete is a highly inhomogeneous material, there is a large uncertainty associated with testing concrete components. The random distribution of strong aggregates and weaker mortar and voids inside concrete components result in significant differences in strength between otherwise similar components. To capture this effect in simulations has been a major goal in this thesis, and for this stochastic methods are needed.

For a series of n samples, there are two central measures that indicate the position and spread of the samples; the mean value $\bar{\mu}$ and the standard deviation $\bar{\sigma}$, defined as:

$$\bar{\mu} = \sum_{i=1}^{n} \frac{x_i}{n} \tag{3.12}$$

$$\bar{\sigma}^2 = \sum_{i=1}^{n} \frac{(x_i - \bar{\mu})^2}{n-1}, \tag{3.13}$$

where x_i is the value of sample i, for example strength, weight, etc. Once the measurements have been made, it is common to represent the data by a probability density function (PDF). In some cases, the probability distribution of the measurements is known beforehand, while often it is not. In those cases a probability distribution must be assumed and fitted to the data. The most important probability function is the normal distribution [29], defined as

$$\bar{f}(x) = \frac{1}{\sqrt{2\pi}\bar{\sigma}} e^{-\frac{(x-\bar{\mu})^2}{2\bar{\sigma}^2}}, \tag{3.14}$$

where $f(x)$ denotes the probability of a random variable x being equal to a value X.

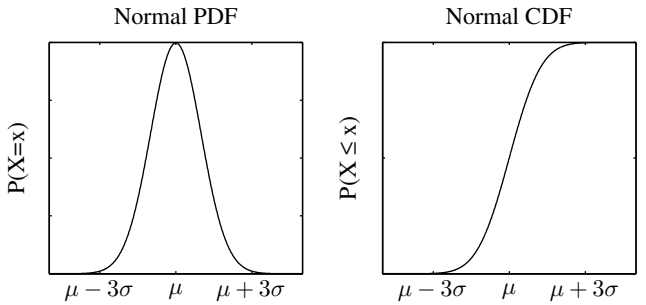

Figure 3.8: *The normal probability density function (PDF) and cumulative density function (CDF).*

Figure 3.8 shows a normal probability density function and its corresponding cumulative density function (CDF). The PDF indicates the probability that a random sample will have a given value, while the CDF indicates the probability that a random sample will have a value less than or equal to a given value. Mathematically, the CDF is defined as the integral of the PDF, i.e.:

$$P(X \leq x) = \bar{F}(x) = \int_{-\infty}^{x} \bar{f}(t)dt. \tag{3.15}$$

In this thesis, it has been assumed that the ultimate strength of concrete follows a normal distribution, as illustrated in Figure 3.9. The normal distribution is known to accurately describe many phenomena that occur in nature [29], and was therefore chosen to represent both the distribution of concrete strength and the distribution of element strength in the stochastic simulations. It is convenient to note that the probability of a value deviating more than three standard deviations from the mean is only around 0.1%. This fact will be used later when determining the range of material strengths needed in the simulations.

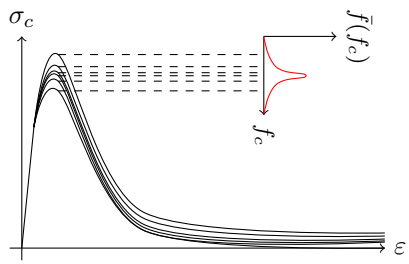

Figure 3.9: *Assumed normal distribution of concrete strength.*

Chapter 4

Concrete

Due to its low cost and widespread availability, concrete has become the most widely used construction material in the world. It also exhibits excellent resistance to water, and may easily be formed into various shapes and sizes [30], hence its frequent use in dam constructions, bridges and offshore platforms. However, concrete is also a highly complex material, and shares little in common with metallic construction materials like steel. In order to understand the physical behavior of concrete, one must first take a look at the building blocks from which it is created, i.e. the internal structure of concrete. Following is a brief presentation of the mechanical properties of concrete, before failure modes, size effects and the two material models employed in this thesis are presented.

4.1 The structure of concrete

Concrete is an amorphous solid, with a highly heterogeneous and complex structure. At the macroscopic level, it may be considered to be a two-phased material, consisting of aggregate particles dispersed in a matrix of hydrated cement paste (HCP) [30]. This is illustrated in Figure 4.1. The aggregate particles are typically gravel and crushed rocks of different shapes and sizes, and may considerably affect the mechanical properties of concrete [30, 31]. After a chemical reaction of cement with water, commonly referred to as the hydration of cement, the HCP acts as a binding medium in the concrete. This hydration process is somewhat time consuming, with concrete being close to its maximum strength after a standardized time period of 28 days [31]. One should be aware of the importance of the water/cement ratio, which greatly influences the strength of concrete [31]. Less water yields a stronger concrete.

At the microscopic level, the complexity of the concrete structure becomes evident. Neither phases are homogeneous, nor are they distributed in a well manner. The

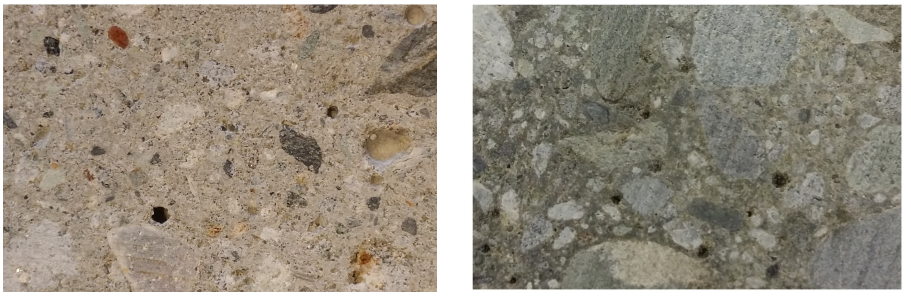

(a) *(b)*

Figure 4.1: *Polished sections from two cylinder concrete specimens used in the experiments. Aggregate particles and voids are clearly present.*

cement phase alone consists of several solid phases of different characters, in addition to a myriad of voids, all of which affect the physical properties of concrete to some extent. Usually, the aggregate particles contain multiple minerals, along with microcracks and voids. On top of all this, the structure of the HCP is dynamic, i.e. it changes with time, humidity and temperature [30]. To make things even more complicated, a third (and crucial) phase at the microscopic level is hereby introduced, namely the transition zone.

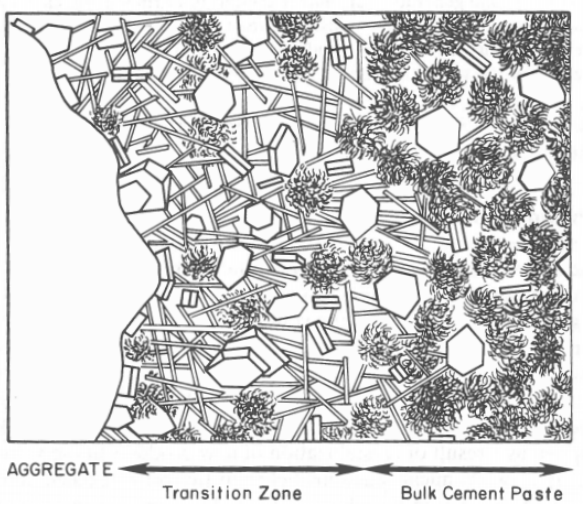

Figure 4.2: *Illustration of the transition zone in concrete. The lamellae in the transition zone are calcium hydroxide crystals, which due to their geometry and orientation possess little adhesion capacity. There is also a large amount of microcracks present, which is a major factor responsible for the poor strength of the transition zone [31].*

The transition zone represents the interfacial region between the particles of coarse aggregate and the HCP [30]. It is generally the weakest among the three phases,

thus it greatly influences the mechanical behavior of concrete. In fact, the transition zone is cause to several of the main features of concrete, for instance its brittle tensile behavior and its toughness in compression. The presence of the transition zone is also the reason why concrete fails at considerably lower stress level than either of its two main constituents [31]. A detailed illustration of the transition zone is given in Figure 4.2.

4.2 Mechanical properties

In metals, plastic deformation is the result of relative motion, or slip, on specific crystallographic planes [25]. Since concrete lacks the crystalline, grid-like structure found in metals, the discussion of plastic deformation caused by plastic slip is inapplicable. Instead, nonlinear behavior in concrete is governed by a completely different mechanism, namely by the propagation of microcracks (mainly in the transition zone) during loading [32]. This is also the reason why concrete exhibits pressure dependency.

Another central characteristic of concrete is that it responds differently in compression and tension, thus it is natural to consider the two loading scenarios separately. Moreover, concrete is a highly rate-dependent material [33], so a presentation of its dynamic response characteristics is also necessary.

4.2.1 Compressive behavior

A typical load-displacement relationship for concrete subjected to uniaxial compression is shown in Figure 4.3. A nearly linear-elastic behavior is observed up to about 30% of the maximum compressive strength. After this point, the curve gradually becomes more nonlinear up to the ultimate capacity. Beyond this, softening occurs until the concrete is fully crushed.

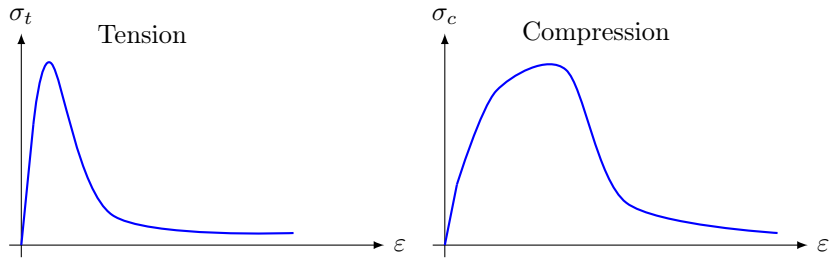

Figure 4.3: *Typical stress-strain curves in tension (left) and compression (right). The compressive strength is usually in the range 20-120 MPa, while the strength in tension is only a fraction of this.*

The reason why concrete behaves this way in compression lies in the transition zone, as previously stated. At the early stages of the loading, the cracks existing

in the concrete remain nearly unchanged. At about 30% stress level, cracks will start to propagate in the transition zone, and they will continue to grow into the *HCP* with further loading. Consequently, a bridging between numerous growing cracks occurs, resulting in a progressive failure of the concrete near the maximum capacity [32]. Compressive strengths for concrete typically exist in the range 20-120 MPa.

4.2.2 Tensile behavior

Cracks propagate readily and at a much lower stress level in tension than in compression. In addition, tensile-induced cracks propagate normal to the direction of maximum tensile stress, and will thus reduce the load-carrying area in concrete. Moreover, they arrest much less frequently [30]. This is why concrete is weak and far more brittle in tension. For comparison, the tensile strength of concrete is typically 5-10% of its compressive strength [32]. However, this relationship is not necessarily true for high-strength concretes. Figure 4.3 illustrates the principal behavior of concrete in tension.

4.2.3 Pressure dependence

Concrete is a pressure dependent material. Confining pressures, or compressive triaxial stress states, may greatly increase its compressive strength and ductility, and can even cause a change in the governing mechanisms in compressive failure [32]. The reason for this is that if the confining pressure is sufficiently great, crack propagation is prevented. It can be said, in general, that concrete behaves in a ductile manner if all three principal stresses are compressive and somewhat equal in magnitude [25].

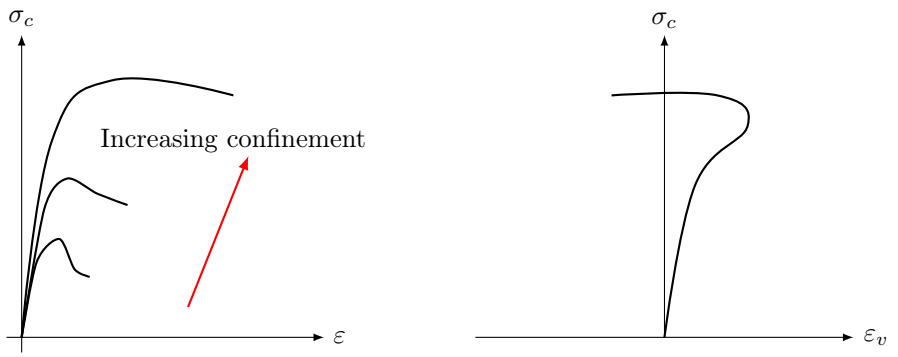

Figure 4.4: *A typical triaxial stress-strain relationship is illustrated in the left figure. The right figure describes the typical dilatancy of concrete, where the volumetric strain ε_v is measured along the horizontal axis.*

Furthermore, the formation and growth of cracks parallel to the direction of the greatest compressive stress causes a volume increase in concrete known as *dilatancy*. Typically, the volumetric strain ε_v begins to decrease from its elastic value at stresses greater than about half the ultimate strength, reaches zero near the ultimate strength, and becomes negative in the strain softening range [27]. This effect can be seen in 4.4, where also a typical triaxial stress-strain relationship for concrete is depicted.

4.2.4 Rate dependence

Concrete is highly affected by loading rates [33–36], particularly in tension where a pronounced increase in strength for high loading rates can be observed. This is usually attributed to the presence of free water in the pores of the concrete, as well as inertia effects [33]. The best way to show exactly how concrete responds to dynamic loading, is by a graphical representation. Figure 4.5 below shows multiple experimental test results provided by several different authors for both tensile and compressive loading at different strain rates. The vertical axis shows the Dynamic Increase Factor (DIF), which measures the increased strength due to a higher strain rate (along the horizontal axis).

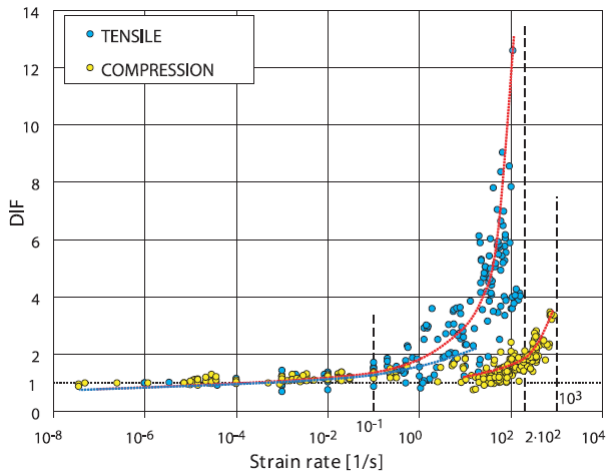

Figure 4.5: *The strain rate effect on tensile and compressive strength is shown, where the data points represent results from various studies by several different authors [34]. The leftmost vertical dashed line marks the location below which no difference is observed in compressive and tensile strength, while the two remaining dashed lines are the tensile and compressive asymptotes.*

From the figure one can distinguish two regions of rate dependence, and what might be regarded as a transition zone between them. At fairly low strain rates a moderate and somewhat linear increase in strength is observed. With higher strain rates, i.e. past the transition zone, a very steep strength increase occurs. While the trends are very clear, neither the transition zone nor the DIFs are easy

to determine accurately. It is apparent that different authors arrive at different conclusions, however it seems from the figure that the DIF may easily exceed 6 and 2 in tension and compression, respectively. Moreover, the figure suggests that the transition zone occurs at a strain rate of roughly 1/s in tension, and 10/s in compression. In the case of blast loading, pressures may yield loads associated with strain rates in the range $10^2 - 10^4 s^{-1}$ [37], thus rate dependence may be important to take into account for such problems.

4.3 Failure modes

In this section, a brief introduction to the failure modes in dynamically loaded concrete plates will be given. Figure 4.6 illustrates the primary modes of failure, and a more detailed explanation is given below.

Concrete plates subjected to severe short duration pressure loads (shock waves, explosions etc), are primarily associated with two modes of localized failure: Flexural and shear failure [15]. Loading characteristics such as duration, proximity and intensity govern the mode of failure of any given plate, in addition to the plate properties (for instance rigidity) and boundary conditions. Typically, if the load impulse and intensity is sufficiently high, the plate will experience a brittle shear failure either along its boundary or in a more localized region (often called punching shear). Flexural failure usually occurs with slower load rates and in less rigid plates. The bending of the plate introduces in-plane tensile and compressive stresses, and since concrete is far weaker in tension, cracking initiates on the side loaded in tension. Moreover, sudden deformation may cause *spalling*, and the reflection of compressive stress waves as tensile stress waves at the rear surface of the plate may cause *scabbing*, both of which are dangerous phenomena [38]. Since scabbing is caused by the reflection of propagating stress waves, the thickness of the impacted concrete is of importance. Haug and Osnes [4] used theory of one dimensional stress waves, and found that for scabbing to occur in their 50 mm plates, which is the same thickness as used in this thesis, the duration of the stress wave would have to be shorter than 0.025 ms. They concluded that it would be very unlikely for this to happen in the shock tube experiments, and it is reasonable to assume this conclusion to be valid for the shock tube tests in this thesis also.

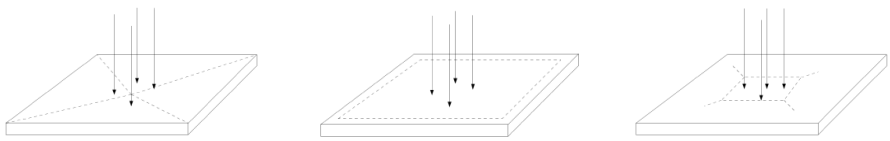

Figure 4.6: *Typical failure modes for concrete plates. Flexural failure is depicted in (a), while shear and punching shear is shown in (b) and (c), respectively [4].*

One should keep in mind that very often the failure modes occur simultaneously. Furthermore, adding reinforcement steel in concrete plates will not only enhance the tensile and shear strength, it may limit the fragmentation in case of total collapse.

4.4 Size effect in Concrete

In elastic analysis of structures, it is assumed that the size does not influence the strength of the structure, i.e. a large structure will fail at the same stress level as a small structure. For many materials, this is generally not the case, and it is instead observed that large structures fail at lower stress than small structures. This phenomenon is called the *size effect*. Bazant [39] names six sources for the size effect in concrete:

The boundary layer effect is because the volume fraction of large aggregates will be lower close to the walls of the structure. The boundary layer thickness is not dependent on specimen size, and has different mechanical properties than the bulk concrete. For a small part, the boundary will thus make up a larger fraction of the volume than for a large part, and the strength will therefore be different.

Diffusion effects cause large specimens to dry slower than small specimens, leading to a difference in strength.

Hydration heat causes large specimens to develop higher temperatures than small specimens during curing, causing a difference in strength.

The statistical size effect is caused by the internal variation of strength in the structure, and can be described by the weakest link approach. For a large structure, there is a higher probability that a critical flaw is present in the loaded volume, causing a higher probability of failure.

The fracture mechanics size effect is caused by the fact that the energy required for crack propagation is approximately constant, while the stored elastic energy in the fracture process zone (FPZ) is dependent on the crack length. If the failure of two structures are geometrically similar, the crack band at failure will be larger for a larger structure. When a crack propagates, there must be balance between the elastic energy release rate and the fracture energy rate, and since more elastic energy is stored in the FPZ of a long crack, the crack propagates with less resistance in a large specimen. See [39] for a more comprehensive explanation.

Fractality in crack surfaces may be another source of size effects, and influences the fracture mechanics size effect. Bazant points out, however, that this effect is probably only hypothetical.

Figure 4.7 shows how the strength of single edge notched beams in three point bending vary with the characteristic size of the beam. The horizontal axis indicates the logarithmic characteristic size of the beam, while the vertical axis shows the

characteristic strength. The horizontal asymptote is the strength derived from plastic analysis, which assumes that the strength is independent on the size of the beams. The asymptote marked *LEFM* is the analytical solution obtained from *Linear Elastic Fracture Mechanics*. It is seen that the strength of the beams drop significantly as the size is increased, indicating the importance of taking the size effect into account when designing large structures.

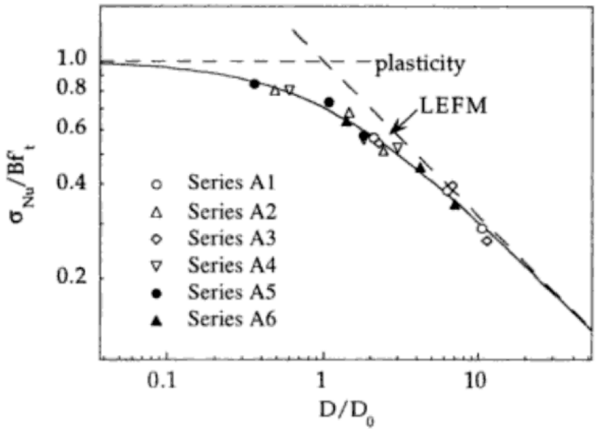

Figure 4.7: *Size effect in single edge notched beams subjected to three point bending [39].*

4.5 Numerical modelling of concrete

This section will present the concrete material models used in this thesis, namely K&C in LS-DYNA and the CDP model in Abaqus.

4.5.1 The K&C Concrete Damage Model

The Karagozian and Case (K&C) Concrete Damage Model was originally proposed by Malvar et al. [40] in 1994, and later revised to include automatic parameter generation and strain rate sensitivity, among others [41]. The model keyword in LS-DYNA is **MAT CONCRETE DAMAGE REL3*, and a total of 49 input parameters are needed. However, since the model features automatic parameter generation, only the unconfined compressive strength is needed to fully define the material behavior.

The K&C model has been used by numerous authors to simulate the effect of blast loads on concrete structures, and has proved to be a robust model that is able to capture much of the behavior that is observed in experimental tests. Lin et al. [24] and Thiagarajan et al. [10] have used the K&C model to simulate reinforced concrete plates subjected to blast loads, and both concluded that the model was able

to capture the experimental behavior satisfactorily. Li and Hao [12] simulated concrete spall damage on a reinforced concrete plate and reinforced concrete columns, and also found that the K&C model performed well. A comparative study between several material models in LS-DYNA [23] found that the K&C model was suitable for modeling quasi-static, blast and impact loads, and was able to capture softening, dilation, confinement effect and strain rate effects properly. Tu and Lu [22] compared the Riedel-Hiermaier-Thoma (RHT) and K&C models on a one-way reinforced concrete plate subjected to a 0.5 kg TNT charge, and concluded that the K&C model performed better, even without needing any calibration.

The model decouples the volumetric and deviatoric strain, and an equation of state gives the relationship between hydrostatic pressure and volumetric strain. The deviatoric response is determined by three independent failure surfaces denoted $\Delta\sigma_y$, $\Delta\sigma_m$ and $\Delta\sigma_r$, representing the maximum von Mises stress at yielding, ultimate state and residual state. The failure surfaces are dependent on the hydrostatic pressure, and are formulated as

$$\Delta\sigma_y = a_{0y} + \frac{p}{a_{1y} + a_{2y}p} \tag{4.1}$$

$$\Delta\sigma_m = a_0 + \frac{p}{a_1 + a_2 p} \tag{4.2}$$

$$\Delta\sigma_r = \frac{p}{a_{1f} + a_{2f}p} \tag{4.3}$$

where p is the hydrostatic pressure, $\Delta\sigma = \sqrt{3J_2}$ and $a_{iy}, a_i and a_{if}$ are material constants. Figure 4.8 shows a typical uniaxial compression curve and the evolution of the failure surfaces. Up to yield, the response is elastic. After yield, $\Delta\sigma$ is interpolated linearly between $\Delta\sigma_y$ and $\Delta\sigma_m$ by a damage function $\eta(\bar{\lambda})$. After the maximum stress has been reached, $\Delta\sigma$ is interpolated between $\Delta\sigma_m$ and $\Delta\sigma_r$, also by the damage function $\eta(\bar{\lambda})$. The damage function starts at zero and reaches one at the maximum stress, before declining towards zero again to represent softening of the concrete. This function is tabulated in LS-DYNA by 13 η-$\bar{\lambda}$ data pairs.

$\bar{\lambda}$ is a function of the equivalent plastic strain $\bar{\varepsilon^p} = \sqrt{\frac{2}{3}\varepsilon^p_{ij}\varepsilon^p_{ij}}$ and the hydrostatic pressure, and is defined as

$$\bar{\lambda} = \begin{cases} \displaystyle\int_0^{\bar{\varepsilon^p}} \frac{d\bar{\varepsilon^p}}{r_f(1 + p/r_f f_t)^{b_1}} & \text{for } p \geq 0 \\ \displaystyle\int_0^{\bar{\varepsilon^p}} \frac{d\bar{\varepsilon^p}}{r_f(1 + p/r_f f_t)^{b_2}} & \text{for } p < 0 \end{cases} \tag{4.4}$$

where r_f is a rate enhancement factor and f_t is the tensile strength of the concrete. As seen, the only difference between the two definitions is that the constant b_1 is changed into b_2 when the material is subjected to tension.

The automatic parameter generation is based on material data obtained from a large number of tests on different types of concrete [41], where the default concrete had a uniaxial compression strength of around 45 MPa. For other concrete

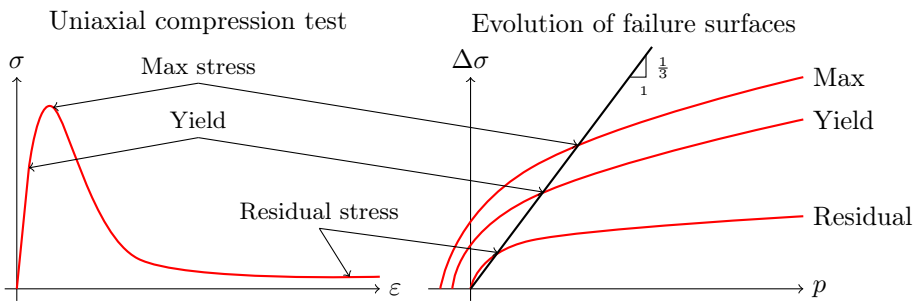

Figure 4.8: *On the left, the stress-strain relation from a uniaxial compression test is shown. The curves on the right show the evolution of the failure surfaces with hydrostatic pressure. In uniaxial compression, the ratio of $\Delta\sigma$ to p is constant and equal to 1/3, as indicated by the straight line. The yield, max and residual deviatoric stress is found at the intersection between this line and the respective failure surface.*

strengths, the default concrete data is simply scaled such that the data will approximate the new strength. Figure 4.9 shows the uniaxial stress-strain curves for various strengths using the automatic parameter generation.

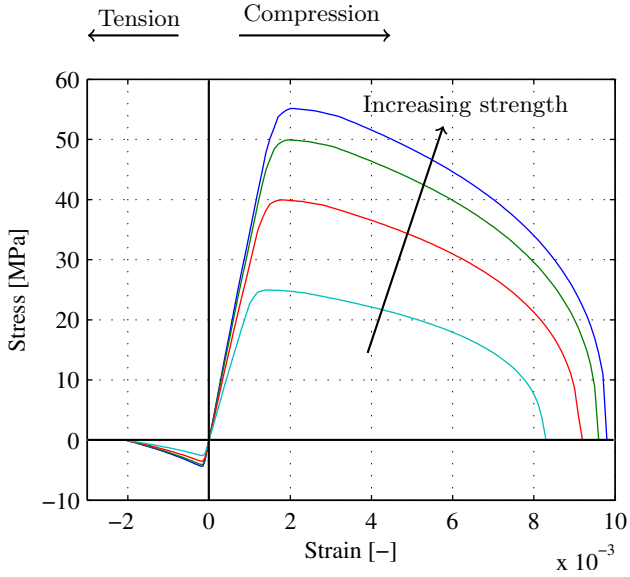

Figure 4.9: *Uniaxial 1-element stress-strain curves from the K&C model at different strengths using the automatic parameter generation capability.*

Another important feature of the K&C-model in LS-DYNA is the strain softening regularization scheme. When using the automatic parameter generation, the model assumes that a crack forms in a single element. The softening of the damage function $\eta(\bar{\lambda})$ is then scaled with the element size so that the fracture energy

remains approximately constant for any element size. This results in small elements being more ductile than larger elements. The reader is referred to [41] for a more in-depth explanation of the regularization scheme.

4.5.2 The Concrete Damaged Plasticity Model

The Concrete Damaged Plasticity Model in Abaqus is based on the models proposed by Lubliner et al. [27] in 1988 and by Lee and Fenves [42] in 1998. It provides a general capability for modelling reinforced or plain concrete in all types of structures, subjected to either monotonic, cyclic and/or dynamic loading under fairly low confining pressures. In this sense, it aims to be an all-purpose model for concrete. It is based on two sets of uniaxial data and five additional parameters, in addition to the elastic properties of the concrete. The uniaxial data, which describes the post-yield stress-strain behavior in compression and tension, must be calibrated for the concrete one wishes to simulate. Thus, extensive experimental testing is required to establish all input parameters for the model.

While the K&C model in LS-DYNA has been used in numerous studies on blast loaded concrete structures, hardly any articles on the matter can be found in which the CDP model is employed. However, there are several recent studies on other complex problems where concrete is simulated using the CDP model. Genikomsou and Polak [43] find in their study on punching shear of plain concrete slabs that the model properly predicts the response observed in experiments. Furthermore, Tysmans et al. [44] successfully simulate high-performance fibre-reinforced cement subjected to both uniaxial and biaxial tension, and they conclude that the CDP model accurately captures the strain hardening behavior in tension. The lack of studies on blast loaded concrete simulated with the CDP model is therefore interesting, considering that it is being successfully used to simulate the response of concrete in several other complex problems.

The CDP model is based on classical theory of plasticity and continuum damage mechanics, and is capable of representing tensile and compressive damage independently. It assumes that the two main failure mechanisms are tensile cracking and compressive crushing. Moreover, the evolution of the yield surface is controlled by two hardening variables, namely the compressive and tensile equivalent plastic strains $\tilde{\varepsilon}_c^{pl}$ and $\tilde{\varepsilon}_t^{pl}$, and is given by:

$$f = \frac{1}{1-\alpha}\left(\bar{q} - 3\alpha\bar{p} + \beta(\tilde{\boldsymbol{\varepsilon}}^{pl})\langle\hat{\bar{\sigma}}_{max}\rangle - \gamma\langle-\hat{\bar{\sigma}}_{max}\rangle\right) - \bar{\sigma}_c(\tilde{\varepsilon}_c^{pl}), \tag{4.5}$$

where $\bar{p}$ is the effective hydrostatic pressure, and $\bar{q}$ is the Mises equivalent effective stress. $\hat{\bar{\sigma}}_{max}$ is the maximum principal effective stress, thus in biaxial compression ($\hat{\bar{\sigma}}_{max} = 0$) Equation (4.5) reduces to the Drucker-Prager yield condition [45]. Effective stress is related to the true stress through the damage function:

$$\boldsymbol{\sigma} = (1-d)\bar{\boldsymbol{\sigma}}, \tag{4.6}$$

in which $(1-d)$ represents the reduction in load-carrying area due to damage (crack growth), with $d \in [0, 1]$ where 0 represents no damage. This is completely equivalent for the other effective values. While the parameter $\beta = \beta(\tilde{\varepsilon}^{pl})$, α and γ are dimensionless material constants governing the pressure sensitivity and shape of the yield surface in the deviatoric plane, respectively. A detailed graphical representation of the yield surface f in plane stress is given in Figure 4.10, while Figure 4.11 below shows how the model behaves in uniaxial tension and compression.

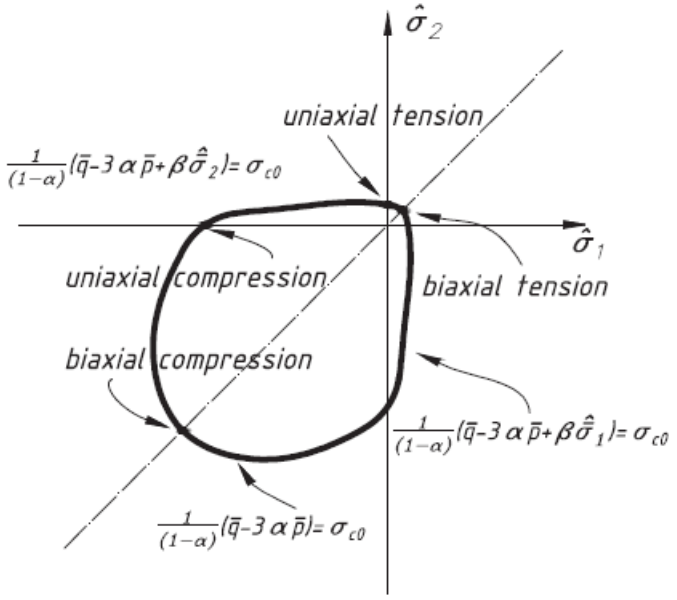

Figure 4.10: *Yield surface in plane stress [44]. Notice the big difference in compressive and tensile yield strength, a typical feature in concrete. Also be aware that the surface is in effective stress space, i.e. damage greatly influences failure.*

Due to its use of continuum damage mechanics, there is no tracking of individual cracks at the material integration points in the CDP model. Instead, the scalar damage parameter d simulates cracking by reducing the overall stiffness in the model. A consequence of this is what might be one of the major shortcomings of the CDP model, namely that element erosion is unavailable. An alternative way to track cracks is to visualize the maximum principal plastic strain after an analysis.

The reader is referred to the Abaqus Analysis User's Guide [45] and the Abaqus Theory Guide [46] for a more comprehensive understanding of the CDP model.

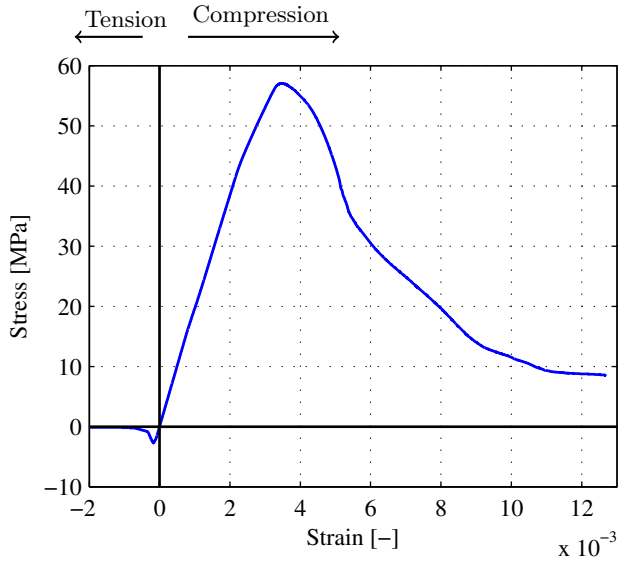

Figure 4.11: *Uniaxial stress-strain curves from the CDP model, performed with 1000 and 1 elements in compression and tension, respectively. The input parameters employed in the CDP model to generate this figure will be presented in detail in Chapter 7.*

Chapter 5

Introductory Experimental Work

Before the shock tube experiments could be performed, the concrete plates had to be created. It was of interest to determine the compressive and tensile strength of the concrete used in the experiments, therefore a large number of material test specimens were cast and tested in compression and tension. The stochastic properties of the concrete was investigated by performing series of identical tests. It was also necessary to determine the mechanical properties of the rebar steel, thus uniaxial tension tests were performed and two material models were studied and fitted to the results. The fits were validated in Abaqus.

5.1 Concrete mix

A B20 concrete with a maximum aggregate size of 16 mm was delivered by NorBetong AS, Trondheim. Table 5.1 describes the mixture in detail, while the aggregate size distribution is given in the following Table 5.2. See the concrete receipt provided by NorBetong in Appendix A.1 for further details regarding the mix.

Material	*Weight %*
Water	3.90
Aggregate	82.95
Norcem Standard FA	13.04
SR-N	0.09
Silica	0.00

Table 5.1: *B20 concrete mix.*

Sand 0-2 mm	*Sand 0-8 mm*	*Gravel 8-16 mm*
4.27 %	60.23 %	35.50 %

Table 5.2: *B20 aggregate size distribution.*

5.2 Testing of fresh concrete

The slump test and the pressure gauge method were performed, in accordance with Norwegian Standards (NS) [47, 48], in order to determine the consistence and air content of the fresh concrete, respectively. The air content was measured to be 2.5 %, while the slump test gave a total height of 195 ± 5 mm. The reader is referred to the standards for further information regarding the tests. Figure 5.1 shows the performed slump test.

(a) ***(b)*** ***(c)***

Figure 5.1: *Slump test (a) prior to removal, removing the mould (b) and (c) the remaining slump. The cone mould is filled with a concrete sample, before it is raised steadily. The height reduction is measured and used to determine the consistence of the fresh concrete [31].*

5.3 Casting of concrete

Work related to the casting of plates and material test specimens is presented in the subsequent section. The casting was performed in accordance with NS-EN 12390-2 [49].

5.3.1 Test specimens

Shocktube experiments were to be performed on concrete plates of outer dimensions 625×625×50 mm. The formwork boxes were the same as used by Haug and Osnes in 2015, and consisted of numerous wooden plates assembled to form cavities with the correct outer dimensions. The plates were pre-drilled with the correct bolt pattern of the shock tube flange, and plastic tubes were inserted through the holes

so that the concrete plates would get the same bolt pattern. The moulds were hard to assemble with perfect accuracy. Consequently, fitting the plastic tubes (PMMA) through the holes in the formwork boxes turned out to be troublesome. To resolve this issue, a tapered guide pin was machined from aluminium and fitted into the tip of each tube, thus making it possible to guide the tubes (forcefully) through the holes. See Figure 5.2. Some of the holes in the formwork plates had been mistakenly drilled in the wrong locations, and were covered with duct tape to prevent concrete from flowing into them, as seen in 5.2a.

(a) *(b)* *(c)*

Figure 5.2: *(a) Assembling the formwork boxes, the tapered aluminium guide pin (b) and (c) fitting the plastic tubes. To the right in (a), a mould plate with mistakenly drilled holes can be seen with duct tape covering some of the holes.*

All the plates were reinforced with one 8 mm shear rebar, while five of the plates were additionally reinforced with a pair of identical rebar meshes. This is illustrated in Figure 5.3 and 5.4. Copper wire and plastic spacers were used to tighten and support the rebar prior to the casting. Furthermore, a lifting point was added to the top of each concrete plate to make them easier to transport.

The formwork and tubes were oiled thoroughly with *Texaform CR3* prior to casting to ensure easy removal, without concrete sticking to the forms. Lastly, the formwork was fastened tightly to the foundation, and a wooden framework was added in the top of the formwork to strengthen the formwork sufficiently to withstand the hydrostatic pressure of the liquid concrete during casting.

A total of 15 plates, 42 cubes (100×100×100 mm) and 20 cylinders (Ø100 × 200 mm) were cast. In addition, three 100 × 100 × 600 mm beams were cast in order to perform three-point bending tests. Tamping and usage of a vibration table was necessary to remove air bubbles from the fresh concrete.

The moulds for the cubes and cylinders were removed the following day, while the formwork boxes were disassembled two days after the casting. Unfortunately, among the five reinforced plates, there were two with large voids due to poor tamping during the casting process. Only one of these could be repaired. In addition, using duct tape to cover the mistakenly drilled holes in the formwork plates did not work perfectly, as the tape came loose in some places and concrete

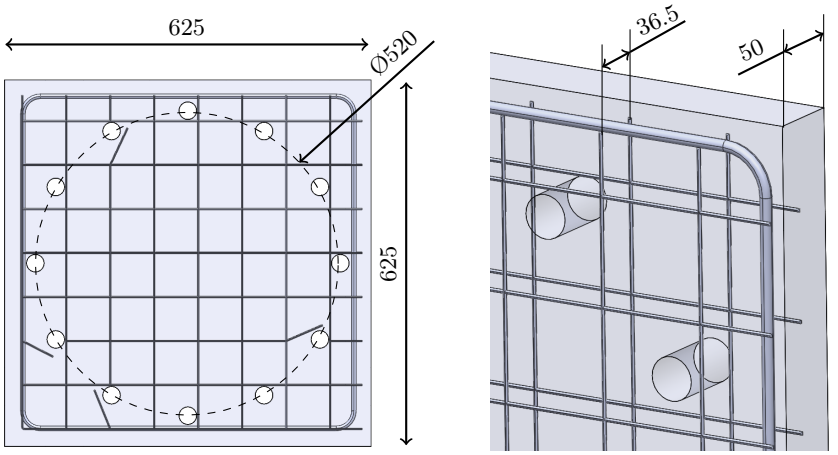

(a) *(b)*

Figure 5.3: *(a) Front view and (b) detail view of the reinforcement in the 50 mm concrete plates. The rebar mesh consists of 71.8 x 71.8 mm squares, with an approximate thickness of 2.5 mm.*

(a) *(b)*

Figure 5.4: *Rebar mesh (a) and plastic support (b).*

flowed into the holes. Also, the hydrostatic pressure of the concrete caused the duct tape to stretch inwards, leaving bulges in the concrete plates, as seen in Figure 5.5f. These irregularities were later removed by grinding to ensure a flush mount to the shock tube flange.

To ensure sufficient humidity and a stable temperature for the concrete curing process, the cubes and cylinders were submerged in water. For the very same reasons, the plates were wrapped in soaked cloth and sealed with plastic foil.

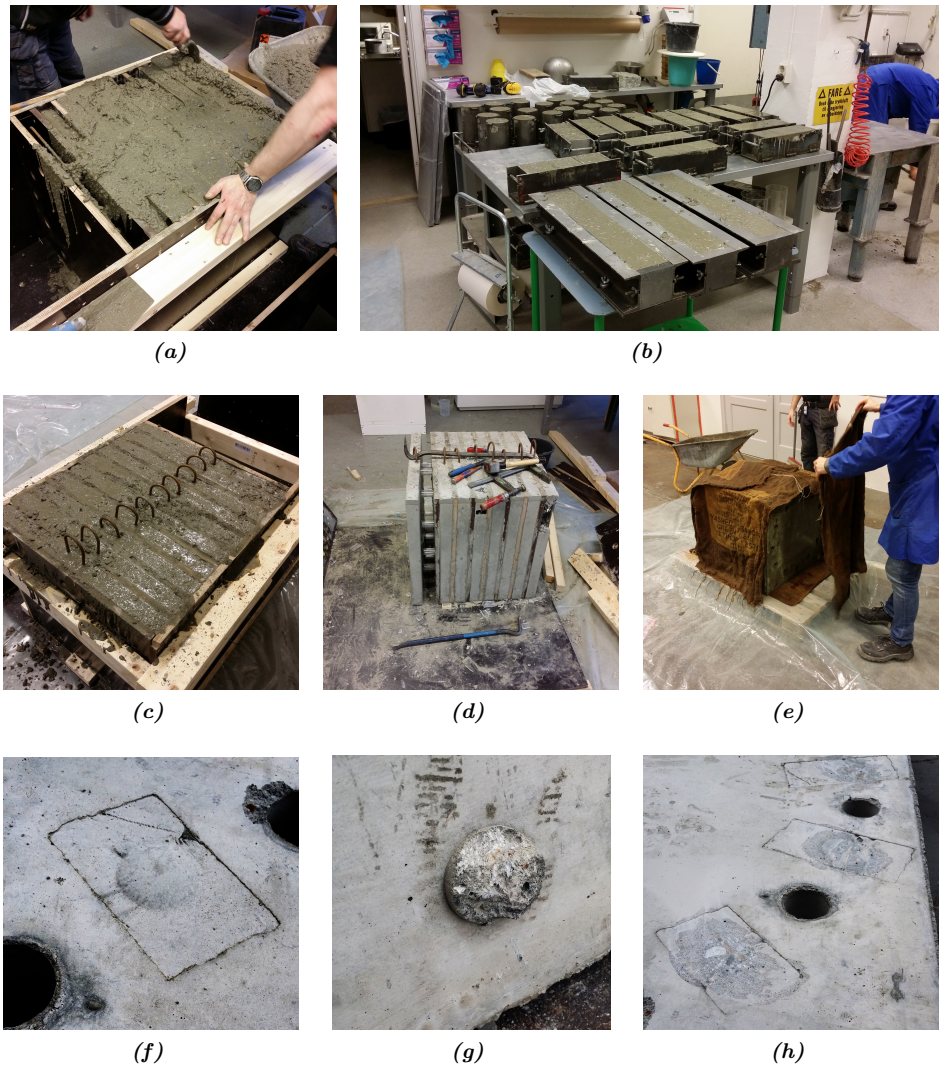

(a) *(b)* *(c)* *(d)* *(e)* *(f)* *(g)* *(h)*

Figure 5.5: *Filling the plate formwork (a) and filled material test specimen moulds (b). The creation of concrete plates; fresh concrete in (c), disassembling the formwork (d) and sealing the plates in soaked cloth and plastic (e). Defects in the concrete plates due to (f) bulging of tape covering mistakenly drilled holes and (g) due to missing tape. The plate after grinding is shown in (h).*

5.4 Physical testing of cured concrete

The concrete specimens were tested to obtain the mechanical properties of the cured concrete. The cubes and cylinders were tested in uniaxial compression and the beams were tested in bending. The cylinders were also tested in tensile splitting. Excluding the bending test, these tests only give the ultimate limit state of the concrete, and does not say anything about the shape of the load-displacement curve.

All the cubes were weighted prior to testing, and it was found that the cured concrete after 28 days of curing had an average density of 2445 kg/m^3. The full results from the testing of cubes and cylinders are given in Tables A.1 and A.2 in the appendix.

5.4.1 Cube compression

The cubes were tested in uniaxial compression by a 3000 kN automatic *Toni Tech* compressive test rig. A loading rate of 0.8 MPa/s was used for all the tests. The machine was set up such that the test would stop once a decline in force was detected. Figure 5.6 shows three cubes after testing.

(a) *(b)* *(c)*

Figure 5.6: *Crack patterns of three cubes subjected to uniaxial compression. The load direction in (b) and (c) is the same as in (a).*

Of the 42 cubes that were cast, 20 cubes were tested on the 28th day after testing. This was done in order to obtain a statistical basis for the variation in strength of the concrete. A summary of the test results is shown in Table 5.3. Figure 5.7 shows the distribution of the test results, while the test results for each individual cube is presented in Appendix A.2.

From the cumulative probability plot, it is seen that the statistical variation in strength is reasonably approximated by a normal distribution.

Measure	*Result* [MPa]
Average strength	46.35
Standard deviation	0.73
Max	48.15
Min	44.66

Table 5.3: *Strength of cubes 28 days after casting. 20 cubes were tested on this day.*

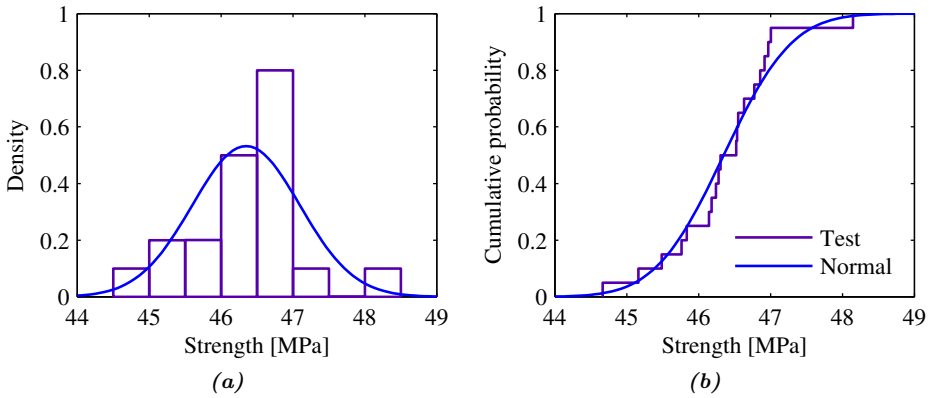

Figure 5.7: *(a) Probability density plot and (b) cumulative probability plot of the results obtained from uniaxial compression cube testing.*

Some cubes from the same batch were also tested at 2 days, 7 days, 14 days, 49 days and 84 days after casting. It should be noted that the tests at 49 days of curing were conducted in a different and less accurate test machine than the rest of the tests, and may therefore be unreliable. As expected, the strength increased with aging of the concrete, as shown in Figure 5.8. The strength as a function of curing time can be estimated by the expression [30]

$$f_c(t) = \frac{at}{b + ct}, \tag{5.1}$$

where t is the age in days and a, b and c are constants. Using MATLAB's curve fitting tool *lsqcurvefit*, the constants were determined by least square fitting. Table 5.4 shows the constants obtained from the curve fitting.

It can be seen that a slight increase in strength can be expected as the concrete is aged beyond 28 days, but this increase is negligible compared with the statistical variation observed in the tests. The high strength obtained after 84 days of curing was unexpected, and the reason for this is not known.

a	b	c
217.18	10.29	4.22

Table 5.4: *Strength evolution constants obtained from least square fitting.*

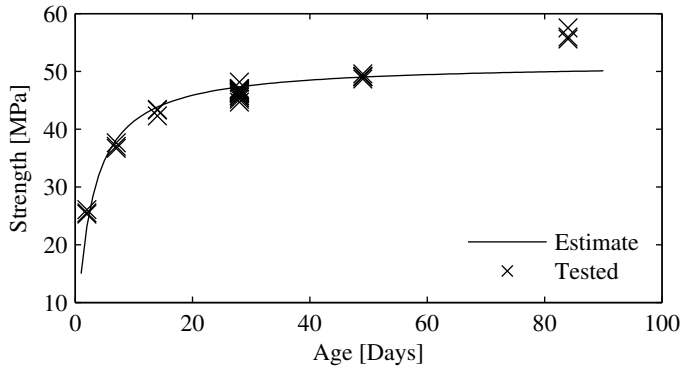

Figure 5.8: *Strength versus curing time for the concrete.*

5.4.2 Cylinder compression

When testing concrete in uniaxial compression, the observed strength of the concrete is greater when testing a 100 mm square cube than a $\emptyset 100 \times 200$ mm cylinder. This is because the friction between the concrete and load applicator plates induce confining pressures in the concrete, which increases the strength of the concrete. Since the aspect ratio of the cylinder is greater, such boundary effects are less dominant in a cylinder, causing the observed strength to be lower. Because of this, the cylinder compression strength is closer to the real uniaxial compression strength, and is therefore used for design purposes [50].

Since the cylinders were cast upright, the top surface was free during curing, resulting in a very rough surface. This is not acceptable when testing, so the cylinders had to be ground in the top and bottom to obtain parallel and true surfaces.

Five cylinders were tested in uniaxial compression 29 days after casting. Figure 5.9 shows the damage evolution of one of the cylinders during testing. It should be noted that the maximum stress is achieved slightly before any cracks appear. The average compression strength of the cylinders was found to be 39.6 MPa, which is 6.75 MPa lower than the cube strength. This difference is slightly less than the 10 MPa difference suggested in Eurocode 2 1-1 [50]. The results from each individual cylinder are shown in Table 5.5.

From the cylinder compressive strength f_c, the elastic modulus of the concrete E_c can be estimated by [30]

$$E_c = 21500(f_c/10)^{1/3}. \tag{5.2}$$

This leads to an estimated elastic modulus of approximately 34 GPa.

Test	*Result* [MPa]
1	40.15
2	39.90
3	38.59
4	38.90
5	40.54
Average	39.62
Standard deviation	0.747

Table 5.5: *Strength of cylinders 29 days after casting.*

(a) ***(b)*** ***(c)*** ***(d)***

Figure 5.9: *Damage evolution of a concrete cylinder in compression. In (a), the first cracks have just appeared. These cracks continue to grow in (b), before they meet and large pieces of concrete becomes loose (c and d). The volume dilatancy effect is clearly seen in (b), where the cylinder bulges outward in the middle.*

5.4.3 Tensile splitting test

Tensile splitting tests were performed in order to get an estimate of the tensile strength of the concrete. The tensile splitting test is performed by laying a concrete cylinder flat in a test machine, and placing a strip of wood between the concrete and test machine at each contact line. When the cylinder is subjected to compressive force, tensile stresses are introduced into the cylinder until the cylinder splits in two [32]. The tensile strength of the concrete can then be estimated by the formula [51]

$$f_t = \frac{2F}{\pi D_c L} \tag{5.3}$$

where F is the force required to split the cylinder, D_c is the diameter and L is the length of the cylinder. It should be noted that the tensile strength obtained from the splitting tests is known to overestimate the real tensile strength by 10-15 % [30], but this has not been taken into account for later analyses.

As with the cylinder compression tests, the top and bottom surfaces of the cylinders were ground parallel and true prior to testing. Figure 5.10 shows a cylinder in the test machine and the five cylinders after testing. It can be seen that the cylinders are split in two nearly equal pieces, with a wedge-shaped piece forming at the top contact line. Table 5.6 shows the results obtained from the tests.

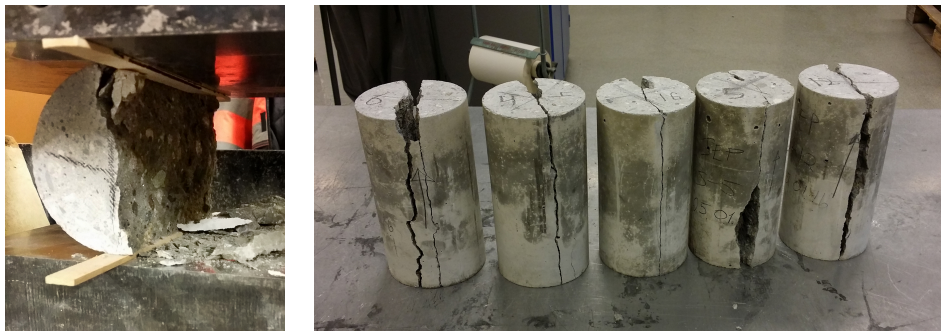

(a) *(b)*

Figure 5.10: *(a) Cylinder right after testing, and (b) all the five cylinders that were tested.*

Test	*Result* [MPa]
1	3.36
2	4.06
3	3.63
4	3.04
5	3.43
Average	3.50
Standard deviation	0.335

Table 5.6: *Tensile splitting strength of cylinders 29 days after casting.*

In addition to giving an estimated tensile strength of the concrete, the tensile splitting tests can also be used to evaluate the strength of the cement compared with the strength of the aggregates. From Figure 5.11, it is seen that a large fraction of aggregates have been split, meaning that the strength of the aggregates in this particular mix is not significantly higher than the strength of the cement matrix. However, it is clear that some high strength aggregates are present, as there are a moderate number of undamaged aggregates present. This serves as an example of the random nature of concrete.

5.4.4 Bending tests

At 84 days after casting, 3-point-bending tests were performed on three concrete beams of dimensions 100×100×600 mm. The span of the bending setup was set to 500 mm, and the load was applied at the midspan by enforcing a constant

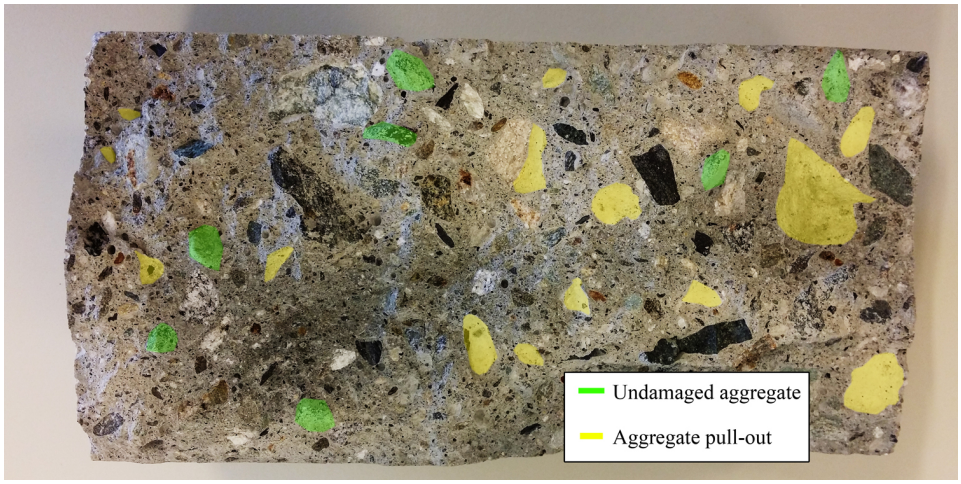

Figure 5.11: *Fracture surface of tensile splitting specimen. The places where undamaged aggregate is stuck in the concrete are highlighted green, while the places where aggregate has been pulled out are highlighted yellow.*

displacement velocity of 0.5 mm/min. A photo of the setup is shown in Figure 5.12a.

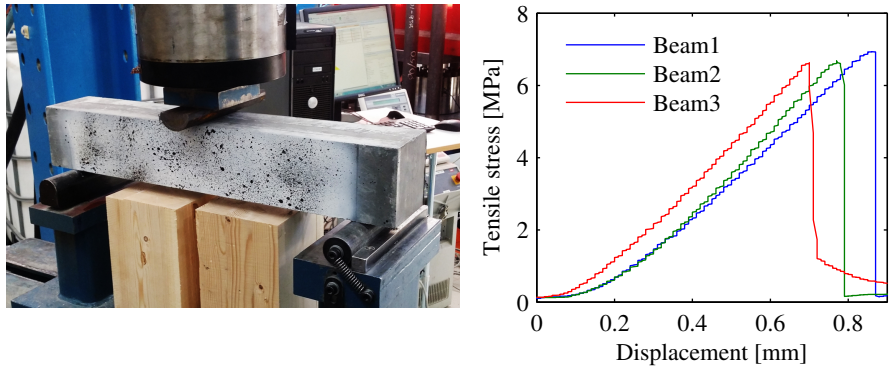

Figure 5.12: *(a) Setup of the 3-point bending tests and (b) the resulting stress-displacement curves.*

The beams failed by brittle fracture at a load of approximately 9 kN. Figure 5.12b shows the maximum tensile stresses in the beams plotted against the crosshead displacement of the test machine. The maximum tensile stress is given by the formula

$$f_t = \frac{3FL}{2Bh^2}, \tag{5.4}$$

where F is the load, L is the span and B and h are the width and height of the beam, respectively. It is immediately seen from the graph that the tensile strength in bending is almost twice as that achieved in the tensile splitting tests. This is normal, since the stress calculation in Equation 5.4 assumes that the stress is linear over the height of the beam, which is not fully correct [30]. It can also be partly attributed to the size effect, since there is only a small volume that is highly stressed. According to [30], the tensile strength may be overestimated by as much as 50-100 %, which is also reflected in these tests when compared with the tensile splitting tests.

The bending tests were filmed during testing, and two-dimensional *Digital Image Correlation (DIC)* was performed on the footage in order to measure the displacement and strain fields. Due to the small strains, the DIC was not able to capture the strain field prior to failure. It was still attempted to measure the displacement of the beams during testing, and the DIC displacement versus the crosshead displacement is plotted in Figure 5.13. In the same figure, the tensile stress has been plotted against the DIC displacement. It can be seen that the DIC displacement is more noisy than the crosshead displacement, and some unphysical behavior is seen for Beam 1 in the region from 4 MPa to 5 MPa tensile stress.

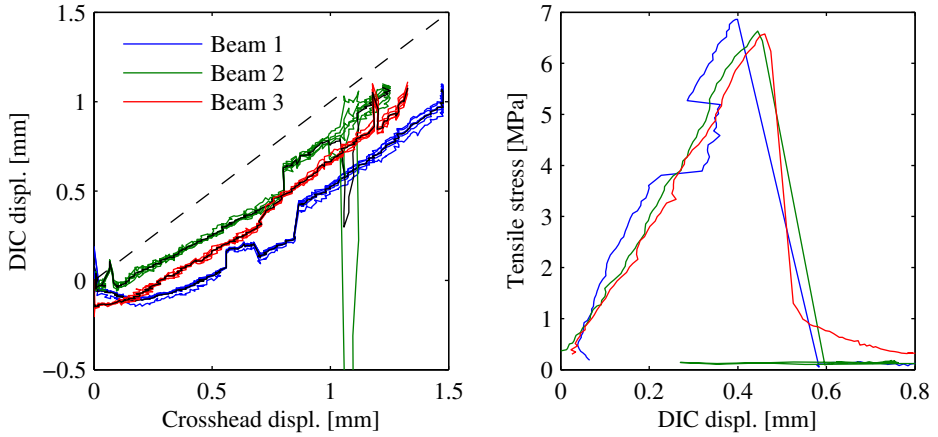

Figure 5.13: *On the left, the DIC displacement is plotted against the crosshead displacement. On the right, the tensile stress is plotted against the DIC displacement. The DIC displacement has been probed at 6 points directly below the load applicator, and the average of the 6 points have been used as the displacement in the figure to the right.*

From the stress-displacement curve in Figure 5.13, the elastic modulus can be estimated by linear regression. If the concrete is assumed to be isotropic and shear deformations are included, the deformation w is given by

$$w = \frac{FL^3}{48E_cI} + \frac{FL}{4A}\frac{2(1+\nu)}{E_c}, \tag{5.5}$$

where I is the second moment of area and A is the cross-sectional area of the beam.

Beam	*E* [MPa]	*Tensile strength* [MPa]
1	8042	6.93
2	6513	6.67
3	6079	6.62
Avg.	6878	6.74

Table 5.7: *Bending test results.*

The calculated elastic modulus is given in Table 5.7, as well as the tensile strength obtained from the bending tests. It is clear from these values that there is still significant compliance in the deformation measurements, since the elastic modulus is expected to be closer to 30 GPa.

5.5 Uniaxial testing of the rebar mesh

In order to determine the mechanical properties of the rebar mesh that was used in some of the concrete plates, uniaxial tension tests were performed. The following section will describe the experimental setup, present the test results and the resulting material data. In addition, two hardening models for the rebar mesh are calibrated.

5.5.1 Experimental setup

The rebar mesh consisted of approximately 2.5 mm thick steel wire. The squares had an approximate size of 75 mm, and the mesh was delivered in 1200 mm long and 800 mm wide sheets. Fourteen test specimens with an approximate length of 70 mm were cut with a wire-cutter plier from one such sheet. Six of the specimens were along the longitudinal direction of the mesh, while another six were along the transverse. Also, two specimens were cut such that the welded joint between the wires was included. Each specimen was clamped by serrated jaws in the test machine.

The diameter of the specimens was measured, and the diameter of each of them was taken into account individually when calculating the stress. There were some variations between the measurements, and it was found that the wires in the longitudinal direction were slightly thicker than in the transversal direction. Table 5.8 shows the average diameter in the two directions, as well as the standard deviation.

Direction	*Average diameter* [mm]
Longitudinal (0 deg)	2.603 ± 0.004
Transversal (90 deg)	2.573 ± 0.004

Table 5.8: *Diameter of the test specimens.*

A 100 kN Instron test machine was used to conduct the experiments. To measure the strain, an extensometer was fixed to the test specimen, measuring the strain all the way to failure. Figure 5.14 shows one of the test specimens installed in the test machine with the extensometer mounted to the left.

Figure 5.14: *Uniaxial tension test of reinforcement mesh.*

5.5.2 Test results

All the tests showed similar behavior up until necking. Since the neck formed outside the extensometer in some of the tests, the behavior after necking is not captured properly in these tests. The engineering stress versus the engineering strain is plotted in Figure 5.15.

It can be observed that the specimens show rather consistent behavior in the plastic region, with the exception of one test that was significantly weaker than the rest. This test was excluded from the calibration because the remaining tests showed consistent behavior. The welded specimens did not show any different behavior than the unwelded specimens in terms of strength, and were thus also excluded from the calibration.

All the specimens failed in ductile fracture, similar to the specimen shown in Figure 5.16. The diameter of the necks of the specimens were measured after they had been tested in order to determine the fracture strain, which in average was found to be 0.8796 ± 0.041.

5.5.3 Calibration of material models

Since some variation is present in the test data, it was decided to represent the average behavior of the test specimens. Using MATLAB, the part of the curves after necking was removed and the true stress - logarithmic strain curves were

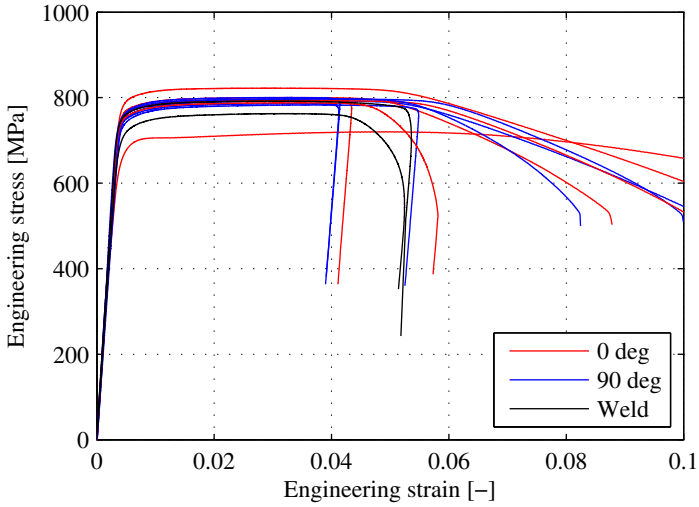

Figure 5.15: *Engineering stress - strain curves for all the 14 test specimens.*

calculated. Next, the elastic strains were subtracted to obtain the σ-ε_{pl}-curves for each specimen.

Based on the σ-ε_{pl}-curves, it was decided to represent the material behavior with a linear hardening model and a power law hardening model. The two models are formulated as follows:

$$\sigma_{eq} = \begin{cases} \sigma_0 + h_R \bar{\varepsilon^p} & \text{Linear hardening} \\ \bar{A} + \bar{B}\bar{\varepsilon^p}^{\bar{n}} & \text{Power law hardening} \end{cases} \tag{5.6}$$

where $\bar{\varepsilon^p}$ is the equivalent plastic strain and σ_0, h_R, $\bar{A}$, $\bar{B}$ and $\bar{n}$ are constants to be fitted.

The least-square curve-fitting tool *lsqcurvefit* was then used to fit the constants of the two functions. For the linear hardening model, only the data for plastic strains larger than 0.01 were used in the calibration because of the nonlinear behavior at lower plastic strains. The resulting curves are shown in Figure 5.17a, while the material constants are presented in Table 5.17b.

Using the commercial Finite Element code Abaqus, the tensile tests were modeled with both 2D-axisymmetric and a 1D-truss elements to verify that the material data obtained from physical testing would yield the correct behavior. The simulation results are shown in Figure 5.18. In both cases, the response is captured well for the linear hardening and power law hardening models up to necking. After necking, only the 2D axisymmetric power law model is able to recreate the response.

Figure 5.16: *Fractured test specimen.*

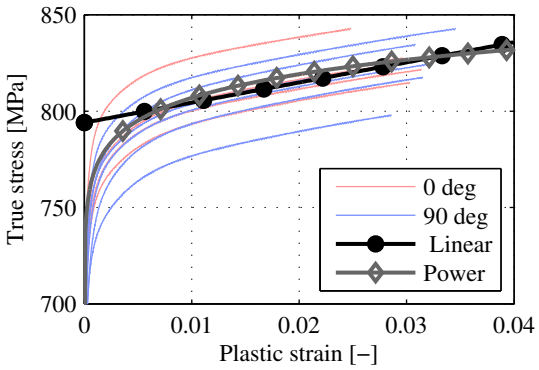

(a)

Material properties			
	σ_0	h_R	
Linear	794	1044	
	A	B	n
Power	348	566	0.044

(b)

Figure 5.17: *(a) Linear hardening and power law hardening fitted to the uniaxial test data and (b) material properties obtained from least-square fitting.*

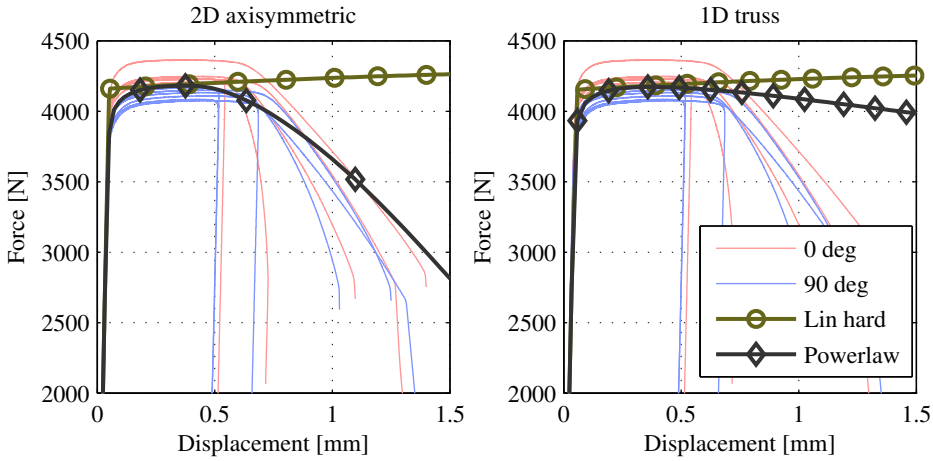

Figure 5.18: *Abaqus simulation of the tensile tests with the material data obtained above.*

5.6 Summary

In this Chapter, introductory experiments on concrete have been performed. The concrete mix has been tested, and concrete plates and test specimens have been created. Furthermore, material tests of the cured concrete have been conducted in order to determine its mechanical and stochastic properties. In addition, the rebar mesh has been subjected to uniaxial testing, and two material models were calibrated to the results. For convenience, a summary of the most central test results is given in Table 5.9.

Cured concrete	*Strength* [MPa]	*Standard deviation* [MPa]
Cube compression	46.35	0.73
Cylinder compression	39.62	0.747
Tensile splitting	3.50	0.335
Three-point bending	6.74	-
Rebar mesh	*Yield limit* [MPa]	*Fracture strain* [-]
Uniaxial tension	794	0.8796 ± 0.041

Table 5.9: *A summary of the most central test results.*

Chapter 6

Shock Tube Experiments

Four 50 mm thick concrete plates were tested in the shock tube facility at SIMLab at 49-50 days after casting. Two plates were subjected to shock waves with a peak reflected pressure of approximately 12 bar, and two were subjected to a higher pressure of around 17 bar. For each pressure level, one plate had a rebar mesh, while the other did not. This chapter will explain the experimental setup used for the tests, and present the test results in detail. An overview of the tests is given in Table 6.1.

Test name	*Reinforcement*	*Driver pressure*
P-41	×	41 bar
R-41	✓	41 bar
P-77	×	77 bar
R-77	✓	77 bar

Table 6.1: *Shock tube experiments overview. The test name character indicates if the plate is plain (P) or reinforced (R), while the number indicates the nominal driver pressure in the test, i.e. P-41 means a plain plate tested at a driver pressure of 41 bar.*

6.1 Experimental setup

Figure 6.1 shows a drawing of the shock tube seen from the side and from above. The shock tube facility at SIMLab features a 18.275 m long shock tube with a square internal cross section of 0.3×0.3 m. The pressure chamber, or driver, is 2.02 m long with a circular cross section where the internal diameter is 0.331 m. The length of the driver can be adjusted to obtain the desired driver volume, and in the following experiments it was set to 0.77 m. The pressurized air in the driver is contained by three sets of polymer membranes, all of which are separated such that two closed chambers are present between them. Upon filling the driver, the two intermediate chambers are filled to 2/3 and 1/3 of the driver pressure, causing

the pressure difference over one membrane set to be no more than 1/3 of the driver pressure. The shock tube is fired by venting the air in the intermediate chamber closest to the driver, causing the membranes to rupture. A series of pressure transducers measure the pressure as the shock front travels down the length of the tube. At 0.305 m and 0.295 m in front of the test specimen, pressure sensor 1 and 2 are mounted, as seen in Figure 6.1b. From these two sensors, the pressure profile of the shock wave can be measured. The pressure was sampled every 0.002 ms, equating to a sample rate of 500 kHz.

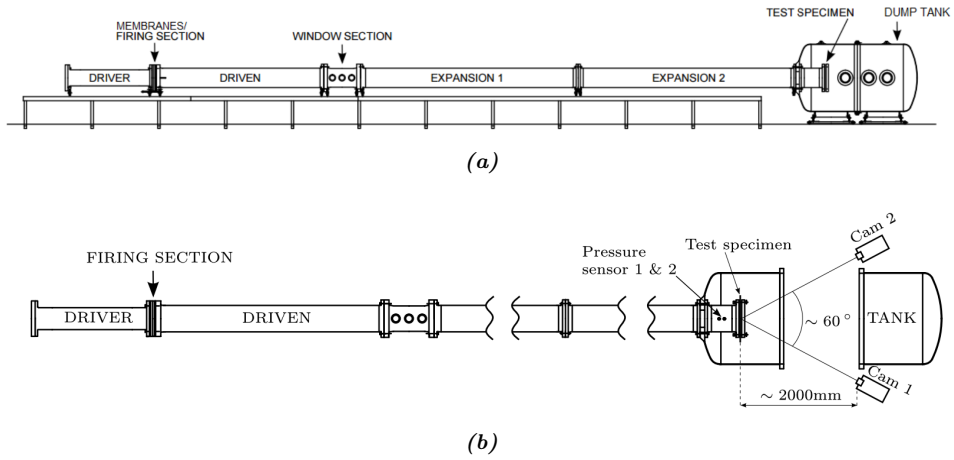

Figure 6.1: *Sketch of the shock tube seen from (a) the side and (b) above [17].*

The concrete plates were mounted to a flange on the shock tube inside the dump tank by 12 M24 bolts, as seen in Figure 6.2. The bolts were tightened using a spanner until the bolts were snug, with care taken not to crack the concrete plates. Prior to mounting in the shock tube, the concrete plates were painted with a speckle pattern, as seen in Figure 6.2b. This was done in order to use 3D-DIC to measure the deformation of the plates during testing. Two synchronized Phantom v1610 high speed cameras were placed such that they could film the concrete plates through the windows of the dump tank, and a single lamp inside the dump tank provided light for the cameras. A frame rate of 24 000 frames per second was used during the tests. Post-processing of the footage to obtain the deformation was performed in the 3D-DIC software *eCorr*.

From the pressure-time curves obtained by the pressure sensors closest to the concrete plate, the peak reflected pressure that acts on the plate could be determined. However, it is not as straightforward as reading the curves directly. First, the velocity of the incident shock wave must be calculated. This is found by dividing the distance between sensor 1 and sensor 2 by the time it takes for the shock wave to travel between them. When the shock wave velocity is known, the arrival time of the shock wave at the plate can be calculated. By performing least-square fitting on the measured pressure curve from one of the sensors, the parameters of the

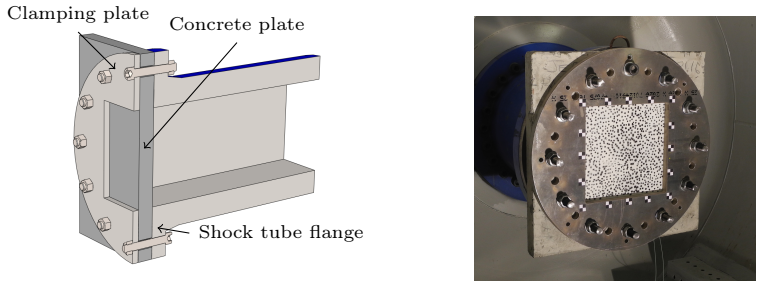

Figure 6.2: *(a) Section view of concrete plate mounted in the shock tube and (b) a plate mounted in the shock tube.*

Friedlander equation in Equation (3.1) are determined. The peak reflected pressure is then found by evaluating the Friedlander function at the time when the incident shock wave arrives at the concrete plate.

Haug and Osnes performed calibration runs of the shock tube in [4] where they replaced the test specimen with a rigid plate that was fitted with pressure sensors. They concluded that the procedure described above was in good agreement with the pressure measured at the rigid plate for driver pressures up to 40 bar, using a driver length of 0.27 m. Tests performed by Aune et al. [18], however, showed a significant deviation between the shape of the reflected shock wave and an ideal shock wave when using a driver length of 0.77 m and a driver pressure of 75 bar. This driver length and pressure is approximately what has been used in the high pressure tests in this thesis. Figure 6.3 shows two of the calibration tests performed by Aune et al., and it is clearly seen that the reflected pressure measured at the rigid plate deviates substantially from the Friedlander curve that has been extrapolated by the pressure data from the sensor closest to the test specimen (sensor 2). Also, it is seen that the deviation is mostly in terms of impulse, as the peak pressure is captured reasonably well. It will be argued in Sections 6.3 and 7.1 that, according to the loading regimes presented in Section 3.1.4, the concrete plates tested in this thesis are in the quasi-static domain. Thus, only the peak pressure should be of importance to the structural response. The pressure load extraction scheme presented above should therefore be representable in subsequent analyses, despite the deviation in impulse.

From the shape of the reflected pressure curves in Figure 6.3, it is clear that the shock wave does not develop fully for these combinations of pressures and driver lengths, as there are strong secondary reflections present right after the incident shock wave has hit the rigid plate. The secondary reflections are created when the reflected shock wave, which goes to the left in Figure 3.3, passes through the tail of the remaining shock wave as it goes towards the test specimen. Since the pressure is high in this region, the reflected shock wave slows down when travelling through

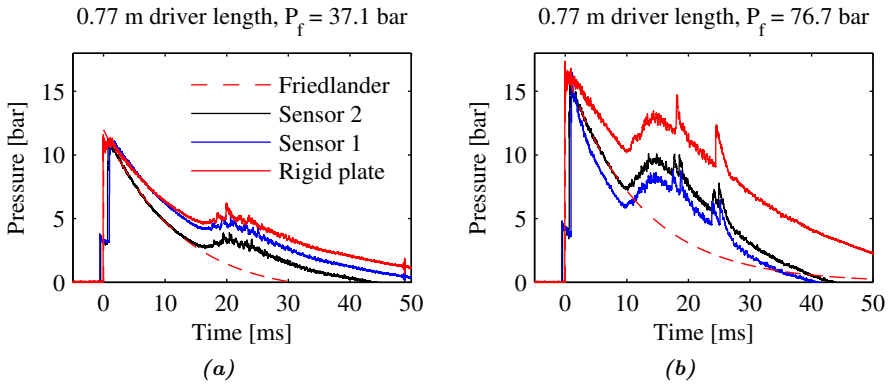

Figure 6.3: *Comparison between pressure profiles obtained by the pressure extraction scheme used in this thesis, and the real pressure measured at a rigid plate. These tests were performed by Aune et al. [18], with a driver length of 0.77 m and driver pressures P_f of 37.1 bar (a) and 76.7 bar (b).*

it, and a rarefaction wave forms in order to maintain pressure equilibrium [18].

During the tests, the momentum of the air moving at high velocity inside the shock tube causes rigid body movement of the shock tube. From the DIC, this movement was measured and subtracted from the displacement of the plate in order to get the deformation of the plate. The movement was measured at each corner of the clamping plate, and the mean of these measurements was used to correct the deformations measured at the concrete plate. In some cases the corner displacement measurements were noisy, so a moving average smoothing filter was used to smooth the data.

6.2 Test results

Table 6.2 shows the key figures for the blasts waves developed in the shock tube. The firing pressure P_f denotes the pressure in the driver at the moment when the membranes rupture. This pressure is markedly lower than the target pressures of 41 and 77 bar, since some pressure is lost due to leakage and venting of the intermediate chamber. The table also shows the TNT-equivalent hemispherical charge weight and standoff distance for the experiments, calculated from the Kingery & Bulmash empirical functions that were discussed in Section 3.1.2. The scaled distances Z indicate that the TNT-equivalent blasts are in the near-field domain, meaning that a blast of such magnitude would probably cause both local and global damage to a structure situated at the given standoff distance. It is clear, however, that such large explosive masses and standoff distances are not obtainable inside the SFT that is proposed for the Sognefjord crossing. The reason for the very high explosive masses and stand-off distances is because the positive impulses in the

experiments are quite large. If, by example, one fourth of the impulse is used in the calculations instead, the TNT-equivalent hemispherical blast for P-41 becomes a more realistic 950 kg at a stand-off distance of 18.7 meters. It should be noted that the impulses in the experiments have been calculated by integrating the fitted Friedlander curve since this is more representable of a real shock wave.

			Friedlander constants			*TNT-eq. hemispherical blast*		
	P_f	i_{r+}	P_r	t_+	b'	Z	W	R
Name	[bar]	[kPa*ms]	[bar]	[ms]	[-]	[m/kg$^{1/3}$]	[ton]	[m]
P-41	38.4	15720	12.05	54.22	2.74	1.9	60.7	74.7
R-41	39.5	15692	12.27	47.01	2.18	1.9	60.4	74.5
P-77	74.4	22419	16.55	45.92	1.84	1.7	123.7	84.7
R-77	72.7	19718	17.27	38.56	1.83	1.6	96.4	73.4

Table 6.2: *Key figures from the shock tube experiments.*

The pressure-time curves are shown in Figure 6.4. It can be seen that the Friedlander equation provides a reasonable approximation to the blast load in all the experiments, but a generally better fit is seen for the lower pressure tests. For the high pressure tests, the secondary reflections are more severe than for the tests at low driver pressure, causing the reflected pressure profile to deviate more from the ideal shock wave, as discussed above and in Section 3.1.1.

During the tests, it was observed that air leaked out from between the concrete plates and shock tube flange. This may also have caused the shock waves to deviate from ideal shock waves, and consequently introduces an uncertainty in the actual loading on the plates.

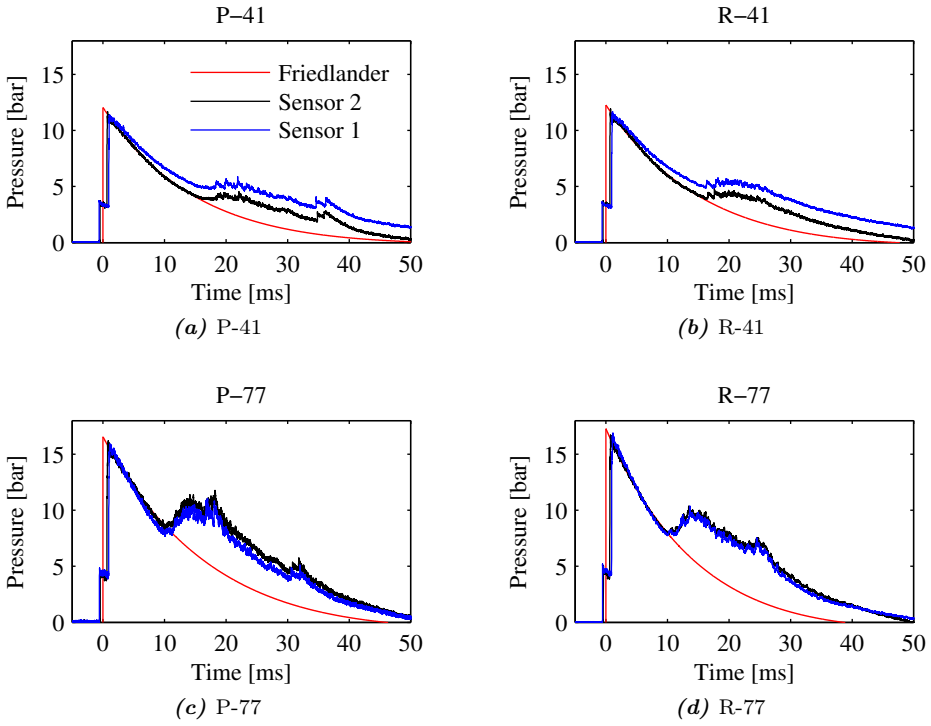

(a) P-41 *(b)* R-41

(c) P-77 *(d)* R-77

Figure 6.4: *Pressure-time curves from the shock tube experiments.*

6.2.1 Test 1: P-41

The first test was conducted on a plain plate, and it was carried out at a nominal driver pressure of 41 bar, resulting in a driver firing pressure of 38.4 bar. No surface cracks were observed prior to testing of this plate. Figure 6.5 shows the front and back of the plate after testing, where the cracks have been accentuated with red color for visibility.

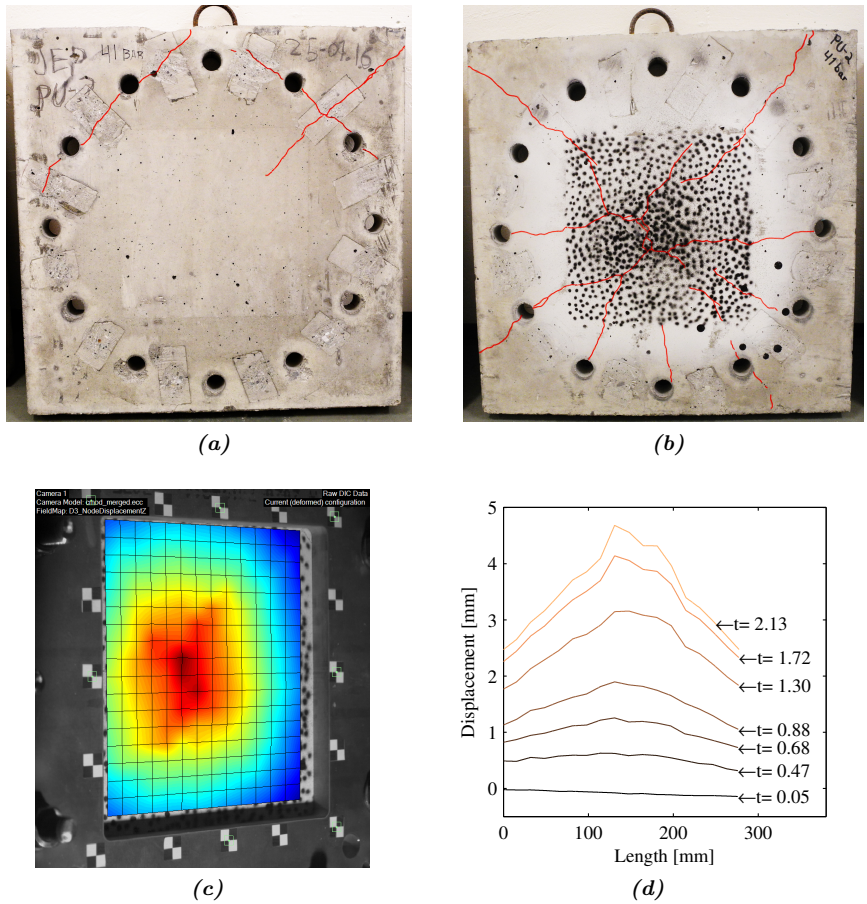

(a) *(b)* *(c)* *(d)*

Figure 6.5: *The (a) front and (b) back of plate P-41 after testing in the shock tube. (c) shows the displacement fringe of the plate at maximum displacement, while (d) shows how the deformation profile changes with time during the initial deformation.*

It can be seen that cracks propagated outwards from the center of the back of the plate, often going through the bolt holes. In the center of the plate at the back surface, a small piece of concrete detached from the plate. From the DIC contour plots, it can be seen that the maximum displacement is focused around

the area where the cracks coincide. Also, the displacement profiles in Figure 6.5d indicate that the plate behaved elastically up to around 0.68 ms after the shock wave impinged on the plate. After this point, all subsequent deformation was caused by opening of the cracks.

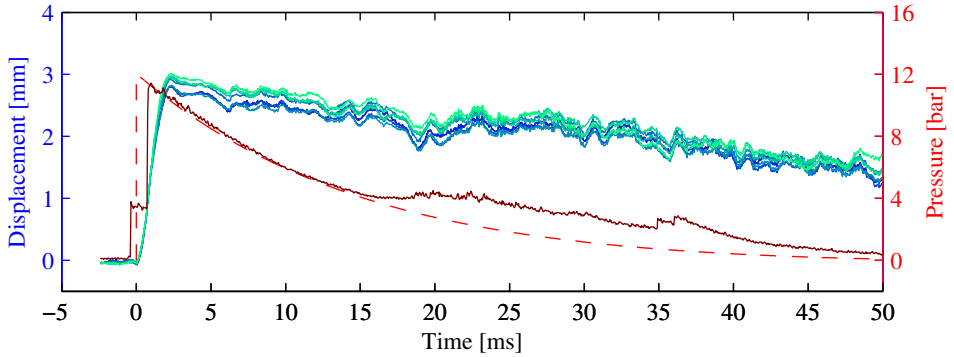

Figure 6.6: *Time vs. displacement from the DIC during test P-41. The displacement has been sampled at several points in the center of the plate, hence the many displacement curves.*

Figure 6.6 shows the center displacement of the plate together with the pressures from the test. The plate reached maximum deformation at t=2.13 ms after it was hit by the shock wave, followed by a steady decline in deformation as the pressure dropped.

6.2.2 Test 2: R-41

The second test was performed on a reinforced plate, using a nominal driver pressure of 41 bar. This resulted in a firing pressure of 39.5 bar. Before testing, some superficial cracks running along the reinforcement mesh were observed. These cracks were marked black, while the cracks that resulted from the test was marked red. Figure 6.7 shows the plate after testing, the deformation contours at maximum displacement, the deformation profiles during initial loading and the displacement-time relation for the center of the plate. In should be noted that the time-displacement curve in Figure 6.7e has been shifted 1 ms to the right in relation to the pressure curve, as there was an error with the synchronization between the pressure data and images in this particular experiment.

The crack patterns that developed during this test differ from the unreinforced plate in that many of the cracks run along the reinforcement mesh. Moreover, the maximum deformation is less for the reinforced plate than the unreinforced plate, however the overall behavior is similar. The plate seems to behave elastic initially, before cracking occurs and subsequent deformation is due to the cracks opening.

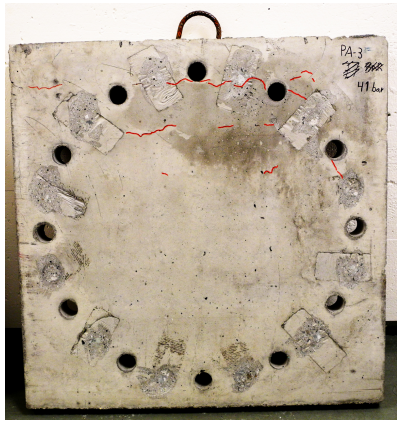

(a)

(b)

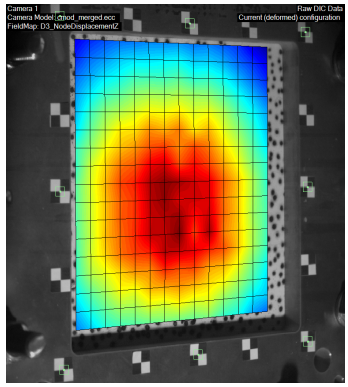

(c)

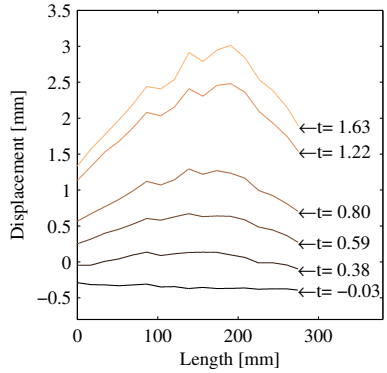

(d)

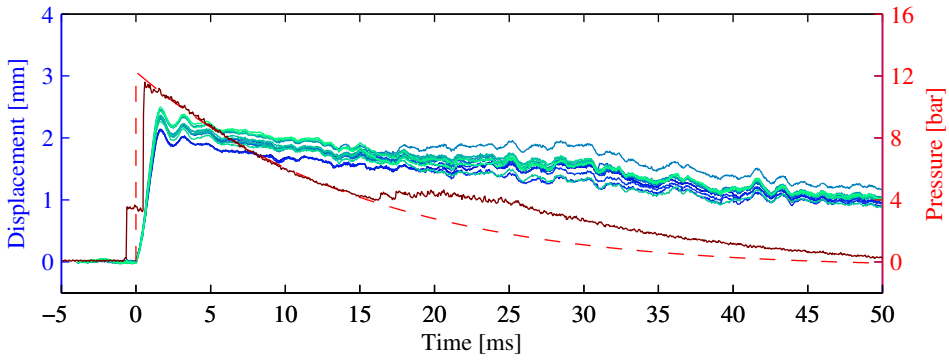

(e)

Figure 6.7: *The (a) front and (b) back of plate R-41 after testing in the shock tube. The displacement contours are shown in (c), and (d) shows the deformation profiles during the initial deformation. The center displacement and pressure histories are seen in (e).*

6.2.3 Test 3: P-77

Test number three was conducted on an unreinforced plate with a nominal driver pressure of 77 bar, which resulted in a firing pressure of 74.4 bar. This plate initially had numerous thin surface cracks which were marked green to distinguish them from the cracks resulting from the blast load. The final crack pattern is shown in Figure 6.8, in which the deformation contours at maximum displacement and the deformation profiles during loading are also included. The displacement-time and pressure-time curves are shown in Figure 6.9.

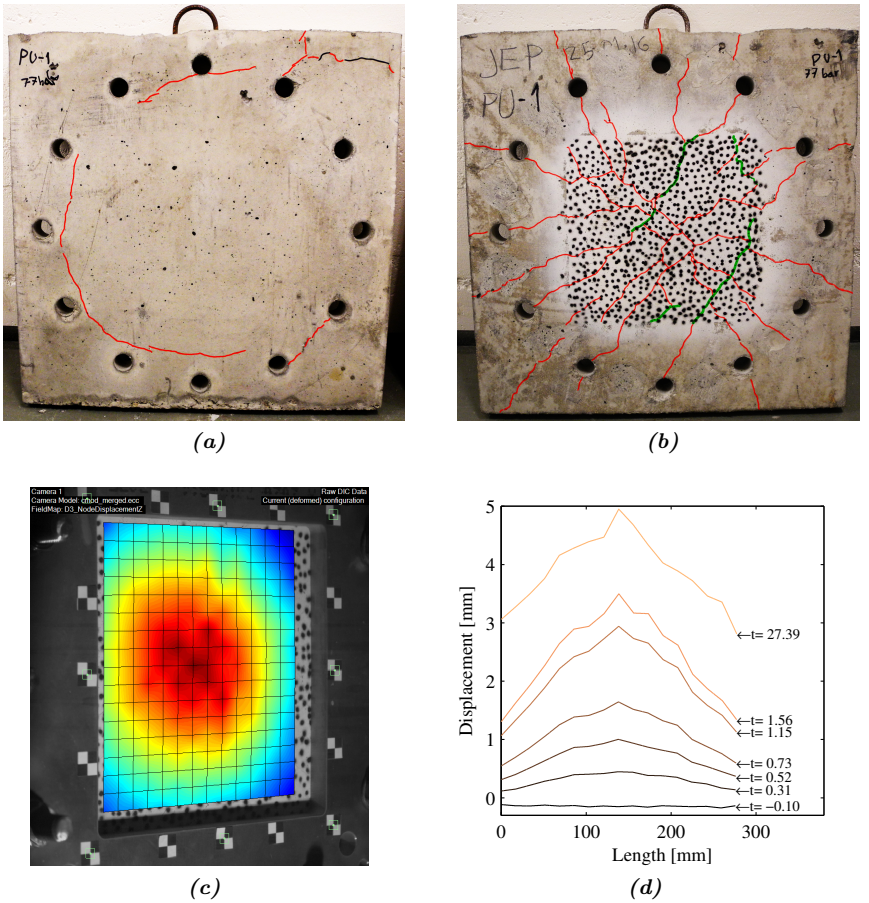

Figure 6.8: *The (a) front and (b) back of plate P-77 after testing in the shock tube. The displacement contours are shown in (c), and (d) shows the deformation profiles during the initial deformation.*

Much more cracks developed at the back surface of the plate in this test than for P-41. Also, a long, continuous crack formed along the bolt holes at the front surface.

From the displacement plot, it can be seen that this plate behaved differently than the two previous tests, in that the displacement increased slowly after the shock wave hit the plate. The reason for this behavior it not known, but some possible culprits will be discussed later in this chapter.

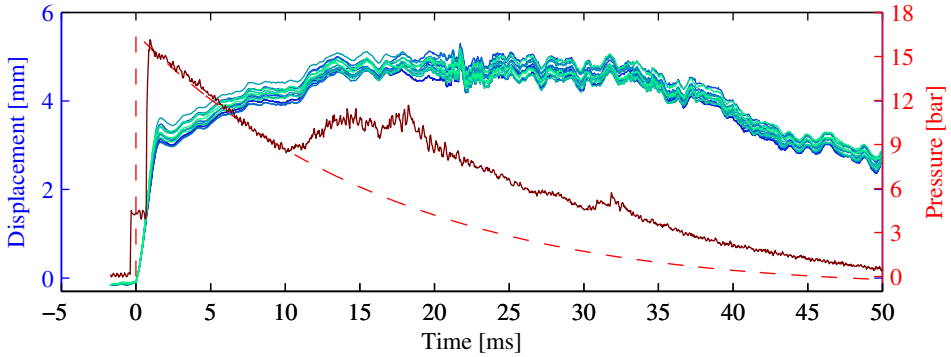

Figure 6.9: *Displacement and pressure histories for experiment P-77. The displacement has been sampled at several points in the center of the plate, hence the many displacement curves.*

6.2.4 Test 4: R-77

In the last experiment, a reinforced plate was tested at a nominal driver pressure of 77 bar, which gave a firing pressure of 72.7 bar. During demoulding of this plate, the lifting point was overloaded and broke loose from the plate. Nevertheless, it was decided to proceed with the test as planned, as it was thought that this would not influence the strength of the plate otherwise. Some superficial cracks which ran along the reinforcement mesh were also present in this plate, and these were marked green as previously.

From Figure 6.10, it is seen that the amount of cracking at the back surface is actually less for this test than it was for the reinforced plate at 41 bar driver pressure in test 2. At the front surface, however, the extent of cracking is more severe than in the lower pressure test. The deformation profiles during the initial deformation are similar to the profiles observed in the previous tests, but the midpoint deformation continues to increase slowly after the shock wave has hit, similar to what was observed in P-77.

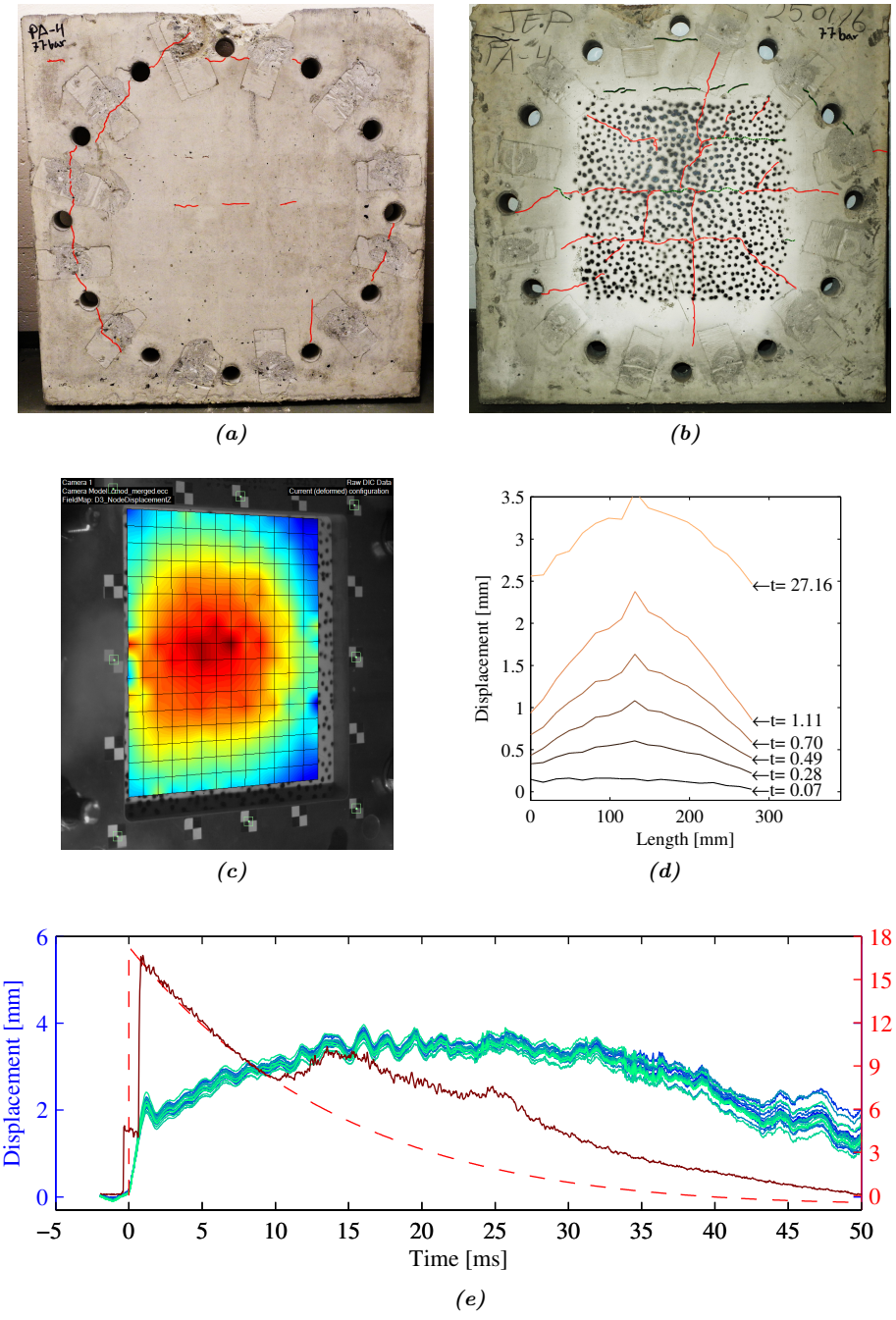

Figure 6.10: *The (a) front and (b) back of plate R-77 after testing in the shock tube. The displacement contours are shown in (c), and (d) shows the deformation profiles during the initial deformation. The center displacement and pressure-time relation is seen in (e).*

6.3 Discussion

Four concrete plates have been subjected to shock waves in the shock tube facility at SIMLab. None of the plates suffered catastrophic failure or developed through-cracks, which was surprising since Haug and Osnes [4] performed similar experiments with a stronger concrete, yet still got more damage. In particular, more damage was expected for P-77, as Haug and Osnes achieved deep cracks when they tested their B45 concrete plates with a driver length of 0.77 m and driver pressure of 75.2 bar. They did, however, achieve a slightly higher peak reflected pressure of 18.78 bar, compared with 16.55 bar in experiment P-77. Also, Haug and Osnes used a steel clamping plate, as opposed to an aluminium clamping plate, which may have produced slightly different boundary conditions. It still appears though, judging from the extensive amount of cracking in P-77, that P-77 may have been very close to collapse in the test.

In all the experiments, the plates are seen to respond fairly quickly to the load. Qualitatively, in light of the blast load regimes that were discussed in Section 3.1.4, it seems that the load regime can be categorized as quasi-static for the plates studied in this thesis. Hence, the deviation in impulse for the fitted Friedlander curves and the measured pressures should not have much influence on the response of the plates in later analyses. Moreover, from the DIC displacement profiles and crack patterns, it appears that damage is induced mainly by flexural bending.

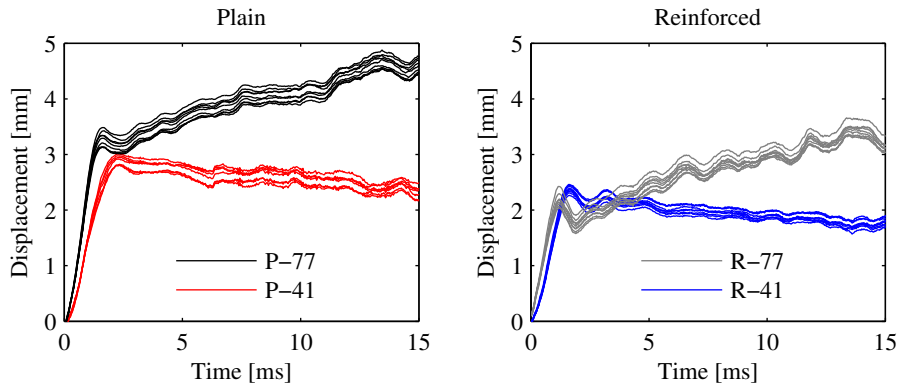

Figure 6.11: *Comparison between the plain and reinforced plates subjected to 41 bar and 77 bar driver pressure.*

Comparing the plain and reinforced plates, it was observed that the reinforced plates were stiffer and developed less cracks than the plain plates. Moreover, the tests at 77 bar caused a different displacement response than the 41 bar tests. This is readily seen in Figure 6.11, where the magnitude of the initial response in both plates is similar at both pressures, but for the high pressure tests the displacement increases steadily after the plates have been hit by the shock wave. The reason for this behavior is not known, but one possible explanation will be presented below.

Furthermore, there is a very small difference in initial deformation for the high and low pressure tests, and for the reinforced plates the initial deformation is actually smaller than for the high pressure test. This behavior was not expected, and the reason for this is not known either.

Figure 6.12a shows the rigid body movement of the shock tube during the four tests. It is seen that the shock tube moves much more during the 77 bar tests than the 41 bar tests, and that the shock tube retracts up to 5 mm right after the shock wave has hit the concrete plates. One possible explanation for the steady increase in displacement for the 77 bar tests may thus be that the concrete plates experience inertial forces during the retraction of the shock tube. Figure 6.12b shows the uncorrected displacement of the center of P-77, in addition to the shock tube displacement. It can be seen that the shock tube retracts at a faster rate than the concrete plate.

Another explanation may be that the plates become more damaged in the 77 bar tests, and that the pressure following the shock wave consequently causes further damage growth in the plates. However, this seems unfeasible since the amount of cracks in the two reinforced plates was almost the same, indicating an equal amount of damage.

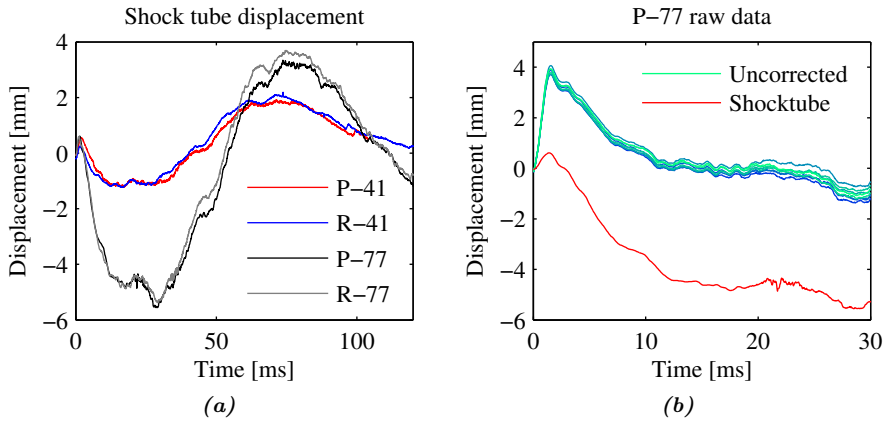

Figure 6.12: *The rigid body movement of the shock tube during the different tests is seen in (a), while (b) shows the uncorrected displacement at the center of P-77 in addition to the corresponding shock tube displacement.*

It is also possible that the strange behavior is due to errors in the DIC-measurements. Still, given that the calibration is good, the DIC technique is known to give excellent results, as shown by Aune et al. [18]. The DIC is calibrated by taking a set of images of a cylinder with a checkerboard pattern. By drawing a mesh that coincides with the lines of the checkerboard, the DIC software can calculate the calibration constants. This is done for both cameras, and since the diameter of the cylinder and the size of the checkerboard squares are known, the DIC software can

calculate the deviation between the theoretical position and measured position of the checkerboard squares. This deviation is called the residual, and indicates how well the calibration is done. The mean residuals in the calibrations performed in the experiments above were in the region 0.11-0.18 mm, meaning that the accuracy of the deformation measurements should also be in this region.

The many uncertainties in the shock tube tests may also have contributed to some of the unexpected behavior seen in the tests. The uncertainties include, but are not limited to:

- The clamping force on the concrete plates was not directly controlled, since the bolts were not torqued accurately.
- Some of the plates may have been pre-damaged or have had internal defects.
- Leaking air between the concrete plates and shock tube flange may have had an effect on the actual load on the plates.
- It has been assumed that the shock tube only moves axially during the tests when subtracting the shock tube rigid body movement. In reality, the shock tube may also have moved in other directions, causing error when correcting the DIC-measurements for the shock tube displacement.
- The cameras may have been inadvertently moved after the calibration pictures were taken, thus causing a loss of accuracy in the DIC-measurements.

Chapter 7

Preliminary Analysis

Before full analysis of the concrete plates was initiated, different aspects of the problem were looked into. In order to get a better understanding of the behavior of the plates, analytical calculations with different boundary conditions (BC) were performed on both the reinforced and unreinforced plates. Moreover, yield line analysis was conducted to study the residual capacity of the reinforced plates, before the boundary conditions were further investigated by doing a simple analysis of the full shock tube clamping assembly in Abaqus/Standard. The behavior of the two concrete models was investigated by simulating the material tests in Chapter 5, and comparing the simulations to the experimental results. Finally, two stochastic methods were developed by the authors as an attempt to recreate the stochastic nature of concrete in the simulations.

7.1 Analytical calculations

The static behavior of the concrete plates has been calculated using three methods. In the first method, a double cosine expansion is employed to calculate the elastic deformation and stress fields for a fully clamped plate. The second method uses a sine series expansion to do the same for a simply supported plate. Lastly, the yield line method is used to calculate the plastic behavior, by assuming that cracks will develop during loading and that all subsequent deformation is concentrated in these cracks.

7.1.1 Clamped plate

In plate theory, a distinction is made between thin and thick plates. Usually, the plate is considered to be thin when the thickness-to-width ratio h/a is less than 1/20. In this case, out-of-plane shear deformations can be neglected, simplifying

the calculations a great deal. While this requirement is not fulfilled for the concrete plates studied in this thesis, the following calculations will still use the thin plate assumption. For the small deformations considered, it is assumed that thin plate theory is sufficiently accurate for an engineering estimate.

The differential equation for a thin, isotropic plate subjected to uniform pressure q_0 can be expressed as

$$\frac{\partial^4 w}{\partial x^4} + 2\frac{\partial^4 w}{\partial x^2 \partial y^2} + \frac{\partial^4 w}{\partial y^4} = \frac{q_0}{D} \tag{7.1}$$

where D is the plate stiffness given by

$$D = \frac{E_c h^3}{12(1-\nu^2)} \tag{7.2}$$

and $w = w(x, y)$ is the transverse deformation field. E_c is the elastic modulus of the concrete and h is the plate thickness. The boundary conditions for a clamped plate are given as

$$w = 0 \text{ and } \frac{\partial w}{\partial n} = 0 \tag{7.3}$$

along the edges, where $\frac{\partial w}{\partial n}$ denotes the slope of the deformation perpendicular to the edges of the plate.

A solution to this differential equation can be expressed as a cosine series on the form:

$$w(x, y) = \sum_{m=1}^{M}\sum_{n=1}^{N}(1 - \cos(2m\pi x/a))(1 - \cos(2n\pi y/b))w_{mn}, \tag{7.4}$$

where a and b is the length and width of the plate, respectively. The coefficients w_{mn} can be found by minimizing the potential energy of the system. The detailed solution procedure can be found in [52], and will not be presented here.

To account for the steel rebar, the plate stiffness in Equation (7.2) must be modified. A very simple way of doing this is to consider the rebar to be a thin plate of equal volume as the reinforcements in that plane. For a square plate of width a, with n rebar wires in each direction and diameter d_r of each rebar wire, the thickness of the equivalent plate thus becomes

$$h_{r,eq} = \frac{n\pi d_r^2}{2a}. \tag{7.5}$$

For the rebar mesh, it is assumed that strain in one direction does not lead to strain in the other direction, i.e. $\nu = 0$. The plate stiffness D_r of two such equivalent rebar plates placed at distance l symmetrically around a mid-plane is given by

$$D_r = 2\int_l^{l+h_{r,eq}} E_s z^2 dz = \frac{2}{3}E_s\left((l + h_{r,eq})^3 - l^3\right), \tag{7.6}$$

where E_s is the elastic modulus of the steel. The reinforced plate stiffness D' is then found by taking the sum of Equations (7.2) and (7.6). It is emphasized that this method does not account for any local stresses introduced by the rebar, but merely increases the overall stiffness of the plate.

The stress components of the plate are calculated as [53]

$$\sigma_x = -\frac{zE_c}{1-\nu^2}\left(\frac{\partial^2 w}{\partial x^2} + \nu\frac{\partial^2 w}{\partial y^2}\right) \tag{7.7}$$

$$\sigma_y = -\frac{zE_c}{1-\nu^2}\left(\frac{\partial^2 w}{\partial y^2} + \nu\frac{\partial^2 w}{\partial x^2}\right) \tag{7.8}$$

$$\tau_{xy} = -\frac{zE_c}{1+\nu}\frac{\partial^2 w}{\partial x \partial y}, \tag{7.9}$$

and the principal stress direction is given by [54]

$$\tan 2\theta_p = \frac{2\tau_{xy}}{(\sigma_x - \sigma_y)}, \tag{7.10}$$

where θ_p is the principal stress direction. Finally, the principal stresses are given by

$$\sigma_{1,2} = \frac{\sigma_x + \sigma_y}{2} \pm \sqrt{\left(\frac{\sigma_x - \sigma_y}{2}\right)^2 + \tau_{xy}^2}. \tag{7.11}$$

By implementing these calculations in MATLAB, the elastic response of the plain and reinforced concrete plates can be compared. Also, the elastic stresses in the plate can be plotted, as well as the principal stresses and principal stress directions.

Figure 7.1 show the 1st principal stresses and stress directions obtained from the double cosine series expansion. At the front of the plate, the maximum tensile stress occurs at the middle of the clamped edges in the direction perpendicular to the edge. At the back, the maximum tensile stress occurs in the center of the plate, perpendicular to the diagonals of the plate. The crack patterns observed in the experiments are not fully consistent with the crack pattern predicted by the analytical calculations, as there are few cracks along the boundary at the front surface, where the 1st principal stress is predicted to be the highest. This may be because the concrete plate is not fully clamped as assumed in these calculations.

Table 7.1 summarizes the calculation results. For the B20 concrete that has been used in this thesis, adding reinforcements gives a 7.9% increase in stiffness. Because the stress scales linearly with the magnitude of the displacement, this also means that the overall stress is reduced by 7.9% everywhere. The cracking pressure, which is defined by the authors as the static pressure required to reach a principal tensile stress equal to the tensile strength acquired in the 3-pt bending tests, is 6.19 bar for an unreinforced plate and 6.64 bar for a reinforced plate. This means that for pressures below 6 bar, the plate will likely not develop any visible cracks, assuming that the plate is in fact fully clamped.

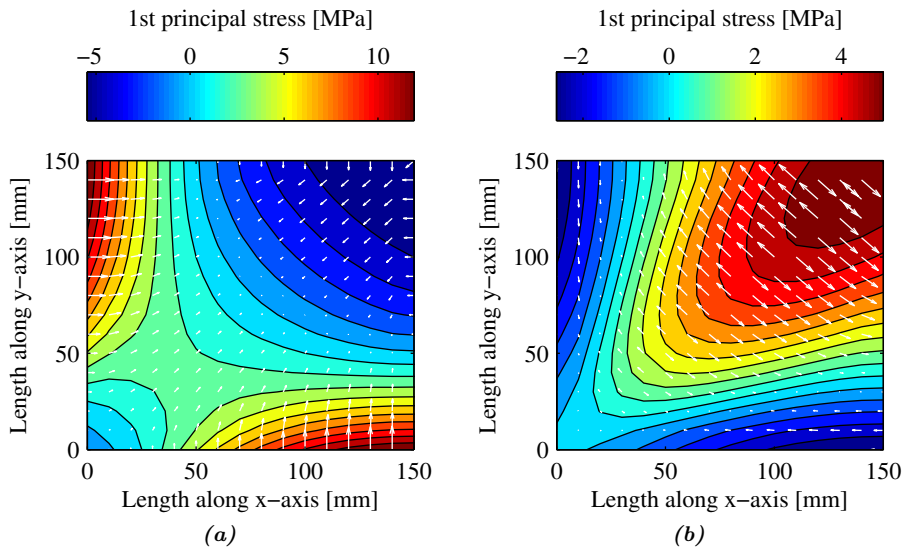

Figure 7.1: *First principal stress and corresponding stress directions at (a) the front surface and (b) the back surface of a plain concrete plate subjected to a static pressure of $P = 12$ bar. The figures only show the bottom left quarter of the plates due to symmetry.*

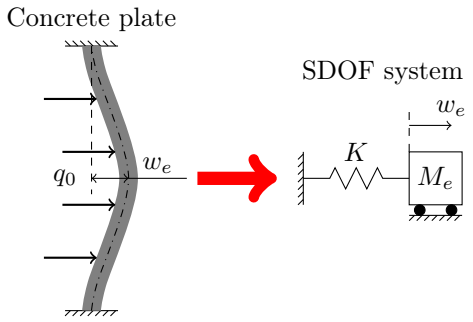

Figure 7.2: *Equivalent SDOF-system for the plate bending problem.*

The analytical displacement field can also be used to estimate the natural frequency of the plate by considering the plate as a single-degree-of-freedom (SDOF) model, as illustrated in Figure 7.2. By using the midpoint displacement as the only DOF, the equivalent SDOF stiffness K can be found by setting the external work equal for the same displacement in the two systems, such that

$$\frac{1}{2}Kw_e^2 = \frac{1}{2}\iint_A q_0 w(x,y)\,dxdy \tag{7.12}$$

where q_0 is the pressure acting on the plate. Recalling that q0 is constant over the

plate, the stiffness K is found by rearranging Equation (7.12), and becomes

$$K = \frac{q_0}{w_e^2} \iint_A w(x,y)\, dxdy. \tag{7.13}$$

The equivalent mass M_e can be calculated by demanding that the kinetic energy of the two systems is equivalent for the same midpoint velocity, i.e.

$$\frac{1}{2} M_e \dot{w_e}^2 = \frac{1}{2} \iint_A m(x,y) \dot{w}(x,y)^2 \, dxdy. \tag{7.14}$$

Assuming small displacements, the velocity $\dot{w_e}$ can be approximated by

$$\dot{w_e} = \frac{w_e - 0}{\Delta t} \tag{7.15}$$

where Δt is a small time increment. The deformation velocity field of the plate can be approximated the same way such that Δt vanishes on both sides. M_e is then given by

$$M_e = \frac{\rho h}{w_e^2} \iint_A w(x,y)^2 \, dxdy. \tag{7.16}$$

The double integrals in Equations (7.13) and (7.16) can be evaluated numerically in MATLAB, and the effective stiffness and mass can thus be found. Finally, the natural vibration period can be calculated by the formula [55]

$$T = 2\pi \sqrt{\frac{M_e}{K}}. \tag{7.17}$$

Table 7.1 shows the calculation results for the clamped plate. The natural vibration period T is found to be 0.297 ms and 0.287 ms for an unreinforced and reinforced plate, respectively. In Section 3.1.4, the different loading regimes for blast loads were discussed, and a relation between the loading regime and the ratio of load duration to natural vibration period was presented. From the shock tube experiments it was found that the load duration t_d was around 45 ms, and since $t_d/T \approx 150$, it can thus be concluded, given fully clamped BCs, that the load is in the quasi-static domain.

7.1.2 Simply supported plate

While the setup of the shock tube is such that the plate should be fully clamped, the case of a simply supported plate has also been investigated for comparison. The clamped and simply supported plate calculations may thus serve as an upper and lower bound for the elastic response of the plates. In the case of a simply supported plate, the boundary conditions in Equation (7.3) read instead:

$$w = 0 \ , \ \frac{\partial^2 w}{\partial x^2} = 0 \text{ and } \frac{\partial^2 w}{\partial y^2} = 0 \tag{7.18}$$

along the boundaries. A solution to this problem is given as [53]

$$w(x,y) = \sum_{m=1}^{M}\sum_{n=1}^{N}(\sin(m\pi x/a))(\sin(n\pi y/b))w_{mn}, \tag{7.19}$$

where for an isotropic plate subjected to uniform pressure, w_{mn} is given by

$$w_{mn} = \begin{cases} \frac{16q_0}{Dmn\pi^6\left(\frac{m^2}{a^2}+\frac{n^2}{b^2}\right)^2} & m \text{ and } n \text{ odd}, \\ 0 & m \text{ or } n \text{ even}. \end{cases} \tag{7.20}$$

The resulting 1st principal stress fields at the front and back surfaces of the plate subjected to $P = 12$ bar are shown in Figure 7.3. It is seen that the tensile stress at the back of the plate is much higher for this case than for the clamped plate in the previous section, which is more in agreement with the pattern observed in the experiments. Still, the correct boundary conditions are probably somewhere in between, as some cracks also have formed on the front of the plate where there should be little stress according to the simply supported plate calculations.

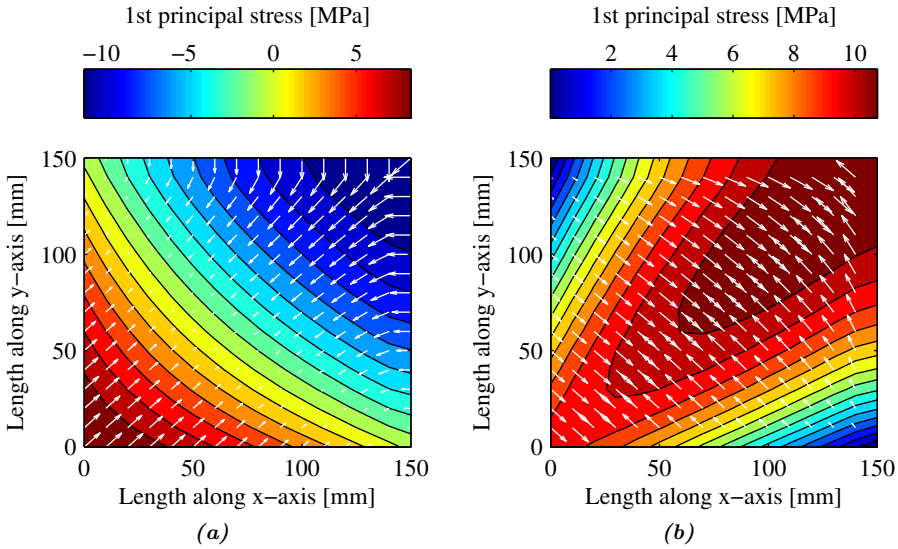

Figure 7.3: *First principal stress and corresponding stress directions at (a) the front surface and (b) the back surface of a simply supported plate subjected to a pressure of $P = 12$ bar.*

The stiffness of a simply supported plate is seen to be much less than that of a fully clamped plate, as seen in Table 7.1. Cracks are predicted to form at a static pressure of around 7 bar for an unreinforced plate, and around 7.5 bar for a reinforced plate. The ratio t_d/T is in the order of 80 for an unreinforced simply supported plate, which means that the blast response is in the quasi-static regime. Also, by the classification in Section 3.1.4, the plates will be in the quasi-static domain for load durations longer than minimum 3.5 ms.

BC	*Reinforced*	*Plate compliance* [μm / bar]	*Cracking pressure* *Front* [bar]	*Back* [bar]	T [ms]
Clamped	×	3.1485	6.19	14.77	0.297
Clamped	✓	2.9310	6.64	15.86	0.287
Pinned	×	10.1084	-	7.06	0.548
Pinned	✓	9.4100	-	7.58	0.528

Table 7.1: *Maximum displacement per bar static pressure (compliance) and static cracking pressures, assuming a bending tensile strength of 6.74 MPa and an elastic modulus of 30 GPa for the concrete. T denotes the natural vibration period of an equivalent SDOF system.*

7.1.3 The yield line method

It is possible to determine the ultimate load capacity of reinforced concrete plates by means of limit analysis. When concrete cracks due to excessive deformation, a redistribution of loads from the concrete to the rebar mesh occurs. Plastic hinges will form in the areas where tensile stresses are sufficiently high to cause yielding in the steel. With further loading, yielding will spread along the paths of least resistance, forming yield lines, or rather plastic hinge lines. It is assumed that the entire load is carried along these lines, thus the plate will collapse once the maximum plastic moment capacity has been reached in all of them. In order to determine the ultimate load and the distribution of moments at that load, either a lower bound or an upper bound method may be used [56]. In this project, the upper bound method known as the yield line method has been employed.

For a given plate with a set of boundary conditions, various collapse mechanisms (i.e. yield line patterns) are proposed. The ultimate load for each configuration is computed using either the principle of virtual work or force equilibrium, and the weakest solution is the correct one. Being an upper bound method, the yield line method gives an ultimate load that is either correct or too high [56], thus it is vital to ensure the correct collapse mechanism is proposed. In the case of square and fully clamped concrete plates, the yield pattern is well known. An illustration is given in Figure 7.4. See [56, 57] for more information regarding the method and the underlying theory.

In Pladeformler [58], Johansen presents formulae covering several different static concrete plate problems, including the one given in Figure 7.4. For convenience, the yield line analysis performed in this project has been based on this formulae, whereof the most important equations are presented subsequently.

$$P_u = 8m_p \left(\frac{1 + \frac{b_r}{a_r} + \frac{a_r}{b_r})}{a_r b_r} \right), \tag{7.21}$$

where P_u is the ultimate load, m_p is the maximum plastic moment capacity, and a_r and b_r are referred to as reduced sides, given by:

$$a_r = b_r = \frac{a}{\sqrt{(1+i)}} = \frac{a}{\sqrt{2}} \tag{7.22}$$

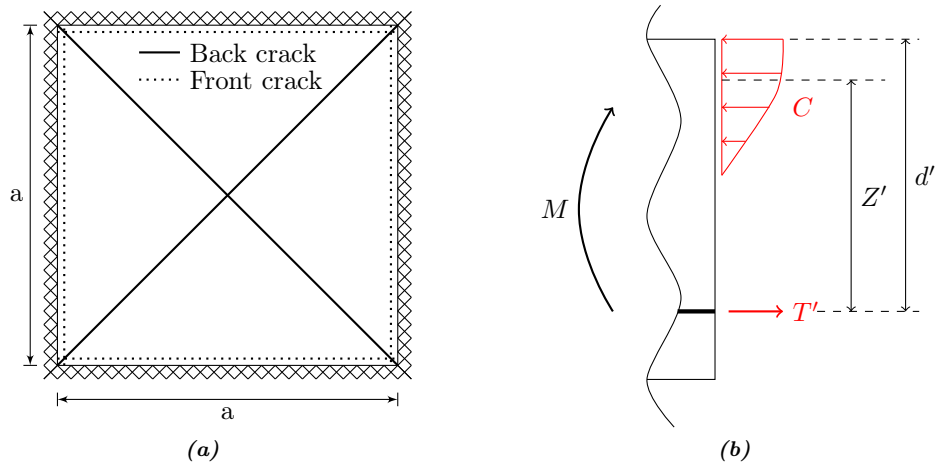

Figure 7.4: *The yield line pattern for a fully clamped, square concrete plate with side lengths a is shown in (a). This pattern is in agreement with the stress field obtained with plate theory in Figure 7.1b. In (b), the assumed stress distribution over the thickness of the reinforced concrete plate is shown. Note that it is assumed that the rebar in compression carries no load, and that the concrete has no tensile strength after initial cracking.*

when $i = 1$, which is the case for fully clamped plates. The only remaining unknown parameter in Equation (7.21) is the maximum plastic moment capacity m_p. A quick and simplified calculation, based on moment equilibrium [59], can be done through the relation:

$$m_p = T'Z' \tag{7.23}$$

where

$$T' = A_s\sigma_0 \tag{7.24}$$

and

$$Z' \approx 0.9d', \tag{7.25}$$

in which A_s is the total reinforcement cross section area, σ_0 is the steel yield stress, T is the tensile stress in the rebar mesh, while d' is the distance between the rebar mesh and the plate side furthest away. See Figures 7.4 and 5.3 for information regarding the plate geometry. Results from the yield line analysis are presented in Table 7.2.

Moment capacity m_p [kNm/m]	P_u [bar]
0.611	3.26

Table 7.2: *Results from the yield line analysis.*

The yield line analysis predicts a plastic capacity that is much lower than the elastic capacity calculated using plate theory. Beyond this, it is difficult to draw

any further conclusions from the result. Moreover, since the plates in the shock tube experiments were not damaged enough to develop the yield line pattern proposed in this calculation, the yield line method will not be pursued any further in this thesis.

7.2 A closer look at the boundary conditions

From the analytical calculations in the previous section, it is clear that the assumption that the concrete plates are fully clamped in the shock tube assembly may not be fully accurate. In particular, the clamped plate assumption should consistently lead to more severe cracking at the side of the plate facing the shock wave, but this was neither observed in the experiments conducted by Haug and Osnes [4] in 2015, nor in the experiments in this thesis. Because of this, it was decided to do a more detailed analysis of the boundary conditions.

The whole plate clamping assembly was thus modeled in Abaqus, including contact definitions and bolt preload. The concrete plate was modeled as a purely elastic plate, and was assigned an elastic modulus of 30 GPa and a Poisson number of 0.2. Contact was defined between the bolt heads and the clamping plate, between the clamping plate and concrete plate and between the concrete plate and shock tube mounting flange, all with a frictional coefficient of 0.2. The bolts were tied to the inside surface of the bolt holes in the shock tube flange, and were given a preload of 31.5 kN, which equates to around 150 Nm of tightening torque. This preload is only an estimate, since the actual preload is not known. The Abaqus/Standard solver with nonlinear geometry was used for solving. The bolt preload was applied in the first analysis step, before a uniform pressure of 10 bar was applied to the loaded surface of the concrete plate. Table 7.3 shows the element types and sizes used in the simulation.

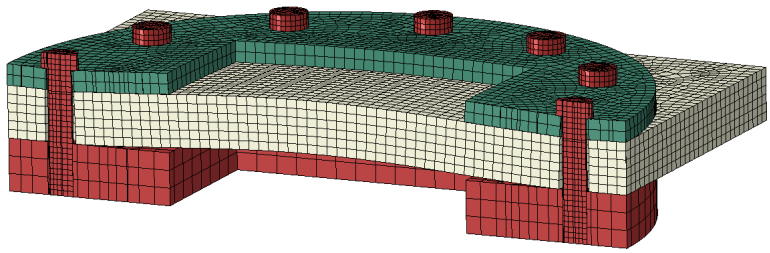

Figure 7.5: *Deformed view of the plate clamping assembly, with deformation amplified by a factor of 50. It can be seen that the clamping plate is not stiff enough to keep the concrete plate fully clamped.*

Figure 7.5 shows the deformation of the plate, amplified by a factor of 50. It is clearly seen that the 20 mm thick aluminium clamping plate is insufficiently stiff to keep the concrete plate fully clamped. Furthermore, from Figure 7.6 it is seen that

Part	*Elements over thickness*	*Element type*
Clamping plate	2	Quadratic brick
Concrete plate	6	Linear brick
Shock tube flange	3	Linear brick
Bolts	5*	Linear brick

*Approximate global element size in mm.

Table 7.3: *Element size and types used for the boundary condition study.*

the maximum principal stress at the front of the plate is concentrated around the bolt holes, not around the edges as predicted by the clamped plate solution. Figure 7.7 shows the displacement profile of the concrete plate taken at the midplane, as well as the maximum principal stress at the back of the plate. The analytical profiles are also shown in this figure, and it can be seen that the clamped plate solution correlates less with the FEA results than the simply supported (pinned) solution. For easier comparison, the FEA displacement profile has been shifted so that the displacement at $x = 0$ is zero. A displacement of 0.1 mm is seen at the boundaries, indicating that the clamping plate deforms during loading. It can be seen that the displacement obtained from FEA is higher than both the analytical solutions. A possible explanation for this is that the analytical solutions do not take shear deformation into account, while the FEA solution does. It is also seen that the stress is not accurately captured by any of the two analytical solutions, as there is considerable tensile stress at the boundary of the plate in the FEA simulation. These findings indicate that the boundary conditions of the concrete plate is not captured accurately by any of the simplified boundary conditions studied so far, and therefore further analysis of the concrete plates should be performed by including the whole clamping assembly.

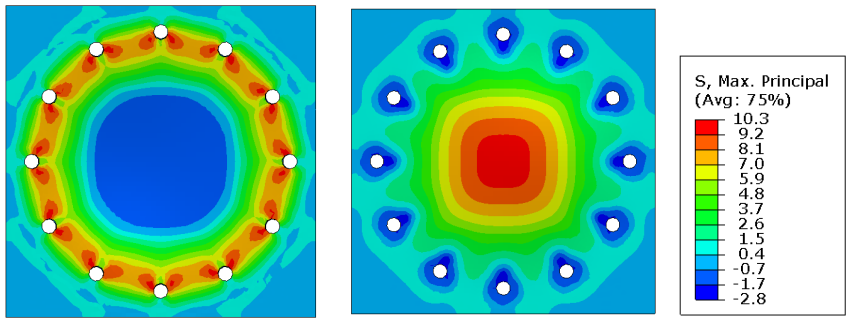

Figure 7.6: *Maximum principal stress at the a) front and b) back of the concrete plate.*

The simulations in Abaqus can also be used to estimate the cracking pressure of the unreinforced concrete plates. Since the deformations are very small, the geometric and contact nonlinearities can be assumed to be small also, and the results can be considered to be linear. In Figure 7.6 it is seen that a static pressure of 10 bar

causes a maximum principal stress of 10.3 MPa in the concrete. Thus, a static pressure of 6.5 bar should give a maximum principal stress of 6.74 bar, which is the bending tensile strength of the concrete. Hence, no cracks should develop at pressures below 6.5 bar. This is close to the analytical estimate from the simply supported unreinforced plate of 7.06 bar.

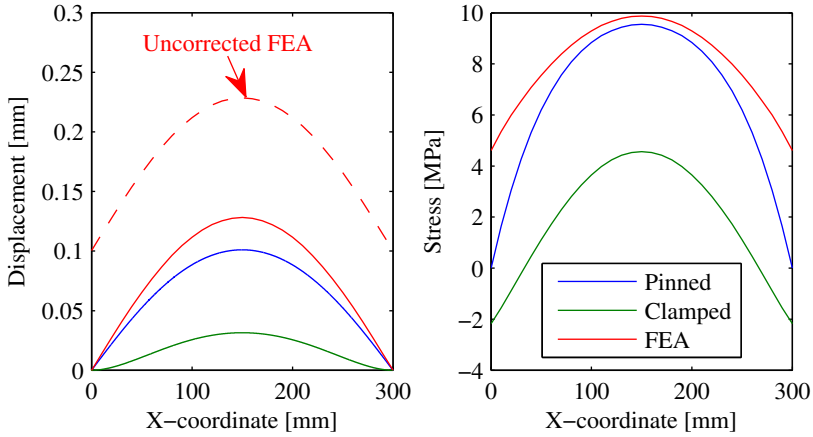

Figure 7.7: *Analytical and numerical displacement profile (left) and maximum principal stress at the back of the concrete plate (right), taken across the middle of the plate. The displacement profile obtained from FEA has been shifted such that the displacement is zero at $x = 0$ for easier comparison with the analytical results.*

7.3 Simulations of material tests in Abaqus

The primary objective of the preliminary numerical analyses in Abaqus was to gain an understanding of how the Concrete Damaged Plasticity (CDP) model responds to various loading types. A natural starting point was therefore to simulate the material tests conducted in this thesis, i.e. the cube/cylinder compression, tensile splitting and three-point bending tests. The motivation behind this is twofold: If the material model fails to simulate the most basic problems, it will probably also fail to capture the response as problems become more complex. In addition, material test simulations are of convenience when calibrating the model, as they are readily compared with experimental results.

In order to employ the CDP model, one must first determine the required material input parameters. Since extensive experimental testing is required to establish these parameters, they were taken from the literature [60]. The entire material data used in the initial simulations can be found in Appendix B.1, while a small summary of the most important parameters is given in Table 7.4. Note that the stiffness E_c proposed in [60] is lower than what was estimated in Chapter 5 (34 GPa). Information regarding the geometrical models is presented in Table 7.5.

E_c [GPa]	υ	f_c [MPa]	f_t [MPa]
19.7	0.19	50	2.8

Table 7.4: *Essential material parameters [60], where E_c is the stiffness, f_c and f_t are the compressive and tensile strengths, respectively, and υ is the Poisson's ratio.*

Model	*el. type*	*el. size* [mm]	*# of elements*	*Dimensions* [mm]
Cube comp.	C3D4*	8	13612	100×100×100
Cylinder comp.	C3D4*	8	23238	Ø100×200
Tensile splitting	C3D4*	N/A	75416	Ø100×200
3pt-bending	C3D8R**	10	6000	100×100×600

*4-node linear tetrahedron.
**8-node linear brick element with reduced integration

Table 7.5: *Information regarding the Abaqus models.*

Initially, the simple C3D4 tetrahedral element was employed for meshing. Although it exhibits locking, and is thus far too stiff, reasonable results may be obtained with an adequately fine mesh [20]. However, it was decided to replace it with the C3D8R brick element in the three-point bending simulations, since this can represent a linear stress field (as opposed to a constant stress field for the C3D4 element), and is thus better suited in bending dominated problems. The simulations in which the C3D4 element was employed were also checked with the C3D8R element, and it was confirmed that they produced virtually identical results for the given meshes.

Dynamic explicit analysis was used in all of the simulations, and it was verified that the kinetic and hourglass energies were negligible compared with the total internal energy to make sure no unwanted dynamic effects affected the solutions. Furthermore, the compression tests and the three-point bending tests were simulated using surface contact, with analytical load plates and a frictional coefficient of 0.2. The value of the frictional coefficient was based on a qualitative estimate, and since it gave reasonable results no further effort was put into finding a more exact value. Surface contact was also used in the tensile splitting simulations, but solid, linear elastic load plates were used instead of analytical plates to better replicate the experimental setup.

7.3.1 Compression test simulations

Stress-displacement curves from the cube and cylinder compression test simulations are shown in Figures 7.8a and 7.8b, respectively. In addition to studying the compressive behavior of the model, the effect of scaling the compressive strength input parameters was investigated. Scaling is done using a scaling factor (sf), which is multiplied with the tabulated compressive stress and strain input values in the model. This approach makes for a convenient way to calibrate the compressive strength to the experimental values.

As can be seen from the figures, the shapes of the stress-displacement curves agree

quite well with the expected response as presented in Section 4.2. A very subtle nonlinear behavior close to the compressive strength can be observed in both figures, and clearly the model captures the post-yield softening in the concrete. The increased cube strength due to the higher confinement pressure is also captured by the model.

Evidently, scaling seems to work well within the tested range. By comparing the stress-displacement curves with the compressive strengths observed in the experiments (the red, dashed lines), it seems that the strength is slightly overestimated by default (sf=1). This will be discussed further in Section 7.3.3. Detailed values from the analysis are presented in Table 7.6.

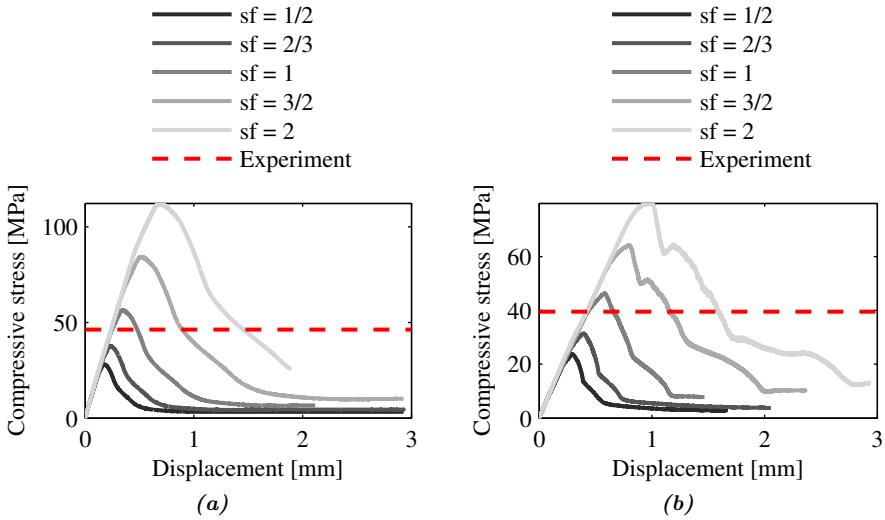

Figure 7.8: *Cube compression (a) and cylinder compression (b). By using a scaling factor (sf) on the material constants from [60], it is possible to change the concrete's compressive strength. sf = 1 corresponds to the default compressive strength, i.e. the tabulated values in Table B.2, Appendix B.1.*

Scaling factor	1/2	2/3	1	3/2	2
f_c, *expected (cylinder)* [MPa]	25	33.3	50	75	100
f_c [MPa], cube	28.3	37.7	56.3	84.3	112.3
f_c [MPa], cylinder	23.8	31.5	46.3	64.3	80

Table 7.6: *Results from the compression test simulations. The compression strength, $f_c = F_{max}/A$, is less for the cylinder, which agrees well with observations from experiments.*

7.3.2 Tensile splitting and three-point bending simulations

Figure 7.9a shows the resulting stress-displacement curves from the three-point bending simulations, while Figure 7.9b shows the stress-time curves from the tensile splitting simulation. The stress was plotted against time since it was difficult to accurately measure the displacement in the tensile splitting simulation. Evidently, the tensile response in both tests is linear all the way until brittle failure occurs. Some crack growth takes place in the tensile splitting cylinder specimen before failure, as can be seen in Figure 7.11a, while a somewhat more sudden failure is observed in the three-point bending test in Figure 7.10. Moreover, comparison between the tensile splitting simulation and the experimental result in Figure 7.11c shows that the CDP model captures the physical behavior quite well. The same can be said for the three-point bending simulation.

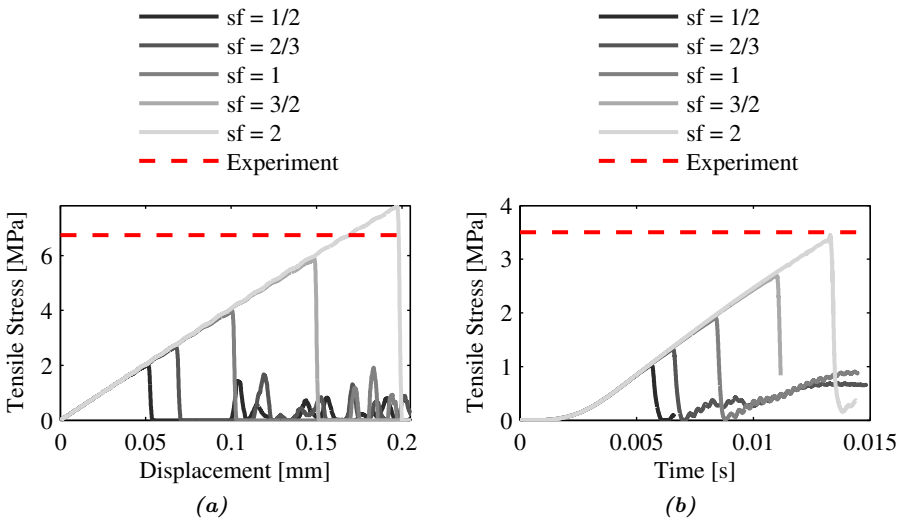

Figure 7.9: *Stress-displacement curves from the three-point bending simulations in (a), and stress-time curves from the tensile splitting simulations in (b). Like with the compression test simulations, a scaling factor has been used to study the effect of changing the tensile strength. The stress-time curve in (b) displays an initial non-linear behavior due to the ramped velocity step used in the analysis. It would be perfectly linear if it were to be plotted against the displacement.*

Using the very same approach as previously, the effect of scaling the tensile strength input data set (see Table B.3 in Appendix B.1) was studied. As Figure 7.9 clearly shows, the default tensile strength (sf=1) is far too low to capture the capacity observed in the experiments in either of the simulations. Fortunately, since scaling seems to work well in the tested range, the tensile strength can be safely calibrated to match the experimental value. It seems from Figure 7.9b that twice the input strength is needed to match the experimentally observed tensile strength of 3.5 MPa, while it is a bit lower for the three-point bending simulation. At this point,

an interesting observation should be made: The CDP model is able to capture that the concrete is stronger in three-point bending than in tensile splitting.

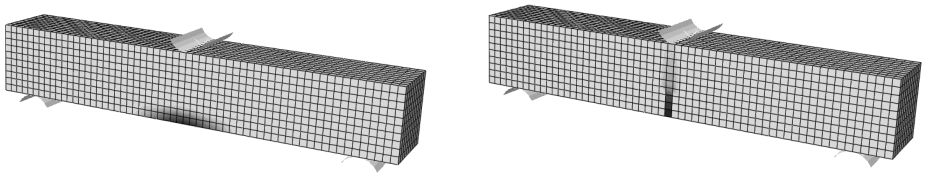

(a) *(b)*

Figure 7.10: *Plastic strain field (a) right before failure and (b) right after failure for the 3-pt bending simulations. Darker elements indicate higher levels of plastic strain.*

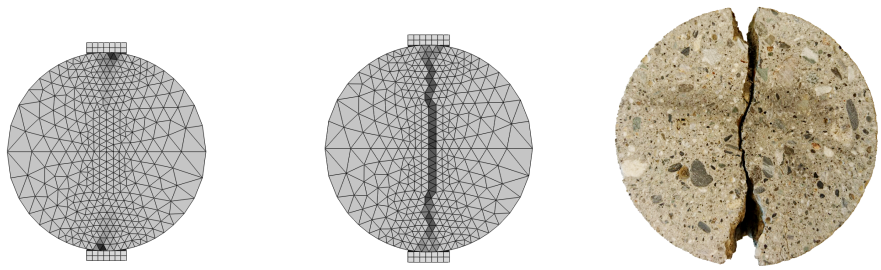

(a) *(b)* *(c)*

Figure 7.11: *The figure visualizes the plastic strain in a cylinder specimen subjected to tensile splitting in Abaqus. An initial crack appears in (a), which with further growth propagates suddenly through the entire specimen (b). A comparison is made with one of the tested tensile splitting specimens in (c).*

Scaling factor	1/2	2/3	1	3/2	2
f_t, *expected* [MPa]	1.4	1.9	2.8	4.3	5.7
f_t [MPa], tensile splitting	1.0	1.3	1.9	2.7	3.4
f_t [MPa], three-point bending	2.0	2.7	4.0	5.9	7.8

Table 7.7: *Results from the tensile splitting and three-point bending test simulations.*

7.3.3 More on strength scaling

To better illustrate and study how scaling the tensile and compressive strength input data set affects the performance of the CDP model, a graphical representation of the results obtained in the two previous subsections is presented in Figure 7.12 below. Not only does it make for an easy way to compare the simulation results, the figure clarifies the behavior of the model when scaling is employed. The appropriate

scaling factors for the compressive and tensile strengths are indicated by the black lines. In compression, the scaling factor was chosen so that it accurately captures the cylinder compression strength after 49-50 days (to match the strength at the day of shock tube experiments). In section 5.4 it was found that the compression strength after 49 days was approximately 5% higher than the 28-days strength, thus the model should capture a cylinder compression strength of roughly 42 MPa. This corresponds to a scaling factor approximately of 0.9. Furthermore, the tensile splitting test was chosen as a reference for the tensile strength, and according to the experiments, a tensile strength of 3.5 should be captured by the model. This corresponds to a scaling factor of 2 in tension.

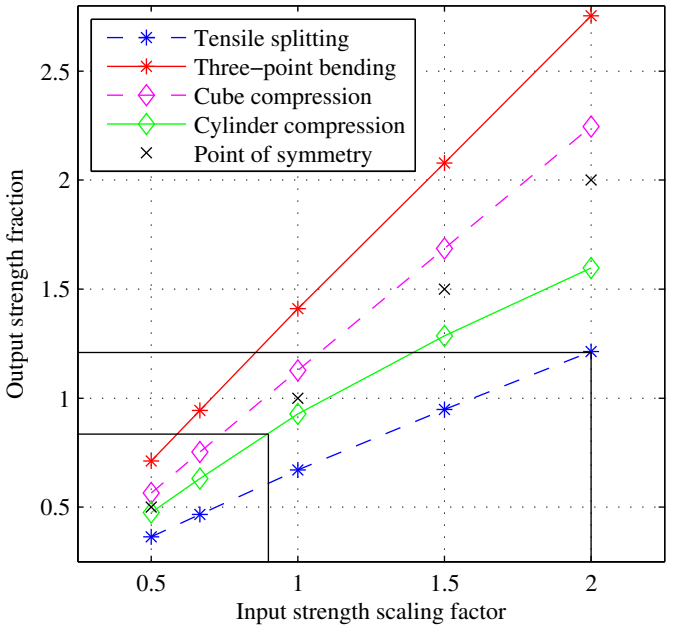

;

Figure 7.12: *The input scaling vs. output strength capacity is plotted for each of the preceding simulations. This is just a graphical way to represent the data already presented in Tables 7.6 and 7.7.*

It is important to realize that this use of scaling is complete equivalent to what happens automatically in the LS-DYNA K&C concrete model with auto-generation of parameters. When the user changes the compressive strength input parameter, a scaling factor is employed in the K&C model to adjust the remaining 48 parameters. This is not possible in Abaqus' CDP model, hence the manual use of scaling.

7.4 Simulations of material tests in LS-DYNA

Preliminary analyses were also conducted in LS-DYNA to investigate whether the K&C-model would capture the behavior that was observed in the cube- and cylinder compression, tensile splitting and three-point bending tests. The material properties used in the simulations are shown in Table 7.8, and the element types and sizes used are summarized in Table 7.9.

E_c [GPa]	υ	f_c [MPa]	f_t [MPa]
29.94*	0.2	40	3.5

*Automatically generated in the K&C-model.

Table 7.8: *Material properties used in the K&C-model.*

Model	*el. type*	*el. size* [mm]	*# of elements*	*Dimensions* [mm]
Cube comp.	C3D8R*	10	1000	100×100×100
Cylinder comp.	C3D8R*	≈ 10	1740	Ø100×200
Tensile splitting	C3D8R*	N/A	6125	Ø100×200
Bending	C3D8R*	10	6000	100×100×600

*8-node linear brick element with reduced integration

Table 7.9: *Information regarding the LS-DYNA models.*

7.4.1 Compression tests

A large uncertainty when simulating the cube compression tests is the friction between the concrete and load plates. Initial simulations showed that the coefficient of friction had a large impact on the simulated cube strength. Figure 7.13 shows the force-displacement curves obtained from simulations with different coefficients of friction. By interpolating the results, it was found that a friction coefficient of 0.068 gave the desired relation between cylinder strength and cube strength, and this value was therefore used for all subsequent compression simulations in LS-DYNA. Since this number most likely is much less than the actual coefficient of friction, it indicates that the K&C model with automatic parameter generation may be overly sensitive to the confinement provided by friction between the load plates. 10 mm reduced integration linear brick elements were used in these simulations, and it was verified that the kinetic and hourglass energies were negligible compared with the total internal energy.

Figure 7.14 shows the average stress versus the displacement for the cube and cylinder. Since the coefficient of friction has been calibrated such that the cube compression strength matches the experimental values, the simulated cube compression strength matches perfectly. The simulated cylinder strength is seen to be slightly higher than the experimental values. This may be due to the mesh, since meshing a cylinder with brick elements leads to a non-uniform element sizes and shapes.

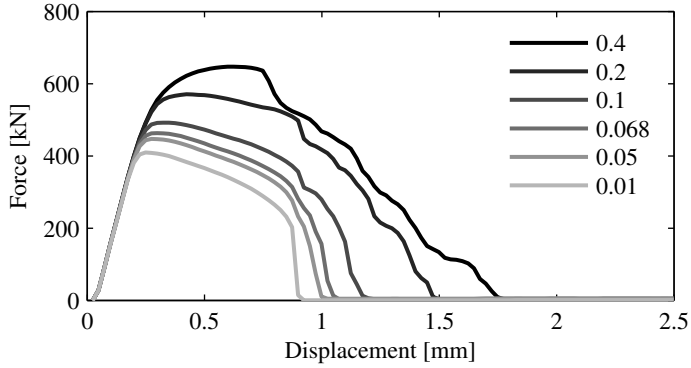

Figure 7.13: *Effect of changing the friction coefficient in cube compression simulation in LS-DYNA with the K&C-model. A friction coefficient of 0.068 is found to give the best correlation to the experimental results.*

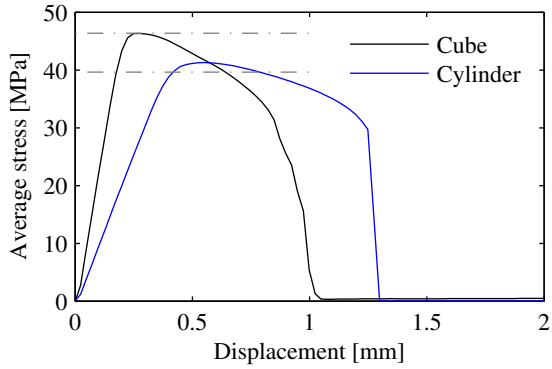

Figure 7.14: *Average stress vs. displacement for cube and cylinder compression simulations in LS-DYNA. The dashed lines indicate the average cube and cylinder compression strengths obtained from physical testing.*

7.4.2 Tensile splitting and three-point bending simulations

Tensile splitting simulations were performed in LS-DYNA to assess how well the K&C-model was able to capture the tensile behavior of concrete. The simulations were performed with three different meshes to study the effect of mesh dependence, and it was found that the K&C-model was not able to capture the correct tensile splitting force and fracture patterns that was observed experimentally, and that the results varied greatly for the different meshes. Figure 7.15 shows the effective plastic strain of the three simulations right after failure, as well as the corresponding stress-displacement curves. It is clear from the curves that only the coarse mesh is able to represent the experimental test reasonably, while the two finer meshes are neither able to capture the fracture pattern nor the strength observed experimentally. One

possible source of error is that these simulations were performed with hard contact between the load plates and the concrete cylinder, without the wood strips used in the experiments. However, this does not explain the very large difference in behavior observed between the different meshes.

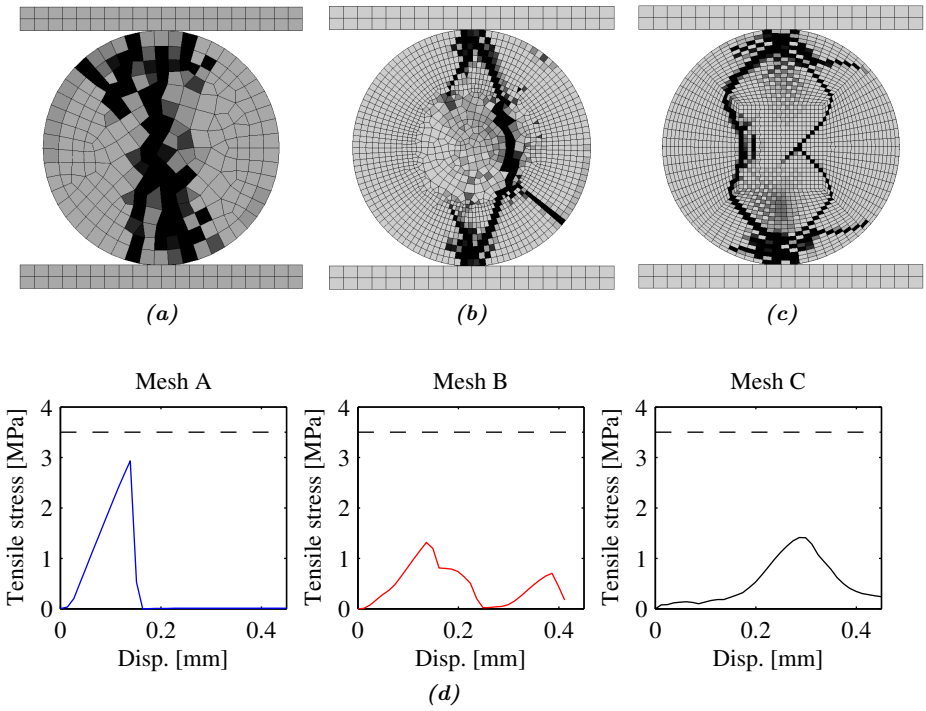

Figure 7.15: *Effective plastic strain at failure for the tensile splitting simulations. Black indicates complete failure of the element. The simulations have been run with (a) 50 elements, (b) 118 and (c) 80 elements around the circumference of the cylinder. Figure (d) shows the stress-displacement curves, where the stress is given by Equation* (5.3)*. The dashed line shows the average tensile splitting strength obtained from the physical tests.*

In order to find the correct input tensile strength for the simulations, it was decided to inverse-model the tensile splitting tests. The mesh in Figure 7.15a was used, since this was the only mesh that produced reasonable results. It was found that in order to get a tensile splitting strength of 3.5 MPa, the input tensile strength needed to be 4.4 MPa. The results are summarized in Table 7.10.

f_t, *input*[MPa]	3.5	4.1	4.41
f_t, *output* [MPa]	2.93	3.23	3.51

Table 7.10: *Inverse modeling of the tensile splitting tests. The input strength is the tensile strength given as input to the K&C-model, while the tensile splitting strength is the tensile strength calculated according to Equation 5.3.*

The 3-pt bending tests were also simulated in LS-DYNA. The concrete beam was meshed with 10 mm elements, and the whole beam was modeled. The supports and load applicator were modeled as completely rigid, and the load applicator was assigned a vertical downward velocity of 2.5 mm/s. The plastic strain field right before and after failure is shown in Figure 7.16. It is seen that the concrete starts to yield in tension before it cracks along the center. As seen in the stress-displacement plot in Figure 7.17, the yielding is insignificant to the overall behavior of the beam, and brittle failure is thus the dominant failure mode. As expected, the stiffness of the concrete is much higher in the simulations than in the experiments, but this is probably because there was compliance in the test machine that was not addressed by the DIC-measurements.

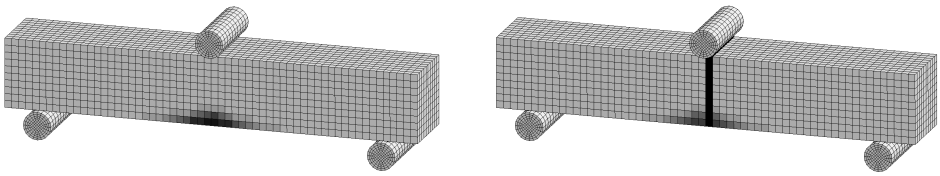

Figure 7.16: *Plastic strain field (a) right before failure and (b) right after failure in the 3-pt bending simulation in LS-DYNA. Darker elements indicate higher levels of plastic strain.*

Inverse-modeling was also performed on the 3-pt bending tests to determine the correct tensile strength to use in further simulations. It is interesting to observe that the K&C-model is able to capture that concrete is stronger in 3-pt bending than in tensile splitting, and it is seen that a tensile strength input of 3.5 MPa gives a bending tensile strength of 5.2 MPa. When an input strength of 4.41 MPa is used, which gave the correct value for the tensile splitting tests, the bending strength is found to be 6.33 MPa. This is very close to the average bending strength found in the experiments, but an input strength of 4.80 MPa is needed to hit the average bending strength spot on.

7.5 Stochastic analysis - Random element strength

Due to its highly inhomogeneous composition, there is a certain randomness to the strength of concrete. In section 5.4.1, it was found that the strength of 20 cubes tested after 28 days of curing varied as much as 3.5 MPa. In the tensile splitting tests the relative variation was even greater, but the number of conducted tests are insufficient to form a reliable statistical basis.

It is believed that the statistical distribution of strong and weak regions inside the concrete is of significance when modeling concrete subjected to blast loads. Many authors have studied the strength of concrete by mesoscale modeling with random

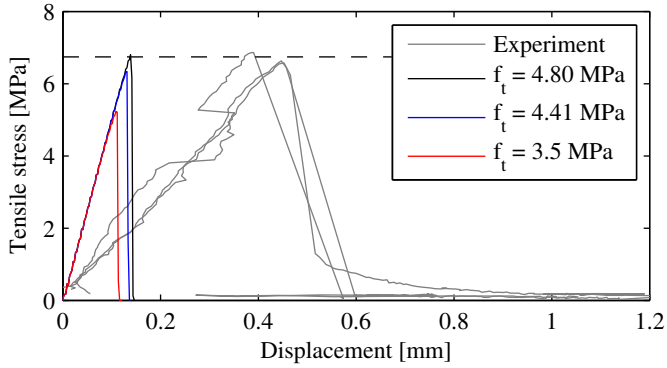

Figure 7.17: *Stress-displacement curves from the bending simulations in LS-DYNA.*

generation of aggregates [61–64], and found that the strength is highly dependent on the meso-scale structure of the concrete. It has mainly been focused on the tensile behavior of concrete in these studies, and the aggregates have been modeled either by 2D- or 3D finite element meshes, or as a simplified lattice structure. Syroka-Korol et al. [65] studied the effect of local fluctuating tensile strength on beam flexural strength by imposing a statistical tensile strength distribution onto a regular tetragonal 2D finite element mesh, and found that this method was able to recreate the statistical size effect that is observed in concrete structures. Brannon et al. [66] remarked that symmetric meshes often lead to unrealistic symmetric cracking in strain softening material models, and that incorporating a statistical distribution of element strength reduces this issue. Moreover, by changing the mean strength of elements with respect to the elements size, according to Weibull's weakest link theory, they observed that the solution became less mesh sensitive.

It has thus been attempted to recreate the statistical variation observed in the physical tests in the finite element simulations by incorporating a statistical distribution of strength in the simulations. This has been implemented simplistically by modifying the input files from Abaqus and LS-DYNA and assigning the elements strength according to a normal distribution of a given mean and standard deviation. Figure 7.18 shows the resulting distribution of strength for a cube with 1000 elements. In LS-DYNA, only the unconfined compression strength has been varied, and the automatic parameter generation capability has generated the rest of the input accordingly. In Abaqus the strength of the elements have been changed by scaling the parameters found in the literature, as described in Section 7.3. The input files have been modified using MATLAB. The desired average strength μ_i and standard deviation σ_i of the elements are given by the user, and the MATLAB-script then automatically generates a given number of materials with strengths linearly varying from $\mu_i - 3\sigma_i$ to $\mu_i + 3\sigma_i$. These materials are then randomly assigned to each element according to a normal distribution. The MATLAB-script used to modify the Abaqus input file is presented in Appendix C.2.

7.5.1 Stochastic cube compression

Multiple sets, each consisting of 20 cube compression simulations, were run in both Abaqus and LS-DYNA. The ultimate goal was to accurately capture the mean stress and standard deviation that had been observed in the experimental compression tests. In this regard, there were two main uncertainties: What the correct statistical distribution of element strength was, and how the cube strength distribution changed when the element size was changed. Since concrete is highly heterogeneous, an "element" may have anything from zero (voids) to several hundred MPa (quartzite aggregate etc.) in compression strength. This vast difference in element strength should be mirrored by the statistical model. Furthermore, it was suspected that the effect of element strength variation would diminish with decreasing element size, so it was important to determine how severe this behavior would be. Since the aggregates can, to some extent, be assumed to be homogeneous, it can also be argued that the element size should be close to that of the aggregates. Figure 7.18b illustrates a cube with element-by-element strength variation, while the corresponding element strength distribution is shown in Figure 7.18a. Each simulation will necessarily have its own unique spatial distribution of element strength.

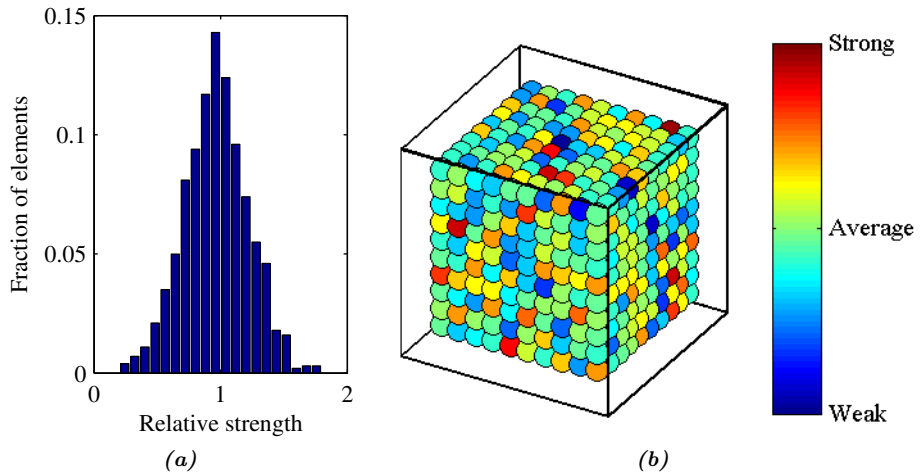

Figure 7.18: *(a) Statistical distribution of strength of the elements in a cube of 1000 elements, and (b) the corresponding spatial distribution of strength.*

First, an attempt was made to achieve the best possible fit to the experimental curve using Abaqus and LS-DYNA. To achieve this, both the element mean strength and the standard deviation in element strength were adjusted for each set until a reasonable fit was achieved. Moreover, the mesh was kept constant at 1000 elements in all of the simulations in order to avoid any possible mesh sensitivity effects. The results from the analysis are illustrated in Figure 7.19, while a detailed overview

can be found in the following Tables 7.11a and 7.11b.

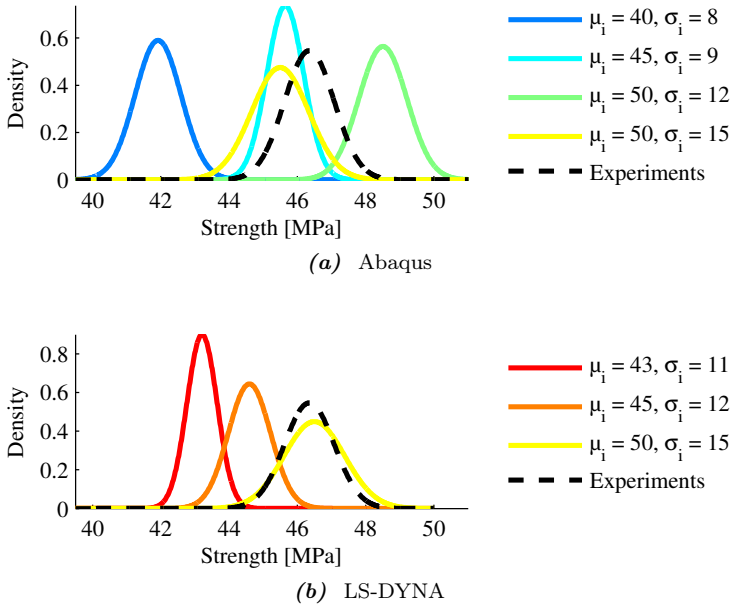

Figure 7.19: *Normal distribution curves from the attempted calibration of the statistical model in Abaqus (a) and LS-DYNA (b).*

Some very clear trends can be observed in Figure 7.19. Obviously, there is a strong relation between element mean strength and cube mean strength. Moreover, comparison between the blue and teal curves indicates that an increase in mean strength also seems to reduce the standard deviation. Furthermore, it seems that an increase in the element strength variation reduces the cube mean strength. This could indicate that the weakest elements are far more predominant than the strongest elements in their effect on the overall strength. This result is in agreement with the work done by E. Syroka-Korol et al. [65], where they found that a higher material (element) coefficient of variation yields a lower mean nominal strength in addition to a higher coefficient of variation of the overall strength. Similar conclusions were made by Grassl et al. [67], who found that the far-left tail of the cumulative distribution function of strength dominates the structural response.

The yellow curves in Figure 7.19 represent the best fits acquired in Abaqus and LS-DYNA.

The next objective was to study the mesh sensitivity of the stochastic method. Multiple sets with different meshes were run in LS-DYNA and Abaqus, and all sets in each program were run with the same element mean strength and standard deviation, as described in Table 7.12. From the results presented in Figure 7.20, it is perfectly clear that the proposed method is indeed very mesh sensitive when the

	Element		*Cube*	
Set	μ_i	σ_i	μ_f	σ_f
Blue	40	8	41.92	0.68
Teal	45	9	45.65	0.54
Green	50	12	48.50	0.71
Yellow	50	15	45.50	0.84
Experiments	-	-	46.35	0.73

(a) Abaqus

	Element		*Cube*	
Set	μ_i	σ_i	μ_f	σ_f
Red	43.19	11	43.21	0.44
Orange	45	12	44.60	0.62
Yellow	50	15	46.50	0.89
Experiments	-	-	46.35	0.73

(b) LS-DYNA

Table 7.11: *Detailed results from the attempted calibration of the statistical model in Abaqus (a) and LS-DYNA (b). μ_i and σ_i are the element mean stress and standard variation respectively, while μ_f and σ_f are the resulting mean and standard deviation in cube strength.*

element strength distribution is kept constant. Most prominent is the connection between element size and standard deviation. That is, finer meshes lead to less variation in the cube's compression strength. Notice the difference between the blue and orange curves. Another factor affected by element size is the mean strength. However, the relationship between mesh size and mean strength is not as consistent as the mesh size vs. standard deviation relationship, in either program, thus further studies are necessary to make valid conclusions in this matter. In conclusion, it seems that the stochastic method herein must be calibrated for each mesh size, and that a wider element strength distribution is needed for fine meshes.

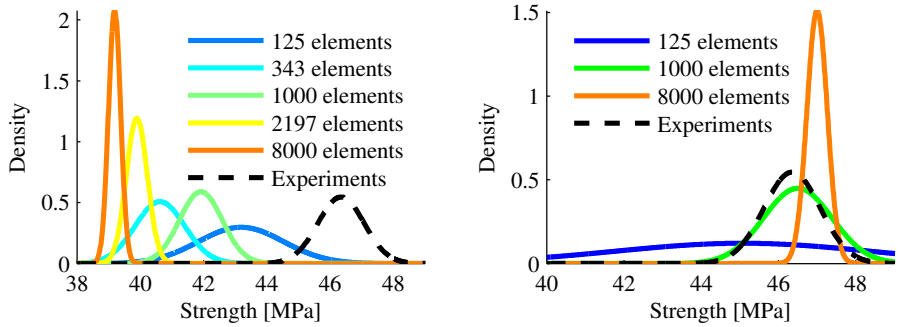

(a) Abaqus ***(b)*** LS-DYNA

Figure 7.20: *The figure shows normal distributions fitted to the results from the mesh sensitivity study in Abaqus (a) and LS-DYNA (b).*

Model	μ_i [MPa]	σ_i [MPa]	*Element*	*Dim.* [mm]
Abaqus	40	8	C3D8R	100×100×100
LS-DYNA	50	15	C3D8R	100×100×100

Table 7.12: *Model information for the mesh sensitivity analysis.*

One should keep in mind that only one set has been run for each configuration,

and that the set-wise variation is therefore not known. Running more sets with the same mesh size and element strength distribution would reveal the discrepancies existing between identical sets, and could possibly be used to explain some of the observed trends, as well as indicating if 20 simulations are sufficient to give a sound statistical basis.

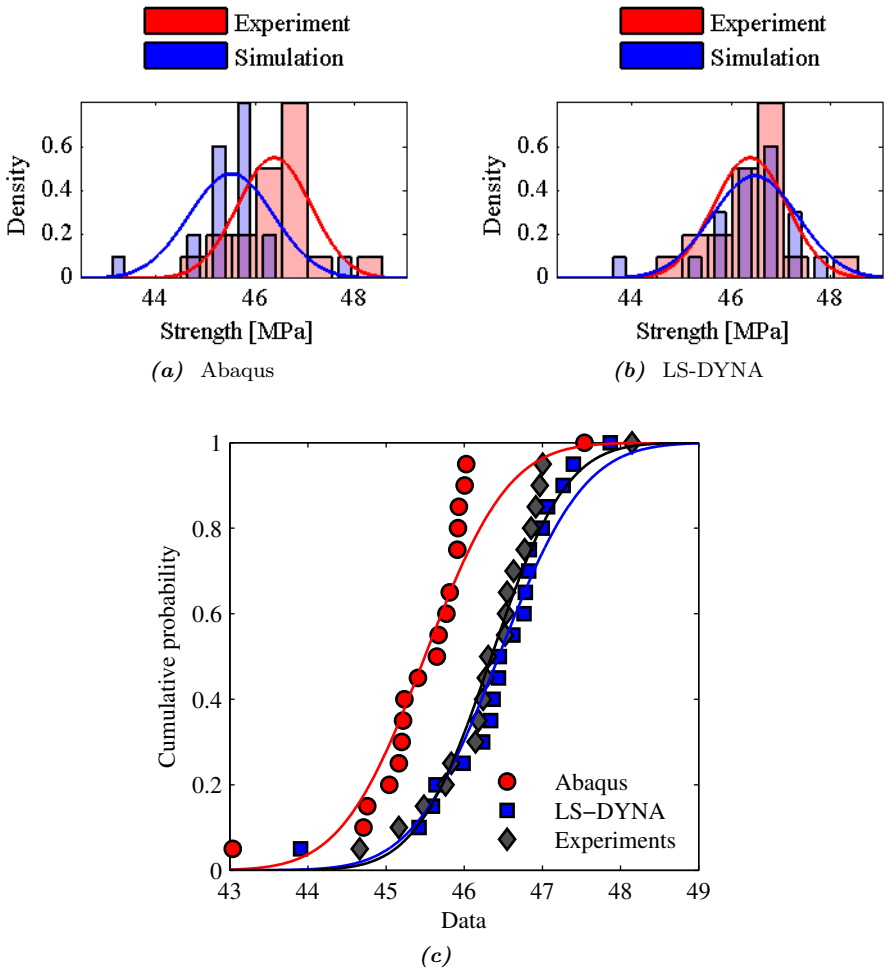

Figure 7.21: *The best fit from the Abaqus study (a) and from the LS-DYNA study (b) is presented in closer detail. The cumulative distributions for both programs, in addition to the experimental results, are given in (c).*

To further compare the performance of the LS-DYNA and Abaqus models, the best fit for each program (the yellow series in Figure 7.19) is investigated with greater detail in Figures 7.21 and 7.22. Figures 7.21a and 7.21b include the data used to fit the normal distributions, thus providing closer insight into the actual behavior of

the statistical method. Figure 7.21c displays the cumulative distribution functions in combination with their respective numerical and experimental results. It is seen that reasonable fits were achieved with both LS-DYNA and Abaqus, however the LS-DYNA fit is far closer than the latter. Perhaps most interesting are the results presented in Figure 7.22. These reveal an important difference in how the two programs respond to the implemented statistical model. Both programs capture roughly the same maximum strength and stiffness, however their post-yield behaviors differ greatly in that introducing statistical variation drastically reduces the ductility in the LS-DYNA K&C model, while little change is observed in the Abaqus CDP model. Moreover, the shape of the curves from the K&C model seem less physically correct than those from the latter, compared with the idealized behavior discussed in Section 4.2.1. This was also observed in the simulations without statistical variation.

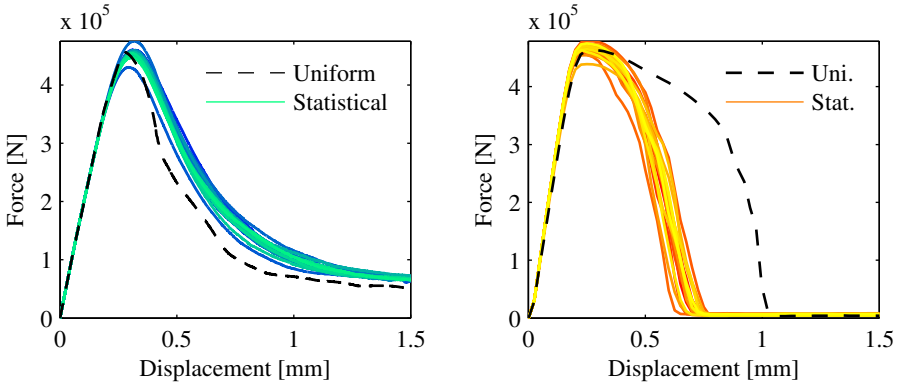

(a) Abaqus *(b)* LS-DYNA

Figure 7.22: *Force-displacement curves from all 20 simulations run in Abaqus (a) and LS-DYNA (b) for the best fitted series. In addition, the force-displacement curve from a uniform simulation, i.e. without statistical variation, is included in each figure.*

7.6 Stochastic analysis - Mesoscale modeling

Due to the mesh-dependent behavior of the stochastic method presented above, a more physically correct method was also attempted by dividing the elements of a mesh into aggregate and cement. This method is essentially mesoscale modeling of the concrete, as performed by numerous authors previously with different degrees of sophistication. Echardt, Häfer and Könke [68], for example, simulated the fracture behavior of concrete at the mesoscale in 2D by generating a distribution of ellipsoids to represent the aggregate, using a sieve-analysis curve to achieve the correct distribution of aggregate sizes. Each aggregate was meshed by tetragonal elements with nodes coincident to the aggregate boundaries, and a smeared-crack material

model was assigned to the cement and aggregate. They also assumed a rigid bond between the cement and aggregate, and concluded that the model produced reasonable crack patterns, with microcracks initiation around the aggregates. Other authors, such as Shuguang and Qingbin [69], included the effect of the transition zone between the cement and aggregate, and modeled each aggregate accurately by performing CT-scans on a concrete specimen.

The method developed in the following is similar to the method used by Echardt et al. [68] in that a rigid bond is assumed between the cement and aggregate. However, instead of meshing the concrete such that the nodes are coincident to the aggregate boundaries, a randomly generated aggregate distribution is superimposed on a regular mesh, and the elements are divided into aggregates or cement. Both aggregates and cement are modeled with the K&C-model, where the aggregates are given a much higher strength than the cement. Due to time constraints, this method has only been implemented to work with LS-DYNA and the K&C material model.

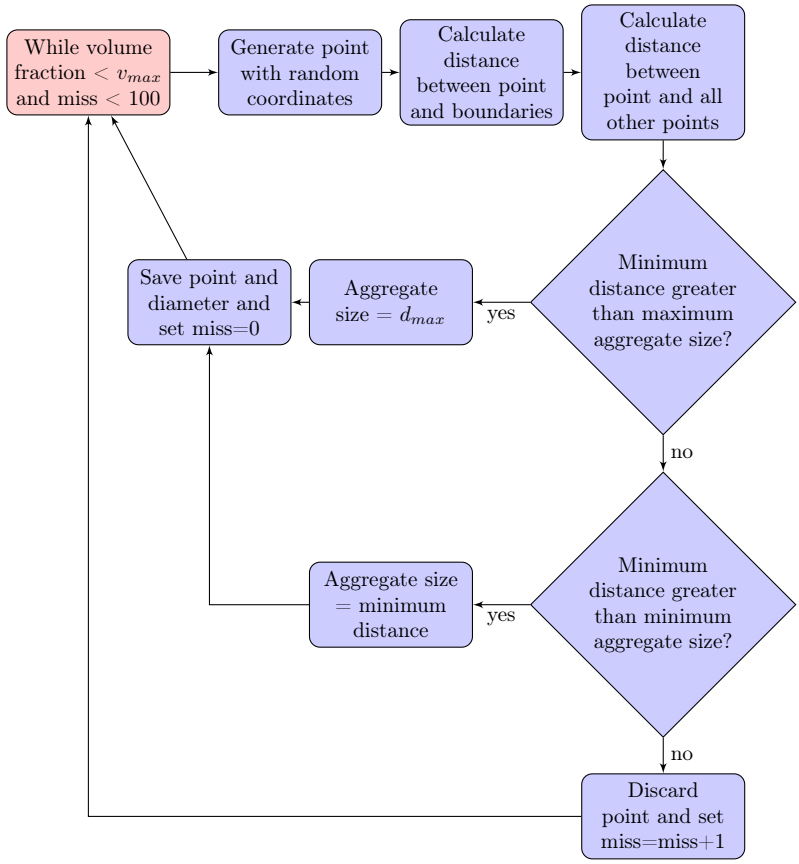

Figure 7.23: *Aggregate generation algorithm.*

MATLAB was used for programming the mesoscale method. The generation of aggregates is achieved by first defining the boundaries of the component, as well as the maximum and minimum size of the aggregates to be generated. The volume of the component will then gradually be filled by spheres that are placed at random positions with the required size to avoid overlapping regions. If a sphere is placed inside or too close to another sphere, the sphere will be deleted and a new attempt at placing a sphere is made. This process will go on until the desired aggregate volume fraction is reached, or until the algorithm fails 100 consecutive times. An overview of the algorithm is given in Figure 7.23. When an aggregate is placed successfully, the center coordinate and radius is saved to a matrix. Next, a finite element mesh is imported and the coordinates of the volume center of each element is calculated. For each aggregate, the algorithm checks whose elements volume centers are inside the sphere, and these elements are assigned the aggregate material. The remaining elements are assigned the cement material.

Figure 7.24 shows the aggregate distribution generated by the algorithm for a concrete mix with $D_{max} = 16$ mm and $D_{min} = 8$ mm, with an aggregate volume fraction of 0.35. This is roughly equivalent to the B20 concrete used in this thesis. The resulting aggregate meshes with three different mesh sizes are also shown. It should be noted that the algorithm does not guarantee that the meshed aggregates are separated. This means that two coincident aggregates may turn into one large aggregate if the component is meshed with a coarse mesh, as is evident in Figure 7.24c. By using a fine mesh, this problem becomes less evident.

7.6.1 Stochastic mesoscale cube compression

20 cube compression test simulations were run with the stochastic mesoscale algorithm and the mesh in Figure 7.24c. An aggregate strength of 200 MPa and a cement strength of 30 MPa was used as an initial guess. The resulting force-displacement curves and the cube strength distribution is shown in Figure 7.25. It is seen that the mesoscale method causes an even more abrupt post yield decline in force than the stochastic method used previously. Still, the initially guessed aggregate and cement strength matches the experimental strength distribution very well, and it is interesting that the stochastic distribution is adequately represented only by changing the mesostructure in the simulations.

Simulations of the mesoscale model with finer meshes were also performed in order to evaluate the qualitative realism of the model. Two models with very fine meshes were run, one with 125 000 elements and one with 512 000 elements, as seen in Figures 7.24d and 7.24e. These meshes correspond to 50 and 80 elements along each edge of the cube, respectively. Different aggregate mesostructures were used for the different mesh sizes. These simulations were also run with element erosion in order to capture the crack pattern observed experimentally. The element erosion criterion was set to delete any elements with a maximum principal strain larger than 0.01, as was also used by [12].

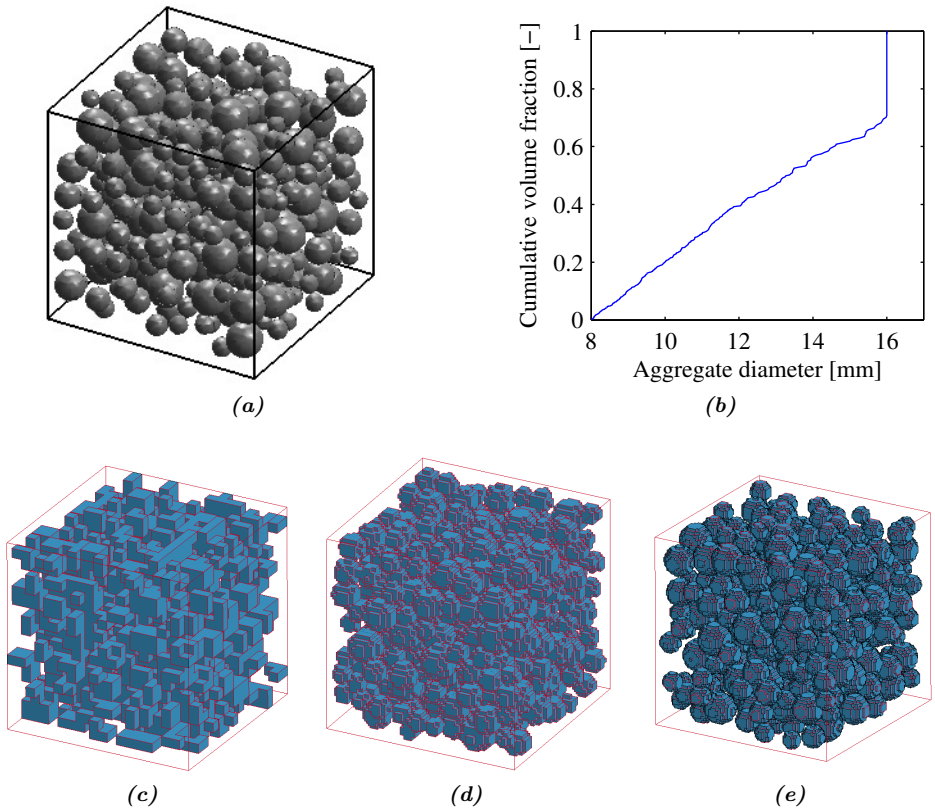

Figure 7.24: *(a) Randomly generated aggregates with $D_{max} = 16$ mm and $D_{min} = 8$ mm and (b) the cumulative volume fraction of the aggregates. The jump at $D = D_{max}$ occurs because the algorithm always generates aggregates with $D = D_{max}$ where they do not overlap other aggregates. Also, the resulting meshes of the aggregates with (c) 8000 elements, (d) 125 000 elements and (e) 512 000 elements are shown.*

Table 7.13 shows the crack pattern evolution for the two meshes with coefficients of friction of 0.068 and 0.2 between the load plates and concrete. It can be observed that both meshes are able to capture the crack patterns that were observed experimentally, but the simulations with low friction develop excessive cracking at the load surfaces. From the load-displacement curves in Figure 7.26, it is seen that the simulations with low friction give too low cube strength, while the high friction simulations give too high strength. Since the aggregate mesostructure differs in the two meshes, the difference in strength may be within the natural variance of the model. From the energy plots it is clear that a substantial amount of energy is eroded once the cube starts to crack, indicating that the simulations may be inaccurate beyond initial cracking.

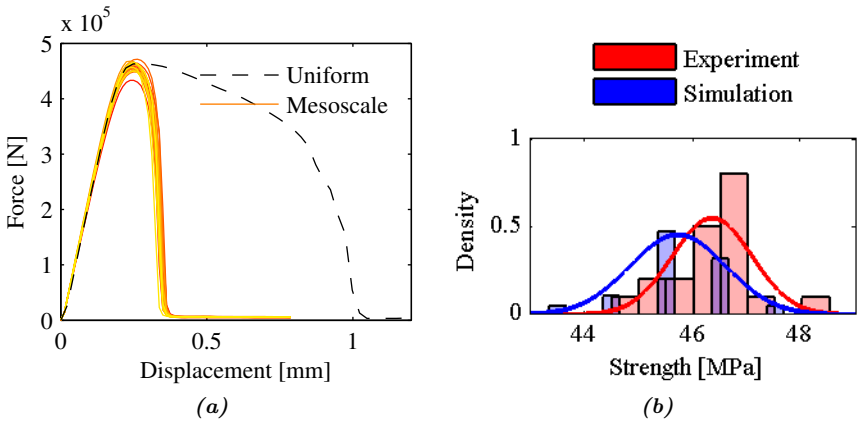

Figure 7.25: *(a) Force-displacement curves from 20 stochastic mesoscale simulations and (b) the resulting cube strength distribution.*

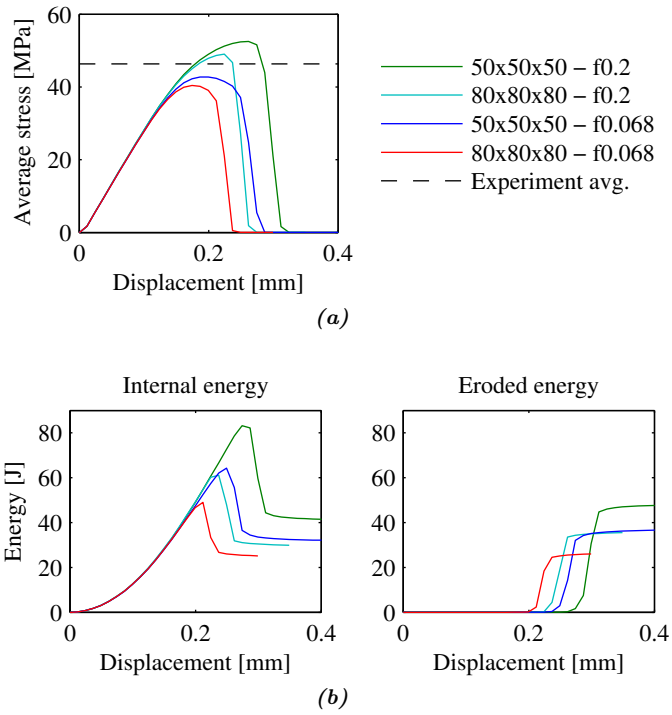

Figure 7.26: *(a) Load-displacement curves for the mesoscale simulations with fine meshes and (b) energy plots from the simulations.*

Elements	*Friction*	*At maximum force*	*During failure*	*Complete failure*
125 000	0.068	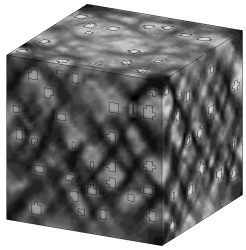	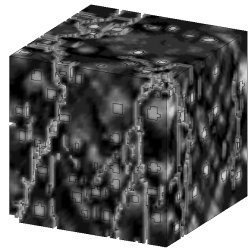	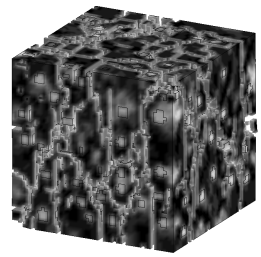
512 000	0.068	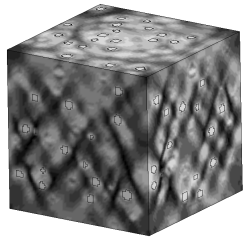	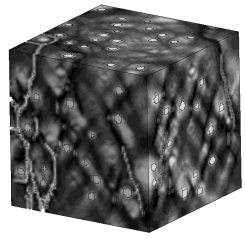	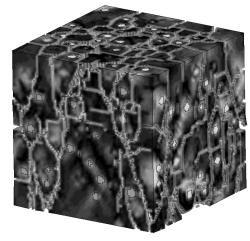
125 000	0.2	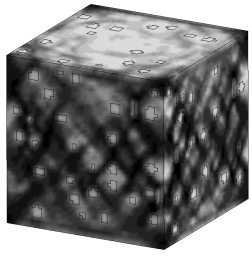	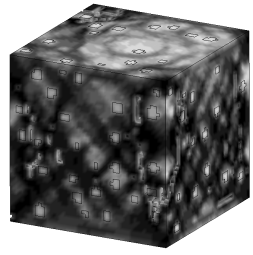	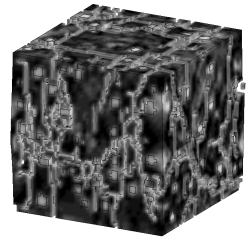
512000	0.2	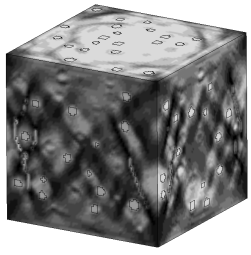	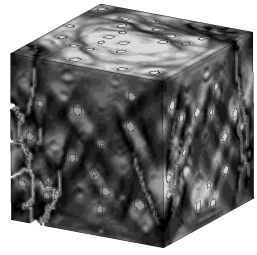	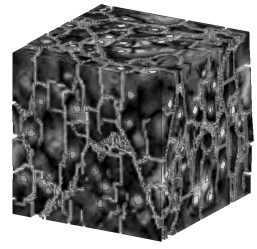

Table 7.13: *Mesoscale simulated crack patterns. Darker shade indicates higher equivalent plastic strain.*

7.7 Summary and discussion

In this chapter, analytical linear-elastic calculations of a plate subjected to uniform pressure have been performed, as well as limit state analysis using the yield line method. The boundary conditions for a shock tube mounted concrete plate have been studied in Abaqus to decide the best method for modeling the problem in subsequent analyses. To assess the performance of the Concrete Damaged Plasticity (CDP) model and K&C model in Abaqus and LS-DYNA, respectively, FE-simulations of concrete material test specimens were conducted. The stochastic nature of concrete was then attempted captured by assigning random element strength in the FE-simulations according to a normal distribution. Finally, a mesoscale model was developed to further investigate the stochastic behavior of concrete.

7.7.1 Concrete plate response

The analytical calculations showed that assuming fully clamped boundary conditions is not correct, since fully clamped boundary conditions should consistently produce more severe cracking at the front surface of the plates than observed in the experiments. Both the fully clamped and simply supported calculations were to some extent able to predict the direction of the cracks at the back surface of the plates, and the calculated cracking pressures also seem reasonable. Furthermore, by transforming the analytical models into equivalent SDOF-models, it was found that the response of the plates to the blast loads generated by the shock tube can likely be characterized as quasi-static. This was also concluded by Haug and Osnes in 2015, but they assumed fully clamped boundary conditions and did not look into the effect of reinforcements. The limit state analysis showed that the plastic capacity in the reinforced plates was substantially lower than the elastic capacity. However, since none of the experimental plates developed the crack patterns proposed in the limit analysis, no further effort was put into this method.

Following the analytical calculations, the whole clamping assembly of the shock tube was modeled in Abaqus. The simulations showed that the stress field could not be reproduced accurately by the idealized boundary conditions in the analytical calculations, and it was thus concluded that further analysis should be performed with the full clamping assembly.

7.7.2 Simulations of concrete test specimens

Abaqus and LS-DYNA were used to simulate the material tests in Section 5.4, using the Concrete Damaged Plasticity and K&C material models, respectively. Considerable effort was made to establish suitable input constants for the CDP-model by scaling the material data set found in the literature. The CDP-model was able to capture that concrete cubes are stronger in compression than concrete

cylinders, and that the tensile strength is greater in 3pt bending than in a tensile splitting test. This effect was also captured by the K&C-model. The K&C-model, however, was seen to be sensitive to the frictional coefficient in the cube compression simulations, and a very low frictional coefficient was needed if the cube compression strength were to be accurately modeled. Also, mesh refinement in the tensile splitting simulations with the K&C-model lead to less accurate results.

Comparing the post-peak compressive strength behavior of the two material models, it is clear that the CDP-model is more in agreement with the idealized curves presented in Section 4.2.1. While the shape of the force-displacement curves can only be assessed qualitatively, the post-peak compressive strength behavior of the K&C-model seems excessively ductile. It should be noted that the behavior of the K&C-model can be tuned by manually adjusting the material constants, but this would remove one of the main benefits of using the K&C-model, namely its simplicity.

7.7.3 Stochastic methods

The stochastic nature of concrete was attempted recreated by two methods, random element strength and mesoscale modeling. In the random element strength method, the elements of a FE-mesh are randomly assigned strength according to a normal distribution. This method was implemented in MATLAB to work with both Abaqus and LS-DYNA, and a large number of cube compression simulations were run to study the effect of element size and element strength distribution. By running multiple series with different element strength distributions, it was found that the relationship between the element strength distribution and cube strength distribution was generally not straightforward. Yet, it was observed that the left tail of the element strength distribution dominated the cube strength distribution. Finally, an element mean strength of 50 MPa with a standard deviation of 15 MPa was found to reproduce the stochastic variation of cube strength seen in the experiments, given an element size of 10 mm. As suspected, it was confirmed that the method was sensitive to element size, with finer meshes resulting in a more narrow distribution of cube strength.

To remedy the mesh dependence of the random element strength method, it was attempted to model the aggregate and cement matrix of the concrete directly. A script was written in MATLAB to place a given volume fraction of spheres inside a concrete part and superimpose this onto a regular FE-mesh, before dividing the mesh into aggregates and cement matrix. Both aggregates and cement were modeled with the K&C-model, using a uniaxial compressive strength of 200 MPa and 30 MPa, respectively. This initial guess of aggregate and cement strength gave a good representation of the stochastic cube strength distribution, and caused a much less ductile response than the simulations with uniform material using the K&C-model. Cube compression tests were also simulated with very fine meshes using the mesoscale method with element erosion, from which it was seen that

the method reproduced the crack patterns seen in the cube compression tests with good accuracy.

Comparing the two stochastic methods used herein, it is clear that both methods have their merits. The main benefit of the random element strength method is that it is relatively easy to implement for any geometry. Still, the lack of objectivity is a serious drawback which requires that the model is tuned for each mesh size. The mesoscale method, on the other hand, does not exhibit the same degree of mesh dependent behavior, and makes sense from a physical standpoint. However, choosing an appropriate material model for the cement and aggregate is not straightforward, and more work should be performed to establish the tensile properties of a concrete specimen modeled with the mesoscale method. Also, an exceedingly fine mesh is needed to accurately model the spherical aggregates. For structures where the aggregate size is small compared with the dimensions of the structure, the mesoscale method is not feasible due to the enormous amount of elements needed. In such cases, the random element strength method may be more suitable since it can be calibrated to any element size.

Chapter 8

Simulations of Concrete Plates in Abaqus

This chapter presents the shock tube simulations performed in Abaqus, all of which were done with explicit analysis using the reference model shown in Figure 8.1. In section 7.2 it was found that the plate boundary conditions are too complicated to be idealized as clamped or simply supported, etc. Therefore, the reference model was made as identical to the real clamping assembly as possible, with contact defined between all parts. A preload force was applied to the bolts during an initial static step. However, due to convergence issues in the preload step, the preload had to be reduced from 31.5 kN, which was used in the boundary condition study in Section 7.2, to 8 kN. The geometry of the rebar mesh was replicated, as seen in Figure 8.1c, and the material was modelled using power law hardening with the material properties calibrated in Section 5.5. The concrete properties were based on the study of strength scaling in section 7.3.3, and are presented briefly in Table 8.1. The default stiffness found in the literature was not changed.

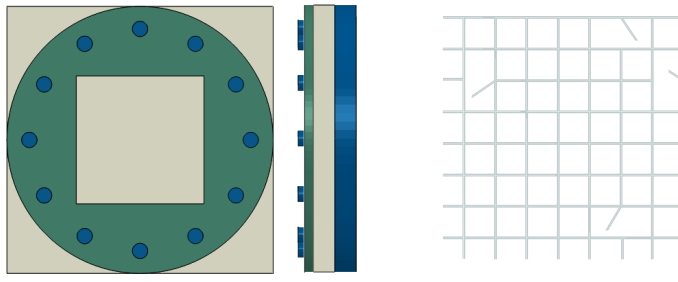

Figure 8.1: *The figure shows the reference model used in the Abaqus simulations, with the back side of the assembly (a), its profile in (b) and the rebar mesh in (c).*

In those simulations where the two rebar meshes are included, they have been connected to the concrete by use of the *Embedded region* constraint in Abaqus. Furthermore, the pressure load in each simulation was defined by importing its respective Friedlander curve, as found in Chapter 6. Table 8.2 presents some more detailed information regarding the reference model.

f_t [MPa]	f_c [MPa]	ν	ρ [kg/m^3]
5.7	45	0.2	2440

Table 8.1: *Input parameters used with the CDP model. The strengths are based on the study of strength scaling in the preliminary analysis. There it was found that an input compressive strength f_c of 45 MPa yields roughly 42 MPa in the cylinder compression simulations, while the 5.7 MPa input tensile strength f_t will produce a strength of 3.5 MPa in the tensile splitting simulations.*

Assembly part	*Material*	*E* [GPa]	ν	*Plasticity*	*Element*
Backing plate	Steel	200	0.33	-	C3D8R
Bolts	Steel	200	0.33	-	C3D8R
Clamping plate	Aluminium	70	0.33	-	C3D8R
Concrete plate	Concrete	20	0.2	CDP	C3D8R
Rebar	Rebar steel	200	0.33	Power law	Truss

Table 8.2: *Reference model material data. The backing plate, the bolts and the clamping plate were all modelled as elastic materials, while power law hardening and the Concrete Damaged Plasticity model were employed for the reinforcement and the concrete plate, respectively.*

The study in Abaqus is divided into three different parts: First, mesh sensitivity is investigated for two different meshes; a coarse mesh and a fine mesh. Then, a subroutine that enables the use of element erosion is created and implemented in the model, and its impact on the simulations is studied. Finally, a study on the effect of using random element strength is conducted.

One way of presenting the simulation results is to visualize the plastic principal strain. In fact, this is the preferred method of tracking crack growth in the CDP model. As the reader will soon discover, the figures visualizing the plastic principal strain presented herein have some additional red lines included. These lines are actually the crack patterns observed in the experiments for the particular plate in question. The commercial software Adobe Photoshop has been used to achieve this layering of experimental results exactly on top of the simulated results. This approach makes for an easy way to directly compare the real and simulated responses. Another way to assess the results is to investigate the midpoint deflection in the concrete plate. This has been done by comparing the DIC-measured deflection with the simulated deflection.

8.1 Effect of mesh

A central aim of the mesh study was to determine how well (or poorly) crack patterns are captured, and to see if there was reasonable agreement between the two meshes in this regard. Moreover, it was important to reveal any mesh dependence present in the CDP model, i.e. to determine if mesh refinement alters the behavior of the plate. In the CDP model, mesh dependence is known to be most predominant in simulations of plain concrete [45].

Two different meshes were employed. The coarse mesh shown in Figures 8.2a and 8.2b consists of 10 mm large elements. This equates to five elements over the plate thickness. Figures 8.2c and 8.2d show the fine mesh, where an element size of 5 mm has been used. With this, twice the number of elements across the thickness is achieved.

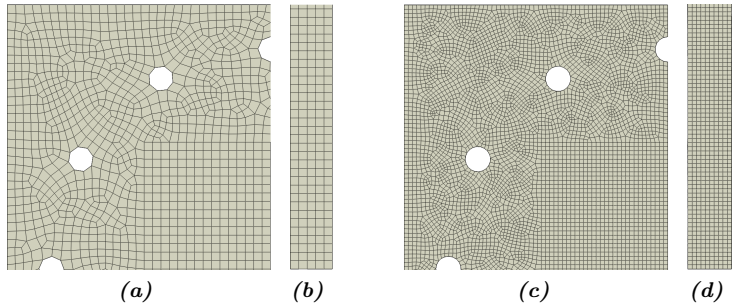

Figure 8.2: *The front and side view of the coarsely meshed concrete plate is shown in (a) and (b), respectively. Likewise for the fine mesh in (c) and (d). The coarse mesh consists of 10 mm elements, while 5 mm elements are employed in the fine mesh*

The simulation results are presented on the next two pages, in which Figure 8.3 displays the midpoint deflection curves and Table 8.3 shows the crack patterns. From Figure 8.3, one can draw some clear conclusions: First of all, the plate simulations are very mesh dependent, but only for the plain concrete. That is, the stiffness of the plain concrete plates is greatly reduced with mesh refinement. Furthermore, it is obvious that the simulations at low pressures yield much more accurate results. In fact, the simulated midpoint deflection of the reinforced plate at low pressure (R-41) in Figure 8.3b is virtually identical to the DIC-measured deflection, for both meshes. While the same cannot be said for the coarsely meshed plain plate at low pressure (P-41), the simulated deflection is still quite close to the measured one. At high pressure, the simulated deflection in the reinforced plate is overestimated by roughly 100% at peak load. Also the post-peak load behavior is different, but this might be a consequence of not including the rigid body motion of the shock tube in the simulations. The deflection of the plain plate at high pressure is also overestimated by roughly 100%, but a drastic change in capacity is observed with the refined mesh: The plate totally collapses.

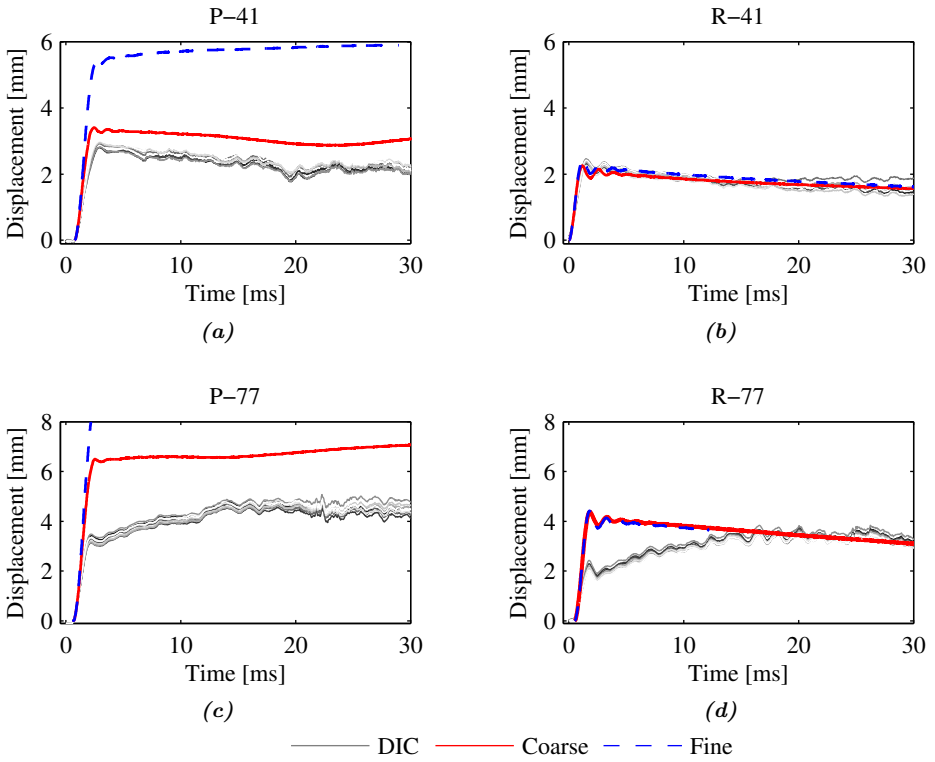

Figure 8.3: *Midpoint deflection plotted against time for the plate simulations in Abaqus. The DIC-measured midpoint deflections are also included in the figures for comparison. Rather than using a single point from the DIC measurements, several points sampled in the center of the plate was used. The figures to the left are from the plain concrete simulations at low (a) and high (c) pressures, while the two on the right are from the reinforced concrete simulations at low (b) and high (d) pressures.*

The crack patterns in Table 8.3 are readily used to further assess the results. While the plain concrete plates exhibit a very star-like crack pattern, the patterns in the reinforced plates are more grid-like and to some extent follow the orientation of the rebar mesh. Both of these results are in agreement with the observed cracks from the experiments. Moreover, crack patterns are captured well in both meshes, however the fine mesh produces a much more prominent and distinguishable pattern in most of the simulations. It is rather remarkable how well the cracks are captured by the model. Even the squares forming in the center of some of the plates are reproduced in the simulations, however it should be noted that the damage seems excessive in most cases, in particular at the front surface of the plates.

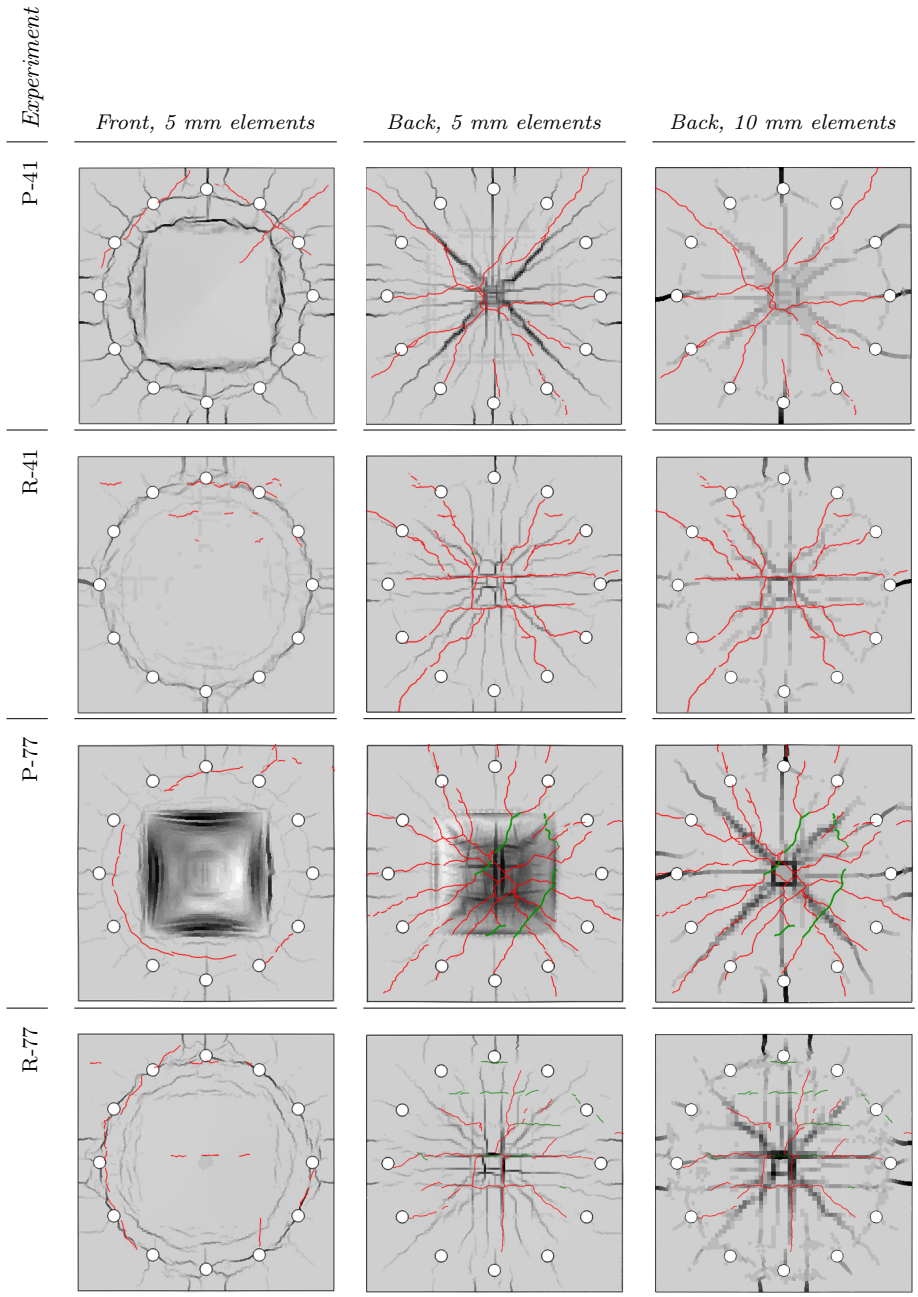

Table 8.3: *Simulated crack patterns in Abaqus. Darker shade indicates higher principal plastic strain, while the red lines represent the experimentally observed cracks.*

8.2 Effect of element erosion

While readily available in LS-DYNA by the **MAT ADD EROSION* keyword, element erosion is not directly available in Abaqus' CDP model. However, it can be implemented manually by writing a user subroutine in Fortran. An interesting objective in this regard is to examine how well user-defined element erosion actually performs, and to assess whether it is a viable option in blast simulations with the CDP model.

A VUSDLFD subroutine was developed by the authors, and is presented in Appendix C.1. A maximum plastic principal strain of 0.01 was chosen as erosion criterion. This criterion is similar to what has been employed by other authors [70–72] in simulations of concrete plates in LS-DYNA, where the total principal tensile strain was used. Since elastic strains only make up a very small part of the total strain when concrete is close to failure, using the total principal tensile strain versus the plastic principal strain should not be much different. All four experiments were simulated using 5 mm elements to get a more realistic visualization of cracks, and no additional changes were made to the models regarding material properties etc.

8.2.1 Plain concrete

Results from the simulations of plain concrete are presented in Figure 8.4. The back and side of the plates are shown at different times during the loading process (1.25 ms and 10 ms), so that the evolution of damage can be compared for the two plates. It comes as no surprise that the plate at high pressure, P-77, totally disintegrates, considering that it also collapsed without erosion (see Figure 8.3c). However, it was surprising that P-41 collapsed, since the previous simulation without erosion (in Figure 8.3a) suggested that it barely survived the blast load. There are some noticeable differences between the two plates. First of all, P-41 seems to experience a flexural failure, perhaps in combination with localized shear close to the center, while P-77 fractures due to concentrated shear bands along the boundary. According to Section 4.3, these are typical failure modes in plates subjected to low and high intensity dynamic loads, respectively. Secondly, the high-pressure plate evidently fails much more violently than the latter, due to the more powerful blast load. This results in smaller fragments, and overall a bigger amount elements are eroded than in can be observed in P-41. Comparing the failure mechanism to the experiment by Haug and Osnes where the plate fully collapsed (Figure 2.2), the simulations with element erosion are not in agreement, since the simulations are seen to produce very small fragments as opposed to large chunks. Moreover, a significant amount of elements are eroded, ultimately resulting in a non-physical collapse mechanism.

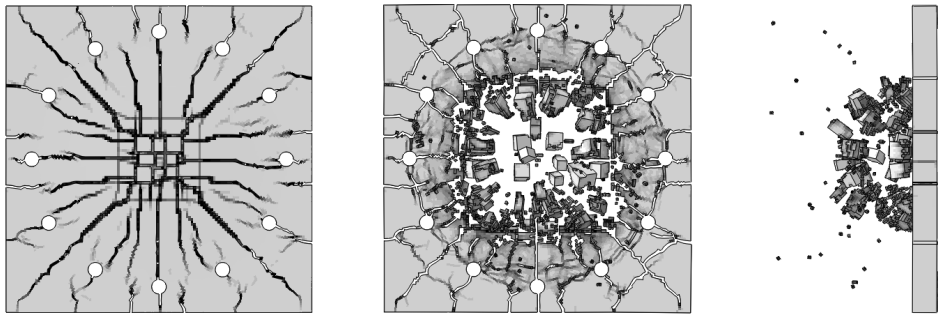

(a) 1.25 ms, P-41 ***(b)*** 10 ms, P-41 ***(c)*** 10 ms, P-41

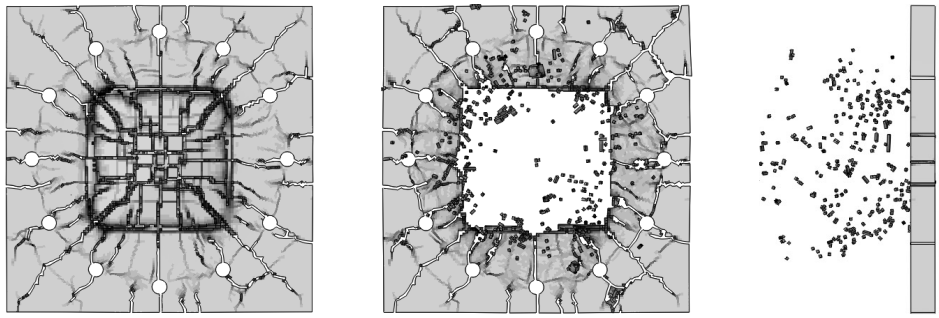

(d) 1.25 ms, P-77 ***(e)*** 10 ms, P-77 ***(f)*** 10 ms, P-77

Figure 8.4: *Element erosion employed in the plain concrete blast simulations. The top figures (a), (b) and (c) are from the low-pressure simulations (P-41), while the bottom figures (d), (e) and (f) are from the high-pressure simulations (P-77). The back and side views of the plates are presented, with both eroded elements and the maximum plastic principal strain shown.*

8.2.2 Reinforced concrete

Results from the simulations of reinforced concrete are presented in Figure 8.5. The back of the plates are shown in five of the six figures, wherein the maximum plastic principal strain field is shown in grayscale, and through-cracks can be distinguished by their white background. Quite good agreement is observed between the damage from the experiment and the simulated damage for the low-pressure reinforced plate (R-41). Moreover, the cracks arrest rather than continue to propagate throughout the simulation, and no cracks go through the thickness of the plate. This is readily seen in Figure 8.5c, in which the cross section of R-41 at maximum damage is displayed. From the figure it can be seen that the cracks at the center of the plate arrest midway through the plate thickness. This is not the case for the high-pressure plate (R-77). The initial damage seems reasonable, however elements continue to erode throughout the simulation in a very gradual and non-physical manner. This results in excessive damage, as can be observed in Figure 8.5f. A reason for this incorrect deterioration of elements might be that the erosion criterion

is not optimal, or that the failure strain is set too low.

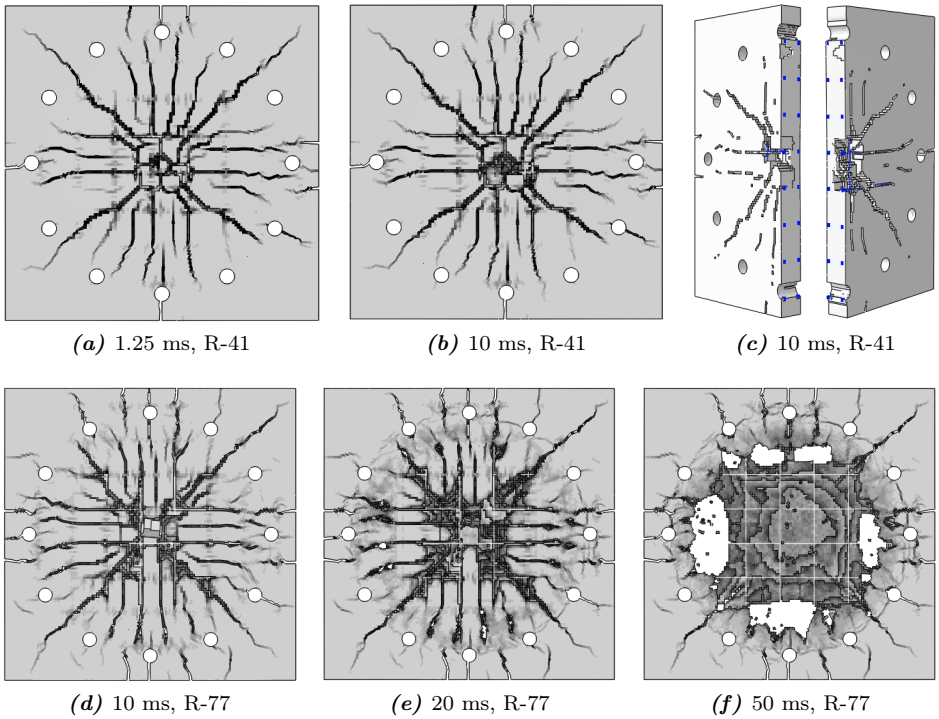

(a) 1.25 ms, R-41 ***(b)*** 10 ms, R-41 ***(c)*** 10 ms, R-41

(d) 10 ms, R-77 ***(e)*** 20 ms, R-77 ***(f)*** 50 ms, R-77

Figure 8.5: *Reinforced concrete plates simulated with element erosion in Abaqus. The top figures (a), (b) and (c) are from the low-pressure simulations (R-41), while the bottom figures (c), (d) and (e) are from the high-pressure simulations (R-77). The cross section of R-41 is shown in (c), and the rebar mesh has been highlighted blue to make it more distinguishable.*

8.3 Effect of random element strength

A study on the stochastic behavior of concrete was conducted in Section 7.5 of the preliminary analysis, in which the required element mean strength and standard deviation in element strength to reproduce the compressive strength distribution of concrete cubes were determined. A brief recap is given in Table 8.4. However, since the entire study was based on cube compression simulations, the obtained results say little about the stochastic nature of the tensile properties. Due to the lack of this knowledge, the tensile strength distribution employed in this section had to be assumed equal to the compressive strength distribution. Thus, an element will be given the same relative strength in tension as in compression. The tensile mean strength remains 5.7 MPa. Figure 8.6 shows one if the models with strength variation in Abaqus.

Element size [mm]	μ_i [MPa]	μ_i^T [MPa]	σ_i [MPa]	σ_i^T
10	50	5.7	15	1.7

Table 8.4: *Variable employed in the strength variation analysis. μ_i and μ_i^T are the compressive and tensile mean element strengths, respectively, while σ_i and σ_i^T are the standard deviations in element compressive and tensile strength.*

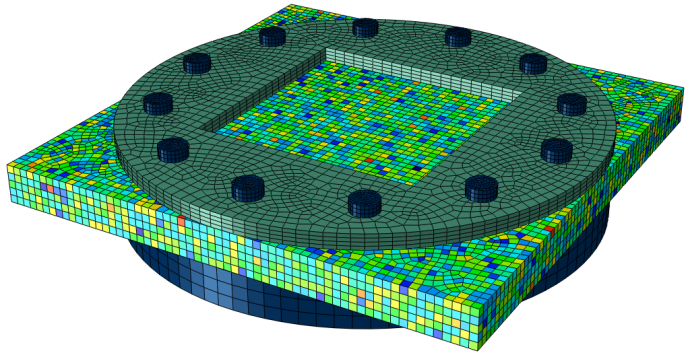

Figure 8.6: *Plate simulation assembly with stochastically distributed strength. Blue elements indicate low strength and red elements indicate high strength.*

Midpoint deflection curves are presented in Figure 8.7. It is immediately observed that the effect of including random element strength in the model is negligible on the overall capacity and deflection of the reinforced plates. The plain plates experience a greater, yet still quite insignificant, effect from random element strength. This is particularly noticeable in Figure 8.7c, where the plate with variation seems to experience a total collapse, while the uniform plate does not. Three simulations were run for each of the plates subjected to low pressures, each with its own unique spatial distribution of concrete strength. The displacement curves from all three simulations are included in Figures 8.7a and 8.7b, however they are virtually identical, hence the difficulty in distinguishing them from one another. Due to time limitations, only one simulation was run for each of the plates subjected to high pressure.

Table 8.5 shows the resulting crack patterns from the plates with strength variation, with the experimental results included in the figures as previously. Crack patterns from the uniform plate analyses are included in the leftmost column of the table. While adding element strength variation has little effect on the deflection of the plates, the crack patterns are greatly affected in that they become much more erratic and asymmetrical. In this regard, the response becomes more realistic when element strength variation is taken into account. However, the simulated damage is still excessive when compared with the experimental results. The effect of the reinforcement mesh on the crack pattern is still observed, although it is less prominent.

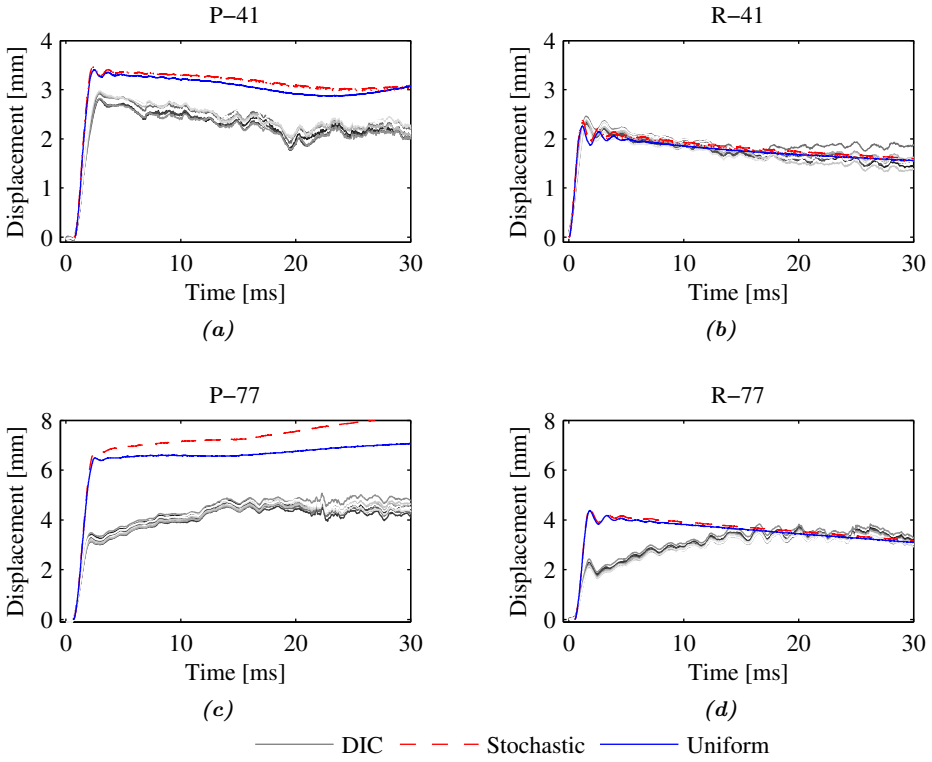

Figure 8.7: *Midpoint deflection plotted against time for the stochastic plate simulations in Abaqus. Like in the previous section, the DIC-measured midpoint deflections are included in the these figures for comparison. The figures to the left are from the plain concrete simulations at low (a) and high (c) pressures, while the two on the right are from the reinforced concrete simulations at low (b) and high (d) pressures.*

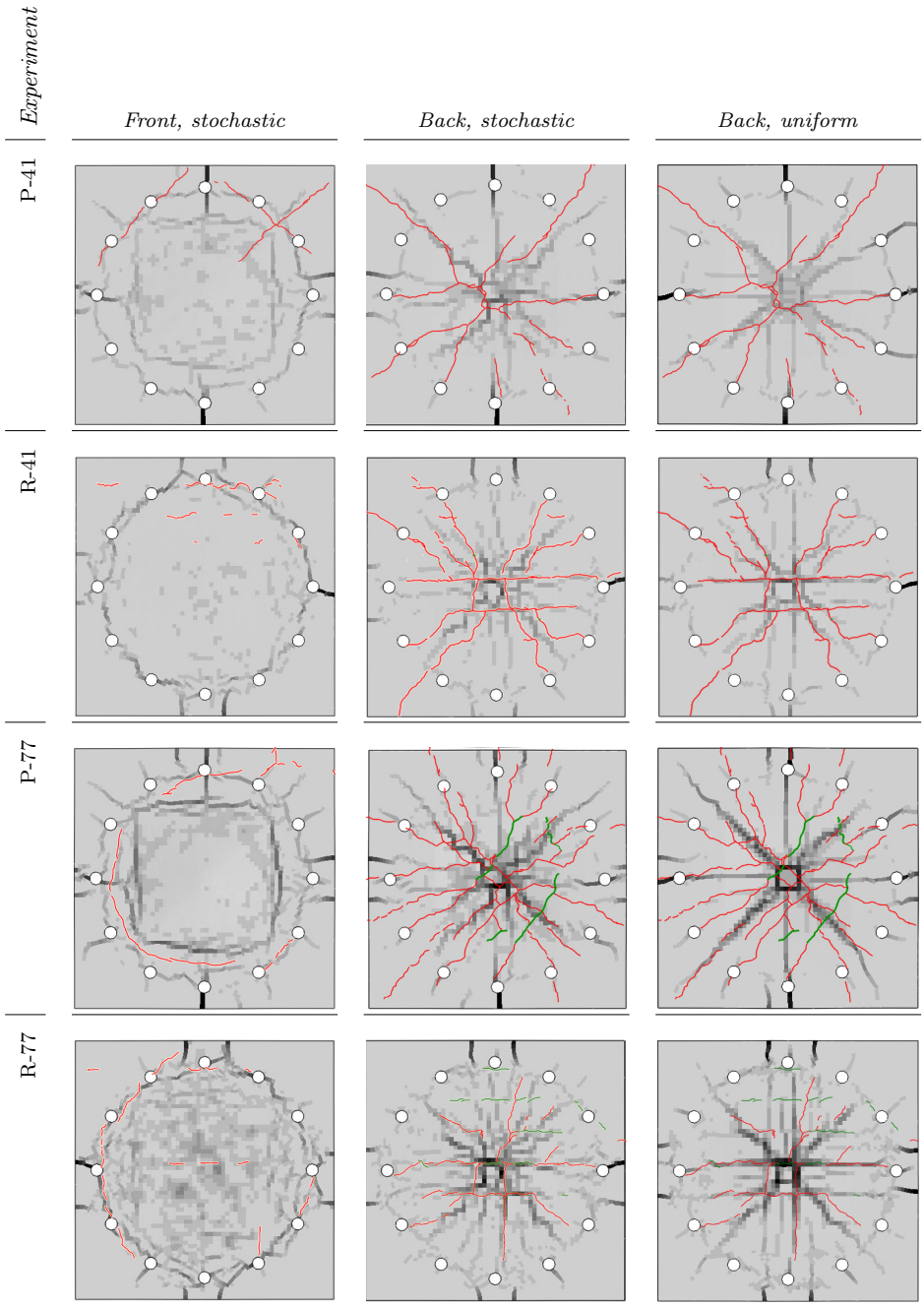

Table 8.5: *Simulated crack patterns in Abaqus. Darker shade indicates higher principal plastic strain, while the red lines represent the experimentally observed cracks.*

8.4 Summary and discussion

Blast load simulations have been run with the CDP model in Abaqus/Explicit, and mesh sensitivity, the effect of element erosion and the effect of random element strength has been investigated.

The CDP model shows strong mesh sensitivity in simulations of plain concrete plates. Mesh refinement drastically reduces the plate capacity due to the localization of strains in narrow crack bands. Evidently, the remedy is to add reinforcement, which acts as a regularization and removes mesh dependence altogether. According to the documentation [45], reinforcement is known to have this effect in the CDP model. Furthermore, good agreement is observed between the crack patterns in the coarse and fine meshes, however, more distinguishable cracks are achieved with the fine meshes.

The implementation of a simple user defined erosion criterion has been successful. With erosion it becomes much easier to assess damage and to determine whether total collapse occurs in the plates, and to determine which mode of fracture is occurring. However, the results suggest that the erosion criterion may overly reduce the plate capacity, and that it can even give non-physical behavior in some cases. This is especially apparent in the reinforced plate at high pressure (R-77), where elements continue to erode throughout the simulation and the plate thus very gradually disintegrates. The damage in Figure 8.5f is simply too excessive and perhaps unrealistic, and does not agree well with the deflection curve in Figure 8.7d. This indicates that the accuracy and validity of the simulations with a simple strain based erosion criterion diminishes after a certain point, given that the plate is subjected to a sufficiently powerful pressure load. An interesting task would therefore be to study the effect of changing the failure strain in the erosion criterion, and perhaps implement a more sophisticated erosion criterion.

Very little change in displacement was observed when random element strength was incorporated into the model, in particular for the reinforced plates. Moreover, three simulations were conducted for each of the low-pressure experiments, and they all produced equal results. It was expected that this simple stochastic model should at least have a noticeable effect on the displacement, which it did not. Since only one experiment was conducted on each plate configuration, it is not known if this is realistic. The assumption made regarding the tensile strength distribution may be too simple, and further work should investigate the tensile properties of the random element strength method used herein. While the change in capacity is negligible, crack patterns are greatly affected by random strength in that they become much more erratic and irregular. In this regard, the simulations with random strength produce more realistic results. It is also important to note that the irregular mesh in some regions of the concrete plates, as seen in Figure 8.2, cause a certain degree of irregular cracks also in the simulations with uniform material formulation. Hence, it is possible that the random element strength method may be better justified in simulations where the mesh is fully regular, and unrealistic symmetrical crack patterns are likely to occur, as also pointed out by [66].

Overall, the CDP model in Abaqus yields qualitatively good results for the concrete plates, in particular at low pressures and when reinforcements are included. Moreover, it is capable of capturing the different crack patterns in plain and reinforced concrete. However, the simulations revealed that the accuracy of the predicted deflection is reduced when the pressure load is increased. It may be that as pressures get sufficiently close to the maximum capacity of the plate, the predicted response becomes increasingly incorrect. This would indicate that the CDP model struggles only when the material is near failure, however, further studies are required to have this confirmed. It is also recognized that the accuracy of these simulations is inherently reduced as through-cracks form. This can be attributed to the lack of FSI-effects in the simulations. As cracks grow through the thickness of the plates, the load changes since pressure escapes through the cracks. Hence, in order to accurately capture the whole collapse sequence of the plates, FSI simulations are required.

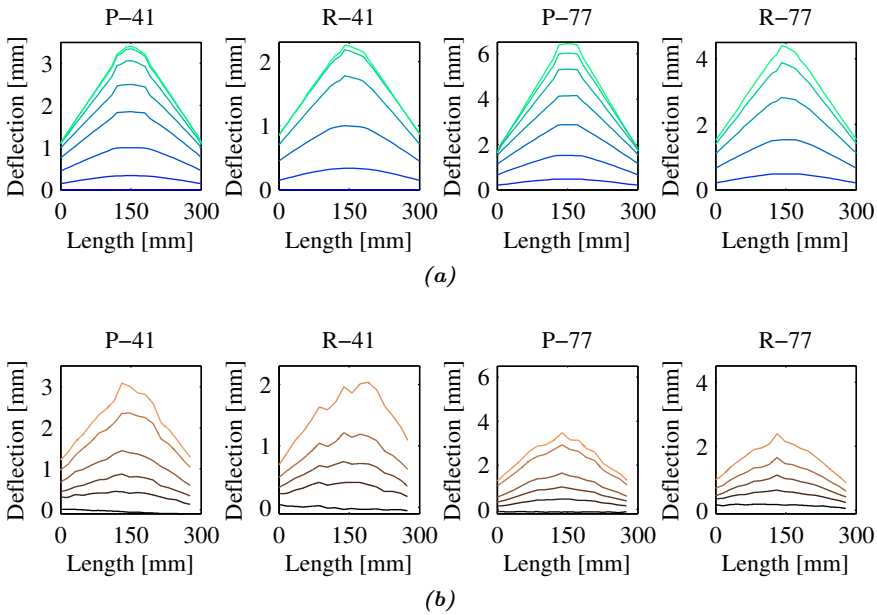

Figure 8.8: *The deflection profiles of the simulated concrete plates (a) and tested plates (b), during approximately the first 1.50 ms of the blast.*

A closer comparison between the results from the plain and reinforced plate simulations is presented in Figure 8.8, in which the simulated deflection profiles are presented in Figure 8.8a, and the matching DIC-measured deflection profiles are presented subsequently in Figure 8.8b. A clear distinction is immediately seen between the plain and reinforced simulated plates, namely the mode of failure. Both plain plates experience a combined shear-punching and flexural failure, while pure flexural failure dominates in the reinforced plates. Notice how the plain plates deform into flat cones, while the reinforced plates end up with a pyramid-shaped

deflection. Moreover, the DIC-measured deflection profiles indicate that in fact all plates experienced flexural bending, and little influence from shear can be observed. The displacement along the boundary is likely due to the bending of the aluminium clamping plate (and the rigid body motion of the shock tube in the experiments). Thus, the results again suggest that the simulations of reinforced concrete yield more accurate and physically correct results.

In the preliminary analyses, effort was put into calibrating the input compressive and tensile strengths in the CDP model. Despite of this, three of the four plate simulations (P-41, P-77 and R-77) predict an overly soft response, with excessive crack formation. Thus, the calibrations based on material tests in the preliminary analysis have not been successful in that the plate simulations predict an overly conservative estimate of the real plate response.

Figure 8.9 shows a magnified view of the deflection curve for the best simulation, R-41, and it is readily seen that perfect correlation between the experiment and the simulation is not achieved. The stress-strain curve could not be calibrated for the concrete due to limited resources, and the stiffness of the concrete was also not measured specifically.

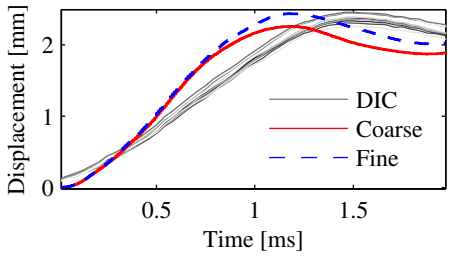

Figure 8.9: *Midpoint deflections for the best matching simulation, R-41, in closer detail. The simulation results from both meshes and the DIC-measurements are included.*

8.4.1 Energy considerations

Energy balance checks were performed for all of the simulations in order to assess the validity of the solutions. In addition, it was of interest to determine the amount of hourglass energy, i.e. energy dissipated due to the artificial stiffness introduced by the solver to remedy zero-energy modes, as briefly introduced in Section 3.2.2. Therefore, the components of the internal energy were studied individually. All the simulations exhibited similar trends in energy balance, thus only one of them, R-41, is considered in the following. Figure 8.10 below illustrates both the energy balance and the components of the internal energy for test R-41, in which Figure 8.10a shows the first 7 ms of the simulation, while the entire simulation is shown in Figure 8.10b. As indicated by the blue dashed line, the energy balance is approximately constant throughout the simulation, so numerical instability is not an issue. Moreover, the hourglass energy is initially fairly low, but it increases

alarmingly as the simulation progresses. However, most surprising is the strain energy which rapidly descends downwards to large negative values. Physically, this response is simply impossible, and the authors' initial response was that it had to be erroneous. An explanation was sought, but neither the Abaqus documentation nor other articles were helpful, thus the uncertainties regarding the strain energy remain unanswered. It could be that the CDP model employs an odd definition for the strain energy that permits negative values. Figure 8.11 below shows the total energy absorbed by the plate, and the result seems reasonable despite the questionable strain energy in Figure 8.10b.

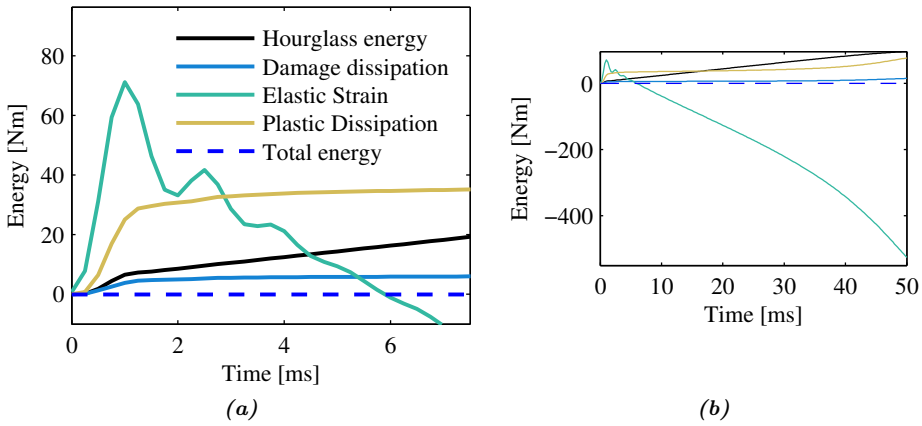

Figure 8.10: *Internal energies, zoomed in region in (a) and for the entire simulation in (b), in addition to the total energy showing the energy balance.*

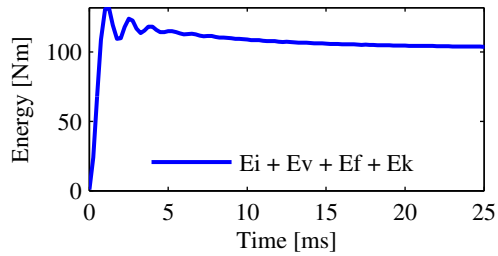

Figure 8.11: *Total energy absorbed by the plate due to the pressure load. The curve represents the sum of the internal energy Ei, the dissipated viscous energy Ev, the dissipated frictional energy Ef, and the kinetic energy Ek.*

It should not go unnoticed that fairly large hourglass energies were produced in the simulations. This was particularly prominent for the simulations that predicted total collapse, i.e. P-77 with fine mesh. Through the findings presented in this section, it goes to show that simulating blast loads with the CDP model is not trivial, and the issues regarding energies should be further addressed in the future.

Chapter 9

Simulations of Concrete Plates in LS-DYNA

The simulations in LS-DYNA were performed using the same reference model as the simulations in Abaqus, but with one difference. In Abaqus, the M24 bolts were constrained to the inside of the bolt holes in the shock tube flange, and a cross-sectional force was assigned to the bolts. Prior to the blast simulation, a static step was run where the bolt preload equilibrium was calculated. In LS-DYNA, the bolt preload was instead introduced by assigning a displacement of 0.12 mm to the bolt ends during the first millisecond of the explicit analysis, while keeping the flange fixed. This introduced a bolt preload of around 30 kN.

The element types and material properties were the same as in Table 8.2, except for the rebar mesh and the concrete, which was modeled with bilinear hardening and the K&C-model, respectively. The hardening parameters for the rebar mesh were found earlier, and are given in Table 5.17b. For the concrete, the tensile strength was found by inverse modeling in Section 7.4.2, and the compression strength was corrected due to ageing according to Figure 5.8. The final material properties are given in Table 9.1.

In those simulations where the rebar mesh is included, it has been connected to the concrete by use of the **Constrained Lagrange in Solid* (CLIS) card in LS-DYNA, with the parameters suggested by Schwer in [73]. The rebar mesh was the same as in the Abaqus analyses, only with beam elements instead of truss elements. The elements of the rebar mesh were around 7 mm for the simulations in this chapter. Reduced integration brick elements were used for all solids, and the default LS-DYNA hourglass-control algorithm was used with an hourglass coefficient of 0.1.

The effect of different mesh sizes in LS-DYNA has been studied, as well as the effect of including strain rate sensitivity in the concrete model formulation. Finally, the effects of random strength variation and mesoscale modeling have been investigated.

f_t [MPa]	f_c [MPa]	ν	ρ [kg/m^3]
4.8	42.3	0.2	2440

Table 9.1: *Concrete material properties used for the simulations in LS-DYNA.*

9.1 Effect of mesh

Changing the mesh size should ideally not change the behavior of the simulations, as long as the mesh is sufficiently fine. However, since the concrete plates are prone to cracking, smaller elements will produce a more narrow crack band, and some mesh dependence is thus difficult to avoid. As with the analyses in Abaqus, each experiment has been attempted replicated with two different mesh sizes of 5 (coarse mesh) and 10 (fine mesh) elements over the plate thickness. The severity of this mesh dependence under different conditions is investigated in the following.

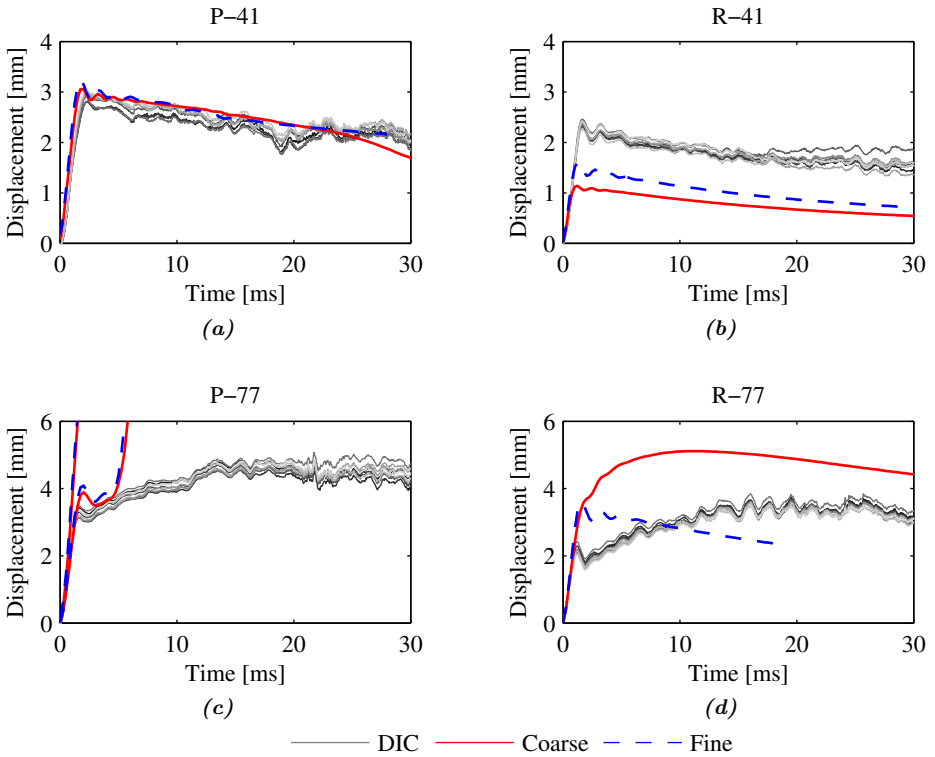

Figure 9.1: *Simulated displacement-time curves from the shock tube experiments, shown together with the DIC measurements.*

The results from the mesh sensitivity study are seen in Figure 9.1 and Table 9.2, where the time-displacement curves and resulting crack patterns are shown. The

experimentally observed crack patterns are projected onto the simulated crack patterns in the form of red lines. From the time-displacement curves, it can be seen that the solution is not mesh dependent for the plates without reinforcement, while some deviation is seen for the reinforced plates. The simulations of P-41 corresponds best with the experimental data, and very good correlation is seen. In the simulations of P-77, total collapse of the plate occurs for both meshes. The time-displacement plot of P-77 shows the displacement at two different nodes, one at the position of incipient failure and one slightly outside this region, and it can be seen that the latter node experience rebound before full collapse occurs. This indicates that the plate is probably very close to withstanding the blast load in the simulation.

The simulations of the reinforced plates are either too stiff or too soft. In the simulations of R-41 the experimental displacement is underestimated by 1-1.5 mm, but the shapes of the curves are similar to the experiment. For R-77, the simulated displacement with fine mesh is similar in shape to the simulations at 41 bar driver pressure, but overestimates the initial displacement by around 1.5 mm. In the simulation with coarse mesh, the plate is severely damaged in the middle and starts to drift outwards, before it retracts once the pressure has decayed enough. The shape of this curve is similar to the experimental curves, but it is not known if the shape of the experimental curve is due to damage alone or some other phenomenon. It is possible that the large deviation between the fine and coarse mesh in the simulation of R-77 occurs since the plate is close to collapsing, and that the solution therefore is sensitive to small changes in the model set-up.

The crack patterns in Table 9.2 show that excessive cracking is generally the case for both the fine and coarse meshes. At the front surfaces, the cracking is much more severe in the simulations than in the experiments, while the back surfaces are more in agreement with the experimental observations. The simulated crack patterns at the back surfaces of P-41, R-41 and R-77 all capture most of the cracks that were observed experimentally, but they also predict some cracks that were not seen in the experiments. For the reinforced plates, the cracks in the center of the back surface of the plates seem to follow the rebar, which is also in agreement with the experiments. The simulation of P-77 is not in agreement with the shock tube test of P-77 since total collapse did not occur in the experiment. However, the circular crack at the front of P-77 fits well with the experiment, and some of the cracks in the clamped region at the back of the plate are also in good agreement.

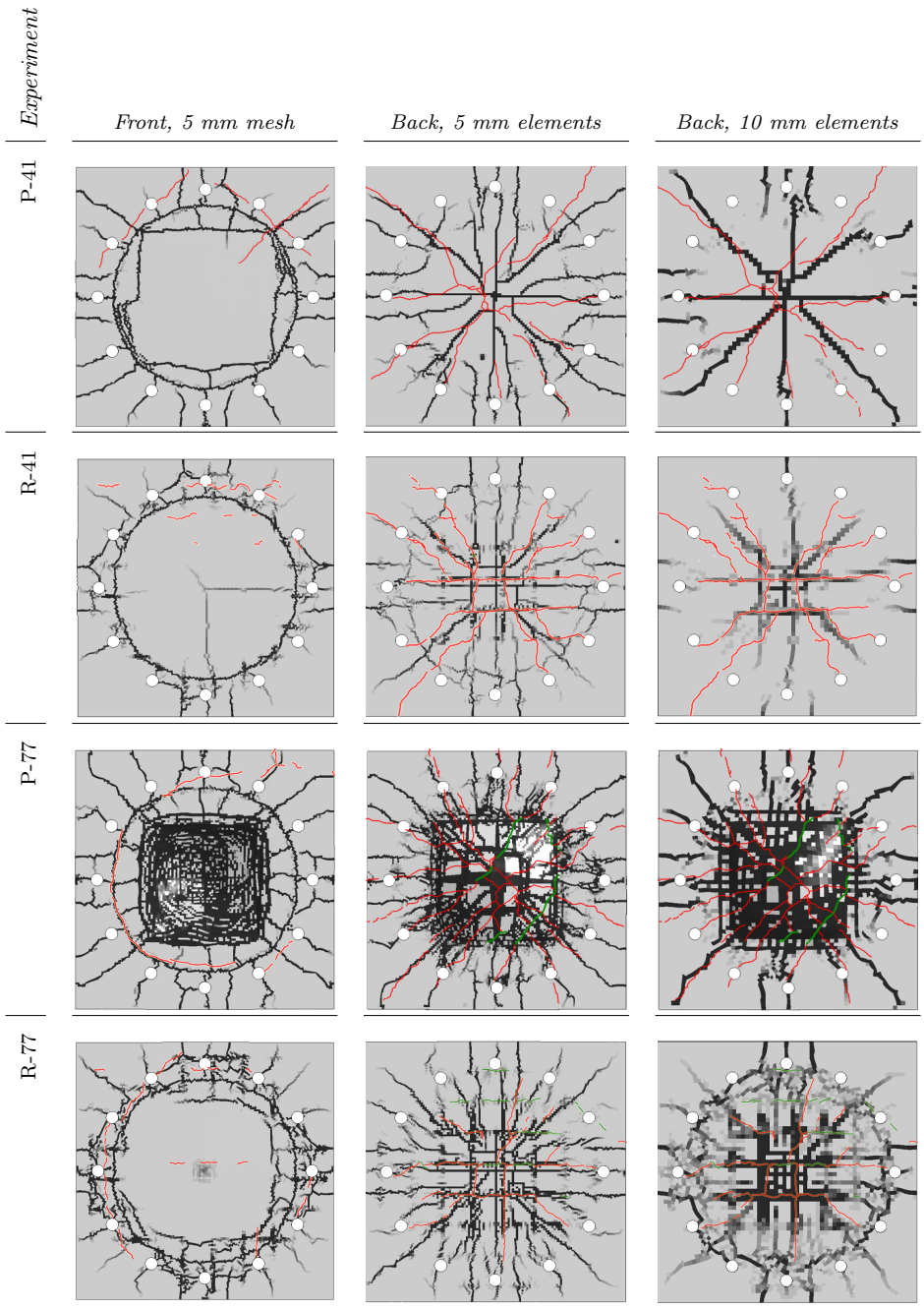

Table 9.2: *Simulated crack patterns with different mesh sizes. 5 mm elements equates to 10 elements over the thickness of the plate, while 10 mm gives 5 elements over the thickness.*

9.2 Effect of strain rate dependence

In Section 4.2.4, the strain rate dependent behavior of concrete was discussed. In the following simulations, strain rate dependent material behavior has been included to study its effect on the blast loaded concrete plates. The LS-DYNA manual suggests a strain rate enhancement curve for the K&C-model, and this curve has been used in the following. Figure 9.2 shows the dynamic increase factor (enhancement factor) plotted against the strain rate.

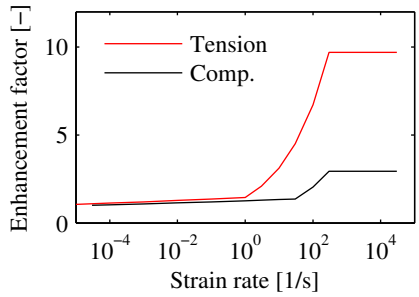

Figure 9.2: *Rate enhancement factor curve suggested in the LS-DYNA manual [74].*

Since the unreinforced plate at 77 bar driver pressure collapsed catastrophically in the previous simulations, it is of particular interest to see if including material rate dependence can remedy this discrepancy. Also, the effect of rate dependence on P-41 will be studied, since good correlation was achieved for this experiment without including rate dependence. The simulations were run with a fine mesh of 10 elements over the thickness since this produced a more detailed crack pattern in the previous simulations.

Figure 9.3 shows the resulting displacement curves from the simulations. Taking strain rate dependent material behavior into account is seen to stiffen the response of the plates significantly. The maximum displacement of P-41 is reduced from around 3 mm to only 0.7 mm, which is much less than what was measured during the experiment. The behavior of P-77 also became stiffer, and it did not collapse when rate dependence was included. However, the behavior was stiffer than the measured displacement from the DIC, and some irregular behavior was present at around 2-5 ms into the simulation.

The resulting crack patterns in Table 9.3 reveal that P-41 was close to not suffering any damage in the simulation with rate dependent concrete. Only minute cracks have formed at the back surface, which is less than what was observed in the experiment. At the front, however, an excessive amount of cracking is seen compared with the experiment. This is also true for the front surface of P-77. Good correlation is seen for the back surface of P-77, with an almost equal amount of cracking in the simulation and experiment. Furthermore, many of the cracks in the experiment are predicted in the simulation, even though the cracks in the

experiment generally are more erratic.

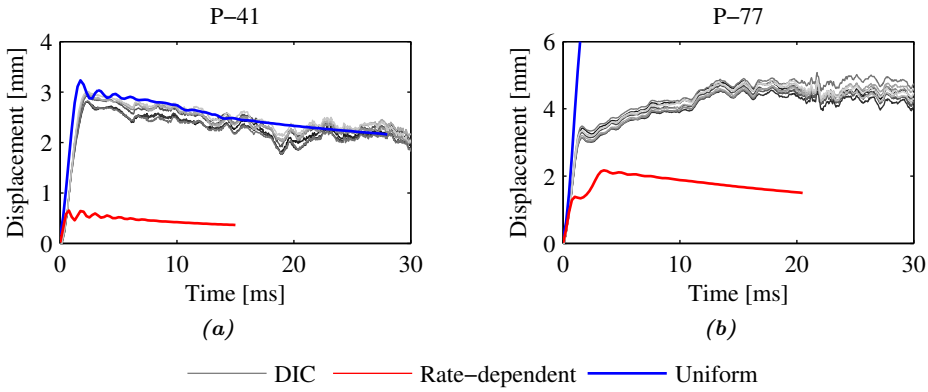

Figure 9.3: *Displacement-time curves from the simulations with strain rate dependent concrete.*

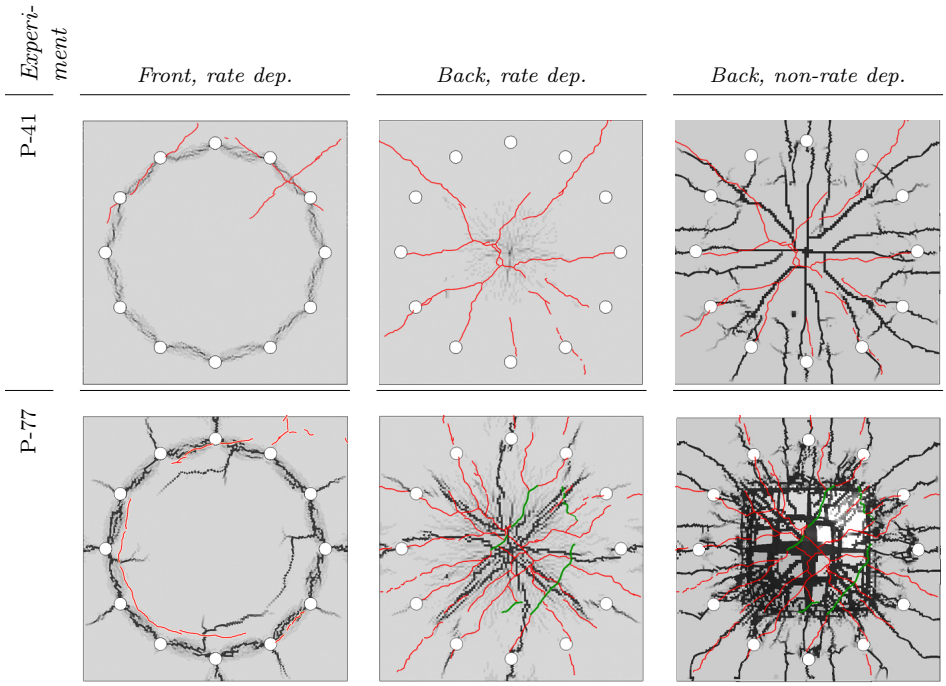

Table 9.3: *Simulated crack patterns with rate dependent concrete in LS-DYNA.*

Figure 9.4 shows the 1st principal strain and strain rate in the element of maximum strain for the two simulations. It is seen that the maximum strain rate is around 20

s^{-1} and 55 s^{-1} for P-41 and P-77. From Figure 9.2, this is seen to correspond to a rate enhancement factor of maximum 4 and 5.6, respectively. At these strain rates it is expected that the concrete should be stronger than in quasi-static loading, but is seems that the rate enhancement curve suggested in the LS-DYNA manual may be too generous for the concrete studied in this thesis.

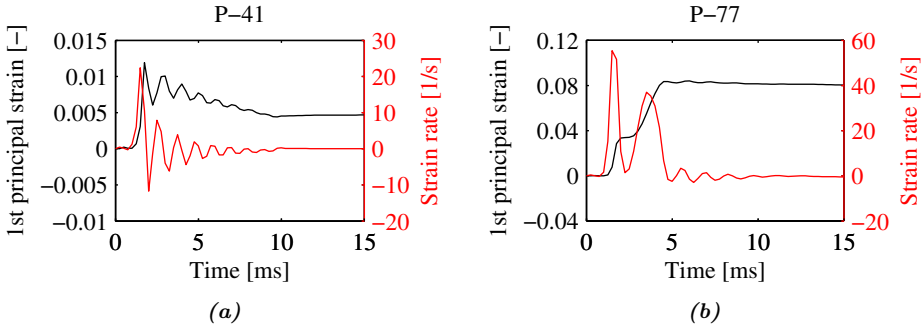

Figure 9.4: *1st principal strain and strain rate in element of maximum strain for (a) P-41 and (b) P-77. The element of maximum strain was located in the center of the back surface of the plate.*

9.3 Effect of random element strength

The effect of including random element strength in the concrete was investigated in LS-DYNA. In Section 7.5 it was found that 10 mm elements with an average element strength of 50 MPa and a standard deviation of 15 MPa was able to recreate the stochastic distribution observed in the cube compression tests. Hence, the same element size and strength distribution was used in the following simulations. It was assumed that the ratio between tensile strength and compressive strength would be constant for all the elements, i.e. that a strong region would be strong in both tension and compression and conversely weak for a weak region. Table 9.4 summarizes the strength distribution used in the stochastic analyses.

Element size [mm]	μ_i [MPa]	μ_i^T [MPa]	σ_i [MPa]	σ_i^T [MPa]
10	50	4.8	15	1.44

Table 9.4: *Strength distribution for the LS-DYNA stochastic analyses. μ_i and μ_i^T are the compressive and tensile mean element strengths, while σ_i and σ_i^T are the standard deviations in element compressive and tensile strength, respectively.*

In order to assess the sensitivity of the simulations to the spatial distribution of strong and weak regions, the simulations of P-41 and R-41 were run three times, each with an individual spatial distribution of concrete strength, as was also done in the Abaqus analyses. The displacement curves and crack patterns from the

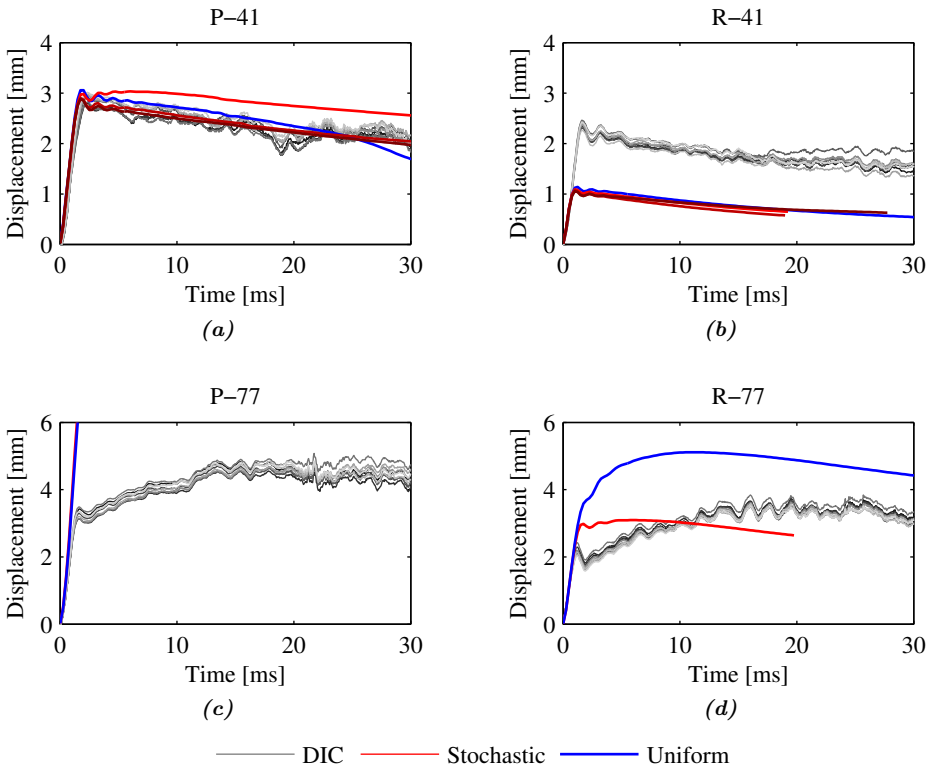

Figure 9.5: *Displacement-time plots from the stochastic simulations of the shock tube experiments, shown together with the DIC measurements.*

stochastic simulations are shown in Figure 9.5 and Table 9.5. The displacement curves show that the behavior did not change significantly for P-41, R-41 and P-77, while the behavior of R-77 became stiffer and resembled the simulation of R-77 with fine mesh in Figure 9.1d. Changing the spatial distribution of strength did have some effect on P-41, where one simulation in particular behaved softer than the two others. For the reinforced plate, however, changing the spatial distribution produced only a negligible difference in response. As in the previous section, the simulations of P-77 predicted total collapse of the plate.

Including random element strength produced more erratic crack patterns than the simulations with uniform strength, and predicted less damage for the reinforced plates. Still, the amount of damage is generally excessive in the simulations, especially at the front surface of the plates. For P-41 in particular, the crack pattern from the stochastic simulation became much more erratic than the simulation with uniform material, resulting in a more realistic crack pattern. For the reinforced plates, on the other hand, the crack patterns became less well-defined and did not

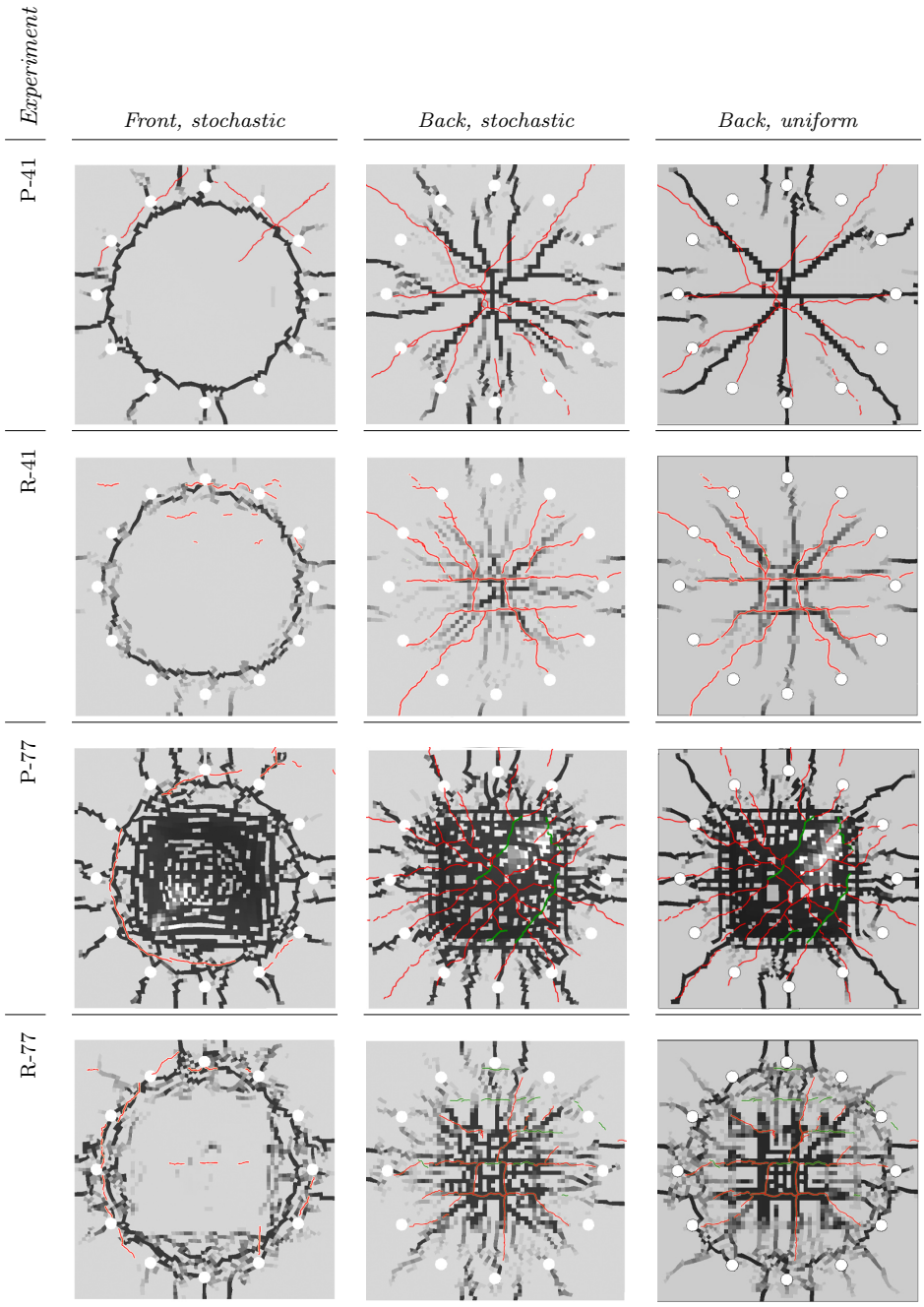

Table 9.5: *Simulated crack patterns with stochastic distribution of element strength in LS-DYNA.*

significantly improve the correlation with the experimental results.

9.4 Effect of mesoscale modeling

Simulations of cube compression tests with the mesoscale method proved to describe both the stochastic variation in cube strength and the crack patterns of the cubes with good accuracy. Because of this, it was decided to model the concrete plates with the mesoscale method. These simulations were performed with the same simulation set-up as previously, but some changes had to be made. First, the mesh of the concrete plate had to be refined sufficiently to capture the spherical shape of the aggregates. Since only a small difference was seen between the meshes of 125 000 and 512 000 elements in the cube simulations, it was decided to use an element size corresponding to the coarser mesh. This resulted in 25 elements over the thickness of the plate, and a total of almost 2 700 000 elements. Also, in order to capture the interaction between fractured pieces of concrete, the contact formulation had to be changed for some parts of the model. The contact card *Contact Eroding Single Surface* was therefore used instead, with contact defined between the cement matrix, aggregates, shock tube flange and clamping plate. Moreover, the aggregate generation algorithm was modified to account for the rebar mesh in some of the plates. A new aggregate placement criteria was added so that no aggregates would be generated where there was rebar, thus preventing the rebar to go through any of the aggregates. The holes in the concrete plates were not taken into account when generating the aggregates. The resulting mesostructure with a rebar mesh is shown in Figure 9.6. As earlier, both the aggregate and the cement matrix were modeled with the K&C-model with uniaxial compression strengths of 200 MPa and 30 MPa, respectively. Simulation of the experiments P-41 and R-41 were performed with the concrete modeled by the mesoscale method. The results from these simulations are presented in the following.

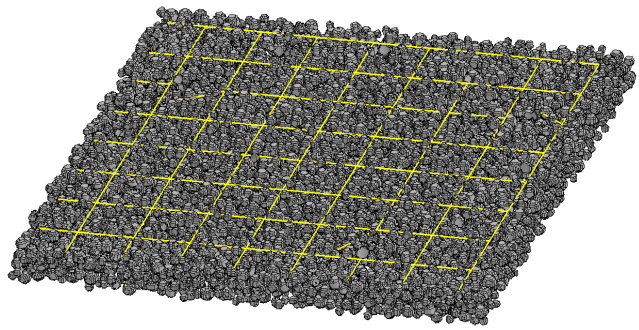

Figure 9.6: *Finite element model of reinforced concrete plate with mesoscale concrete model. The cement matrix has been hidden in this view.*

9.4.1 Plain concrete

The simulation of P-41 predicted total collapse of the plate. Since only minor damage was seen in the experiment, this is not in agreement. The collapse sequence is shown in Figure 9.7, in which it can be seen that the plate behaves in a very brittle manner, and a lot of cracks have formed before the shock wave hits due to the bolt preload. Once the shock wave hits, a large number of cracks form at the back of the plate. These cracks gradually grow deeper until they penetrate the plate, causing large chunks of concrete to be ejected from the plate.

While the capacity of the plate is substantially underestimated by the mesoscale simulation, the overall behavior seems physically correct. By closer inspection of the crack patterns and fracture surfaces, it is seen that the cracks propagate around the aggregates. This makes sense since the aggregates have been modeled with much higher strength than the cement. Still, the crack pattern does not resemble any of the crack patterns seen in the experimental tests, as there are few cracks propagating radially outward from the middle of the plate. Moreover, the failure mode is seen to resemble that of punching shear, as there is a circular region in the middle of the plate that is encircled by deep cracks. It is seen that the concrete breaks up into large chunks instead of small pieces as in the simulations with erosion in Abaqus in Section 8.2. This is similar to the failure sequence seen by Haug and Osnes in the test where the plate was totally obliterated, shown in

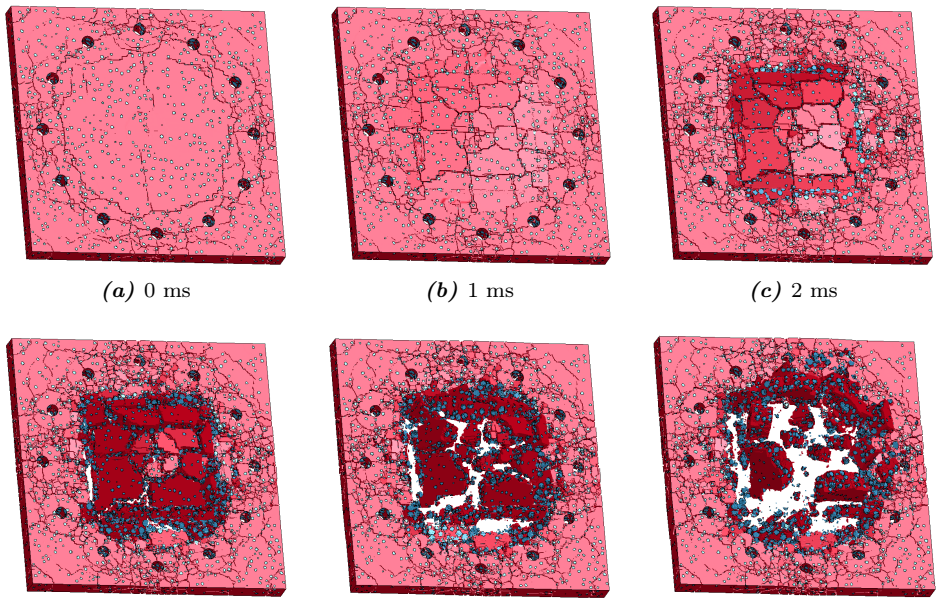

(a) 0 ms ***(b)*** 1 ms ***(c)*** 2 ms

(d) 4 ms ***(e)*** 6 ms ***(f)*** 8 ms

Figure 9.7: *Damage evolution in unreinforced concrete plate subjected to a shock wave equivalent to experiment P-41, where the concrete has been modeled by the mesoscale method.*

Figure 2.2, where few and deep cracks dominated. This simulation was run locally on a laptop with a 4 core 2.1 GHz Intel i7 CPU and 16 GB ram memory. It took 73 hours to simulate 9 ms when running on 4 cores. As in the previous simulations in LS-DYNA, the first millisecond is used to apply preload to the bolts.

Simulation with increased cement tensile strength

Since the previous simulation predicted full collapse of the plate, it was attempted to run the simulation again with higher tensile strength of the cement matrix. In the previous simulation, where a uniaxial compression strength of 30 MPa for the cement matrix was used, the tensile strength was automatically generated by the K&C-model to a value of 2.9 MPa. In the following, the tensile strength was manually set equal to 4.8 MPa, which is the same as what was used for the other simulations in this chapter with uniform concrete.

Increasing the tensile strength of the cement matrix had little effect on the response of the plate in the simulation. As seen in Figure 9.8, both plates failed in roughly the same way, but the simulation with modified tensile strength predicted fewer small cracks in the clamped region of the plate. Also, less damage was predicted at the contact line between the concrete and clamping plate.

It was expected that increasing the tensile strength should cause the plate to become stronger, and while a small difference was seen, it is apparent that a more comprehensive study is needed in order to determine the appropriate material inputs for the mesoscale method.

9.4.2 Reinforced concrete

The running time for this simulation was 63 hours, after which it terminated due to lost contact with the licence server. It ran significantly slower than the previous mesoscale simulation, as it only got to 5.4 ms when running on 12 cores at the cluster facility at the department of structural engineering at NTNU. It was seen that the reinforced plate would also fail completely at this point, so the simulation was not restarted. This simulation also had to be run two times, as the first run experienced beam elements that were ejected from the concrete and elongated to several meters. The simulation was then run again with erosion added to the rebar mesh. Erosion was defined to occur at an effective strain of 0.8796, as found in Section 5.5. It was not expected that the rebar should fail in the simulations, and the purpose of adding erosion was to keep the simulation from experiencing unphysical behavior.

The damage evolution of the reinforced plate subjected to a shock wave equivalent to that of R-41 is shown in Figure 9.9. Adding rebar is seen to reduce the amount of cracking due to the bolt preload. At 0.5 ms after the shock wave has hit the plate, cracks have already started to form. At 1 ms, the amount of cracking is more

than in the plain mesoscale simulation at 1 ms, but the cracks are less severe. The rebar mesh is also starting to become visible, as many of the cracks have formed where the reinforcements are situated. Since the generation of the mesostructure has taken the rebar mesh into account in this simulation, and the tensile strength of the cement matrix is low, this was expected. Subsequent deformation occurs by

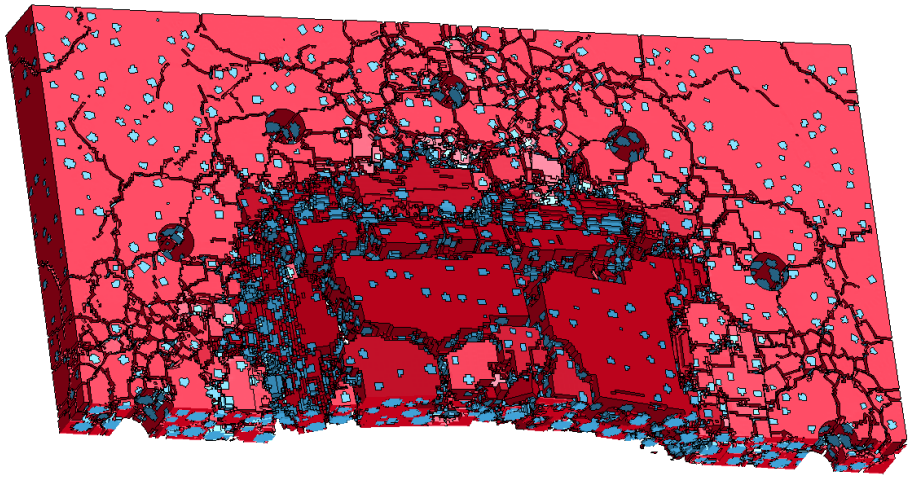

(a) 2.9 MPa cement matrix tensile strength

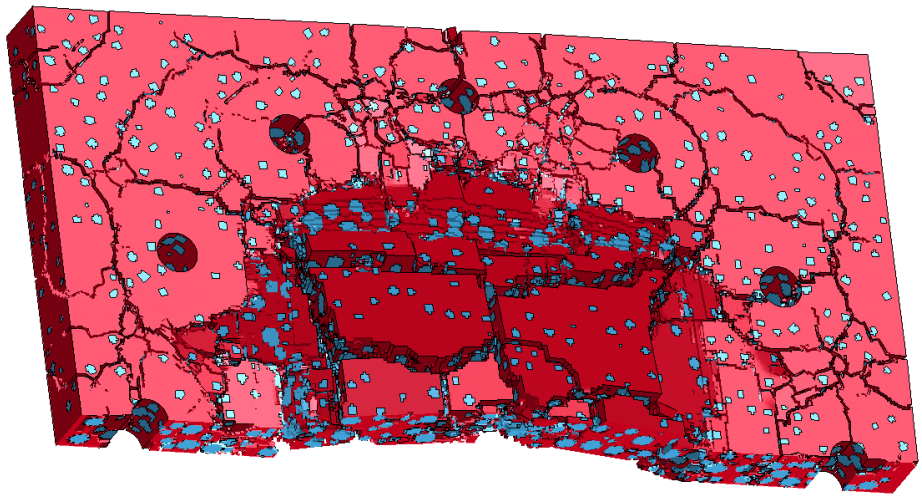

(b) 4.8 MPa cement matrix tensile strength

Figure 9.8: *Section view of the P-41 simulation with the mesoscale model, using (a) automatically generated cement matrix tensile strength and (b) modified tensile strength. The time in the simulation is t=3 ms, and the simulations have been performed with the same mesostructure.*

a combination of bending and shear failure. A significant amount of cement matrix material is eroded at the contact line between the concrete and the clamping plate, which causes the concrete plate to be pushed outward in a deformation mode resembling shear failure, as described in Section 4.3. At the front of the plate, much of the surface that is subjected to pressure is eroded, causing the rebar mesh to become visible. The mesoscale simulation of a reinforced plate is clearly not in agreement with the experimental results, as the amount of damage is vastly exaggerated. Also, adding reinforcement caused a substantial amount of material to be eroded from the front surface of the plate, and this caused an unrealistic behavior. Still, as in the previous simulation, the crack patterns up to 1 ms are highly random and erratic, and resemble that of real concrete.

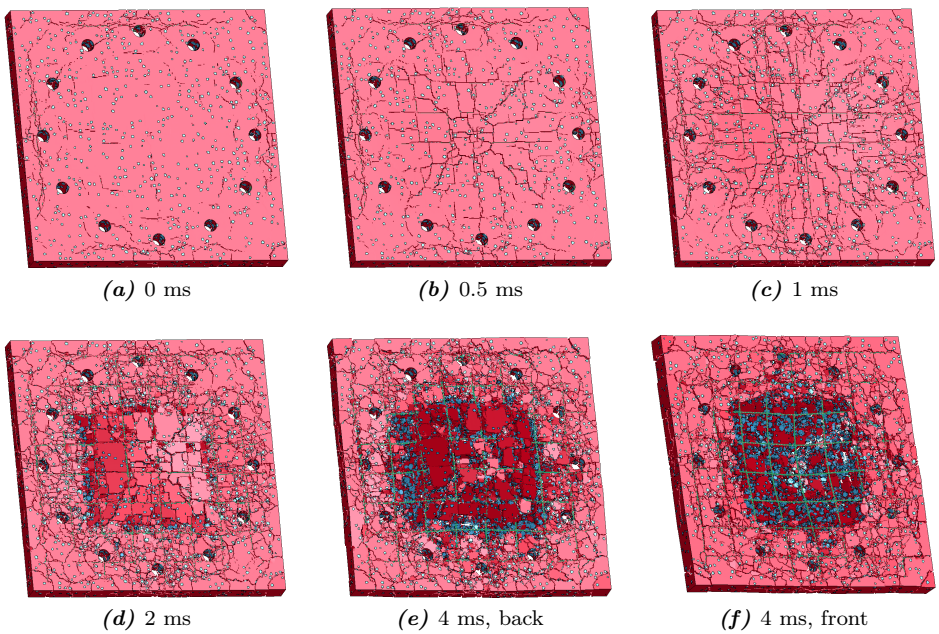

(a) 0 ms ***(b)*** 0.5 ms ***(c)*** 1 ms

(d) 2 ms ***(e)*** 4 ms, back ***(f)*** 4 ms, front

Figure 9.9: *Damage evolution in the reinforced concrete plate subjected to a shock wave equivalent to experiment R-41, where the concrete has been modeled by the mesoscale method.*

Comparison of behavior

Since the mesoscale simulations exhibited complex fracture mechanisms, it is of interest to study the results further to assess how damage evolves in the plates. In particular, the growth of cracks through the thickness of the plates is thought to have a major influence on the global evolution of damage. Moreover, the effect of rebar on the crack evolution is of interest.

Table 9.6 shows the eroded elements of the cement matrices in the three mesoscale

simulations, during the first moments after the shock wave has hit the plates. As pointed out earlier, the bolt preload in the simulations causes a great deal of cracking in the plates prior to the blast load. It is seen that increasing the tensile strength of cement matrix reduces the amount of initial cracks, but large cracks are still present, and the damage in the middle of the plate is seen to increase. Much of the initial cracking is removed when rebar is included in the analysis, and only minor cracks have formed inside the bolt circles.

At 0.2 ms after the blast pressure has been applied to the plates, cracks have formed at their back surfaces. At this point, most of the cracks are shallow, and the least amount of damage is seen in the reinforced plate. For the reinforced plate and the plain plate with low cement matrix tensile strength, more cracks appear at 0.3 ms. The modified plain plate does not get more cracks, but the existing cracks grow in length and depth. At 0.5 ms, the final amount of cracks have also formed in the plain plate, and subsequent damage is caused by these cracks growing in depth. A different failure mechanism is seen in the reinforced plate, where instead new cracks continue to form throughout the first millisecond after the load starts, forming a much more intricate crack network than in the plain plates.

It is clear that the mesoscale method is too brittle, as crack growth initiates instantly, and there is no initial elastic response to speak of.

9.5 Summary and discussion

In this chapter, LS-DYNA has been used to simulate the experiments that were presented in Chapter 6. The simulations have been performed with different meshes, strain rate dependent concrete formulation, random element strength and direct modeling of the concrete mesostructure, with the goal of recreating the displacement history and crack patterns observed experimentally.

The study of mesh sensitivity showed that the K&C concrete damage model did not exhibit mesh dependent behavior when the plates were plain. This is likely attributed to the regularization scheme that is built into the K&C-model in LS-DYNA. For the reinforced plates, however, the response changed when the mesh was refined. Similar behavior was observed by Schwer [73], who studied the effect of changing the mesh size of concrete and rebar individually when modeling concrete plates subjected to blast loads. He found that meshing the rebar and concrete such that the nodes of the concrete and rebar meshes coincided reduced the mesh sensitivity when using the CLIS constraint in LS-DYNA. Hence, it is possible that refining the mesh of the rebar together with the concrete could remove the mesh dependent behavior that was observed in Section 9.1. Only the simulation of the plain plate at low pressure (P-41) correlated well with the experimental displacement history, while the other simulations were either too stiff (R-41), too soft (R-77) or predicted total collapse (P-77). The crack patterns obtained in the simulations were generally too excessive, but many of the simulated cracks coincided

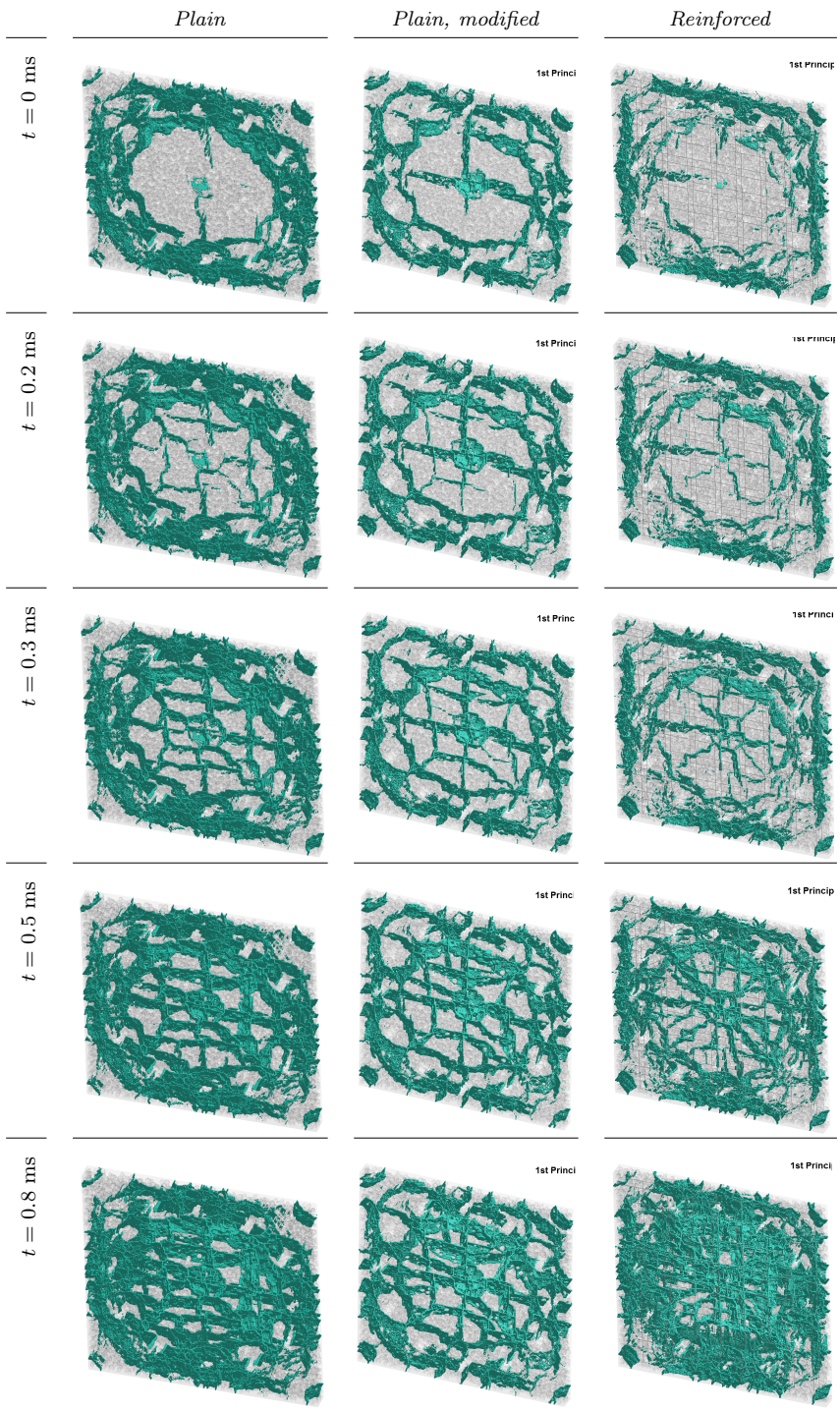

Table 9.6: *Crack growth in the mesoscale simulations.*

with the experiments. Overall, the simulations with uniform material without rate dependence overestimated the amount of damage inflicted to the plates, and did not accurately predict the displacement history. Judging from the damage alone, the simulations can be said to give a conservative estimate of the response of the plates, and fairly realistic crack patterns are predicted.

The strain rate dependence study showed that including the strain rate enhancement curve suggested in the LS-DYNA manual made the simulation results non-conservative, as the displacement history was under-predicted for both of the plain plates. At low pressure (P-41), the predicted crack pattern was also less severe than the experimental results. At high pressure (P-77), the correlation between the experimental and simulated crack pattern improved, but the displacement history was too stiff and did not resemble the experimental results.

Adding random element strength to the simulations did not alter the behavior of the plates substantially, and changing the spatial distribution of strong and weak elements within the concrete did not have a big impact on the simulated displacement history either. Still, the simulated crack patterns became more erratic and improved the correlation for some of the simulations. As mentioned in Section 8.4, however, the random element strength method may be better justified in simulations where the mesh is fully regular.

The simulations with a directly modeled concrete mesostructure did not correlate well with the experiments in that they developed excessive damage. Yet, the collapse mechanism looked surprisingly realistic. Moreover, the crack patterns predicted by the mesoscale method were highly erratic and featured many small discontinuous cracks, which was also observed in the experiments, albeit to a much lesser extent. The mesoscale simulations of reinforced concrete suffered from excessive element erosion at the pressurized surface of the plate, and the collapse mechanism did not look as realistic as in the plain plate simulation. A second simulation of the plain plate revealed that simply increasing the tensile strength of the cement matrix to that of the simulations with uniform concrete did not produce significantly different results. Therefore, it was concluded that a more comprehensive study of the tensile properties of the mesoscale method should be performed. It can also be argued whether it is correct to model the aggregates with much higher strength than the cement matrix, as the fracture surface from one of the tensile splitting tests (Figure 5.11) showed that only a small number of aggregates were undamaged. In fact, it may be more appropriate to model the aggregates with random strength and increasing the tensile strength of the matrix further.

In total, the simulations with uniform concrete provided mostly reasonable and conservative estimates of the amount of damage inflicted to the plates. As with the simulations in Abaqus, the solution became less accurate when the concrete was close to failure, and in LS-DYNA it was seen that small changes in the model set-up caused significant changes in the response. Several modifications were done to improve the accuracy of the simulations, but neither adding strain rate dependence

to the concrete model or including random element strength resulted in perfect correlation. The simulations with directly modeled mesostructure predicted excessive damage, but were promising in that they captured intricate crack patterns and failed in a physically reasonable way.

9.5.1 Hourglass control algorithms

In the process of running the simulations presented above, it was discovered that the standard viscous form LS-DYNA hourglass control algorithm generally gave a high percentage of hourglass energy in the simulations. There are several hourglass control formulations in LS-DYNA, and the severity of the control algorithm can be adjusted by changing the hourglass coefficient. A small study was conducted to assess the performance of some of the hourglass formulations, and an overview of the algorithms that have been used herein is given in Table 9.7.

ID	*Name*	*Default coefficient*
1	LS-DYNA viscous form	0.1
3	Flanagan-Belytschko viscous form with exact volume integration	-
4	Flanagan-Belytschko stiffness form	0.05*
5	Flanagan-Belytschko stiffness form with exact volume integration	0.05*

*Suggested value in LS-DYNA manual [75].

Table 9.7: *Hourglass control algorithms in LS-DYNA.*

To reduce the amount of hourglass energy, simulations of experiment P-41 with 10 mm element size were run with different hourglass control formulations and hourglass coefficients. The results from these simulations are shown in Figure 9.10. The viscous form hourglass controls gave a high fraction of hourglass energy and less stiffness than the fully integrated reference simulation. The peak in hourglass energy during the first millisecond is due to the bolt preload that is enforced at the beginning of the analysis. For the simulations with stiffness form hourglass control, the fraction of hourglass energy is consistently around 0.2, regardless of the hourglass coefficient. However, the stiffness of the solution varies greatly with the hourglass coefficient.

Since fully integrated elements are known to generally produce a too stiff response [20], the optimal response is probably a bit softer than the simulation with fully integrated elements. It is seen from the graph that a stiffness form hourglass control algorithm with an hourglass coefficient of less than 0.01 could perhaps be appropriate. However, this is much lower than the value of 0.05 suggested in the LS-DYNA manual, and it is therefore not known if this is advisable. Even though the default LS-DYNA viscous form hourglass control gave a high fraction of hourglass energy, the overall simulation results correlated well with the experiment for the P-41 experiment, but were too stiff for the reinforced plate at the same pressure.

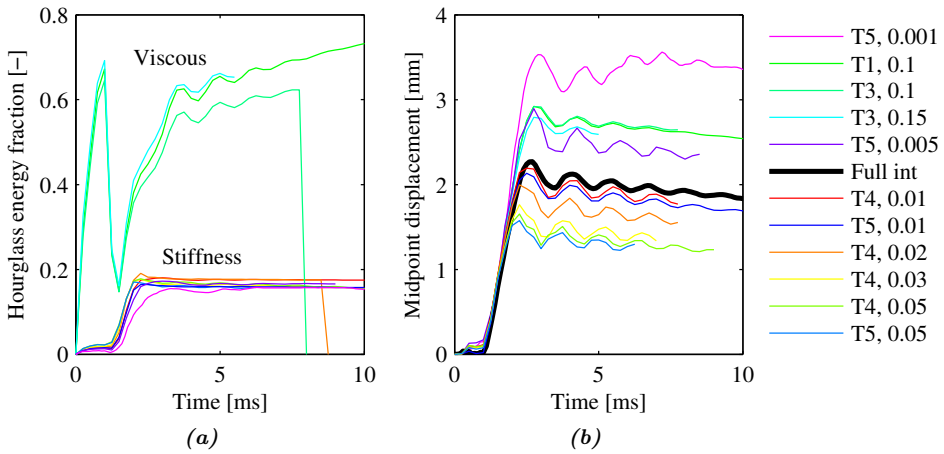

Figure 9.10: *The fraction of hourglass energy to internal energy for different hourglass control algorithms and coefficients are shown in (a), while (b) shows the resulting displacement curves. T1, T3, T4 and T5 in the legend refer to the type of hourglass control, see Table 9.7, and the following number indicate the hourglass coefficient.*

Hence, adding further stiffness to the solution would not improve the correlation of the simulations. Moreover, since the K&C-model is strain softening, there is no resistance to any deformation modes in the elements once the concrete has failed, so adding stiffness to the hourglass modes alone does not make sense.

From this small study, it is clear that choosing the correct hourglass control formulation for simulation of concrete structures is not trivial. Viscous formulations resulted in high fractions of hourglass energy in the simulations, while stiffness based formulations had large impact on the stiffness of the simulations. Based on the many uncertainties that are already present in the simulation of concrete, it is also difficult to conclude which hourglass formulation is most appropriate from comparison with the experiments. Hence, the only conclusion that can be made from this study is that hourglass energy may represent a significant challenge in simulations of blast-loaded concrete, and that dealing with this issue requires special attention from the analyst.

Chapter 10

Capacity Study

In the preceding analyses, the concrete plates have been simulated using different approaches to see how the experiments are best replicated. In the following chapter, the goal is rather to see how the capacity of the plates is predicted, and how the response changes at different loads. The effect of scaling the peak reflected pressure will be investigated, as well as the effect of changing the positive impulse while keeping the peak pressure constant.

10.1 Effect of pressure

From the experiments it is known that the plates should not fail when subjected to a shock wave equivalent to that of P-77 and R-77. Still, some of the simulations predicted total failure for these pressures. Furthermore, the analytical calculations of the simply supported plate in Section 7.1.2 predicted that no cracking should occur for static pressures lower than 7 and 7.5 bar for the plain and reinforced plates, respectively, while the elastic analysis in Abaqus in Section 7.2 predicted a cracking pressure of 6.5 bar for the plain plate. The questions to be answered is thus; when is cracking predicted by the CDP and K&C-models, and when is total collapse predicted?

To assess these questions, simulations of reinforced and plain plates have been conducted. The models with 5 elements over the thickness and uniform concrete have been employed in these simulations, and the Friedlander curve of P-41 has been scaled in pressure to represent different loads. Each model has been subjected to peak reflected pressures starting at 4 bar and increasing in 2 bar increments until failure occurred.

In the following, cracking has been defined as the point when the 1st principal strain exceeds 0.01 for a row of 4 consecutive elements. This definition is made so that the simulations can easily be classified into cracking or no-cracking. Furthermore,

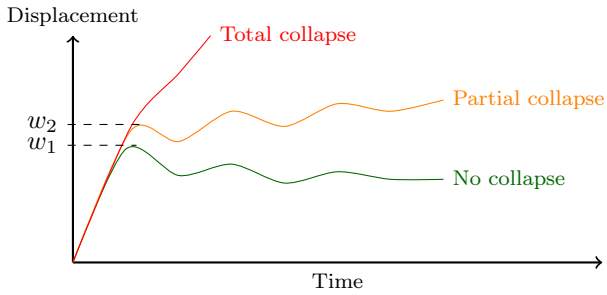

Figure 10.1: *Definition of collapse and maximum displacement.*

the definition of collapse is made as described in Figure 10.1. A partial collapse categorization has been added because many of the simulations exhibited a gradual transition into full collapse.

The simulation results from the LS-DYNA and Abaqus capacity studies are shown in Figure 10.2. In LS-DYNA, cracking is predicted to occur for peak reflected pressures between 8-9 bar for a plain plate, and between 10-11 bar for a reinforced plate. This prediction is slightly higher than the calculations in Chapter 7. Total collapse is predicted between 16-16.55 bar for an unreinforced plate and between 19-20 bar for a reinforced plate. This means that the simulation of P-77 in Section 9.1 was very close to not collapsing. The graphs also show that there is a transition in behavior once the concrete starts to crack. Before cracking occurs, the deformations are small and are approximately linearly increasing with the peak pressure. Once cracks have formed, the deformation increases at a higher rate with increasing peak pressure, before collapse occurs.

In Abaqus, cracking is predicted to occur for peak reflected pressures between 6-7 bar for a plain plate, and between 7-8 bar for a reinforced plate. Evidently, the responses predicted in Abaqus are closer to the analytical calculations in Chapter 7 than those obtained in LS-DYNA. However, a very high pressure, 25 bar in both plates, is required for the model to predict total collapse. Consequently, large displacements are predicted for both plates. In this sense, Abaqus predicts a much more ductile plate response than LS-DYNA. There is a fairly gradual transition in behavior between no cracks and crack occurrence in both plates, while a similar slight transition can be observed in the plain plate going from cracks to partial collapse.

In conclusion, the elastic calculations gave a reasonable estimate to the cracking pressures of the plates compared with the simulations in Abaqus and LS-DYNA, but Abaqus is more in agreement. A cracking pressure of around 7 bar seems reasonable, since one of the B45 concrete plates tested by Haug and Osnes developed some small cracks when subjected to a shock wave with a peak reflected pressure of 7.4 bar. The estimated collapsing pressures in Abaqus and LS-DYNA differ by almost 9 bar for the unreinforced plate. Since none of the plates tested in this

thesis collapsed, it is not known which is more correct. Still, by again comparing this with the test results from Haug and Osnes, a collapse pressure of 25 bar seems excessive. Haug and Osnes got total collapse at 29 bar peak pressure, and were very close to total collapse at 18.78 bar peak pressure. They used a concrete with a 4.14 MPa tensile splitting strength, so it should be expected that the B20 concrete in this thesis should fail at slightly lower peak pressures.

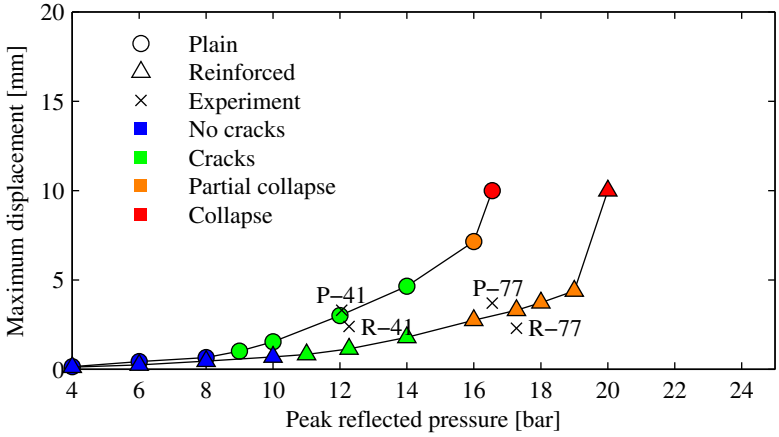

(a) LS-DYNA

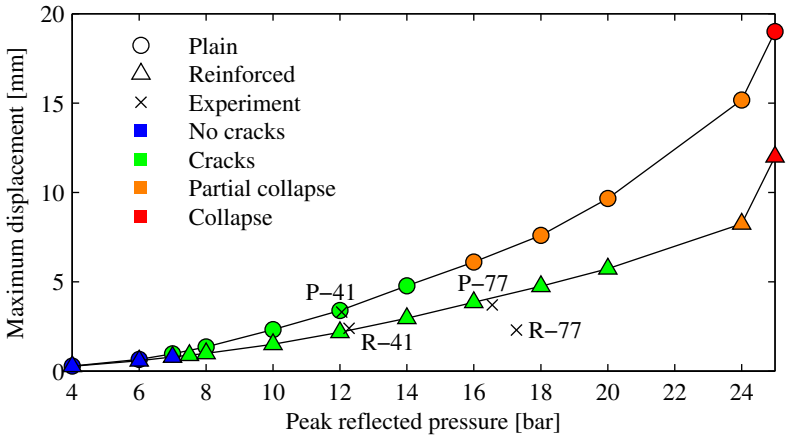

(b) Abaqus

Figure 10.2: *Maximum displacement versus peak reflected pressure on the plates, simulated in LS-DYNA with the K&C-model in (a), and in Abaqus with the CDP-model in (b). The shape of the markers indicate if the plate is plain or reinforced, while the color indicate the amount of damage to the plate.*

10.2 Effect of impulse

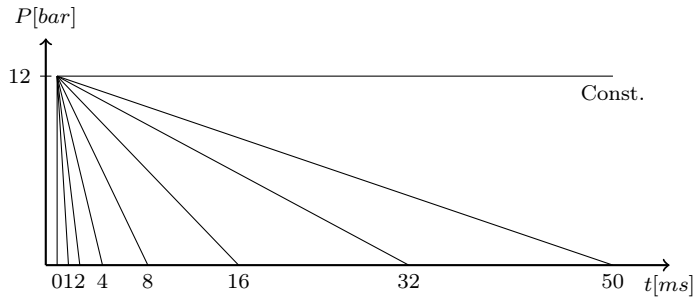

Figure 10.3: *Triangular loads used for the impulse study.*

In the analytical calculations in Section 7.1 it was found that the loading regime for the concrete plates in this study could be classified as quasi-static as long as the load duration was longer than at most 3.5 ms. Hence, according to the classification of loading regimes described in Section 3.1.4, the impulse of the load should not affect the response of the plates when the load duration is longer than 3.5 ms. Since these calculations were an upper bound estimate and assume perfectly elastic conditions and simply supported boundary conditions, it is of interest to see how much the impulse actually influences the response of the plates when the full shock tube clamping assembly is modeled using the K&C and CDP models for the concrete.

To study the effect of blast load impulse, simulations of the plain and reinforced plates have been performed with triangular loads of different durations, as seen in Figure 10.3. All simulations were performed with a peak load of 12 bar.

The simulation results are seen in Figure 10.4. Considering the simulations in LS-DYNA, it is clear that the response of the plates is not in the quasi-static domain for load durations just longer than 3.5 ms. In fact, the plain plate does not converge to the constant pressure solution at all for the load durations considered here, which indicates that the simulations in LS-DYNA are sensitive to the impulse. For the reinforced plate, however, the displacement converges to the quasi-static solution for load durations longer than around 20 ms.

In Abaqus, the results are quite different. Here, the limit of 3.5 ms does not seem that far off. At a load duration of only 10 ms, no change in response is seen for the plain plates, nor for the reinforced plates. These results are in good agreement with the blast load response theory discussed in Section 3.1.4.

The authors have not been successful in finding an explanation for the large deviation between the simulations in Abaqus and LS-DYNA, thus further studies on this matter should be conducted.

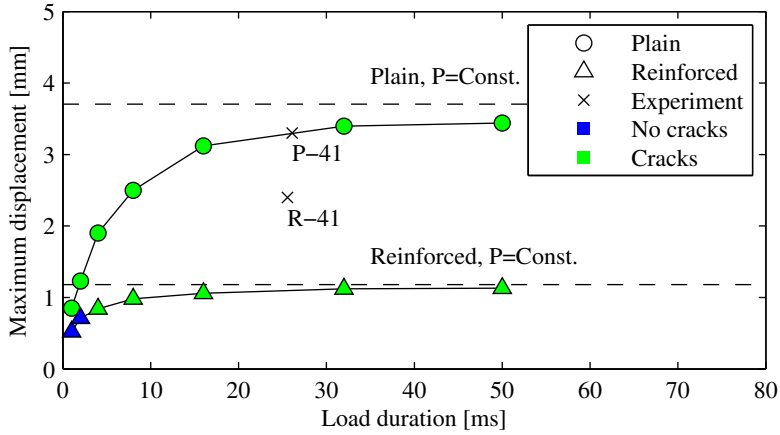

(a) LS-DYNA

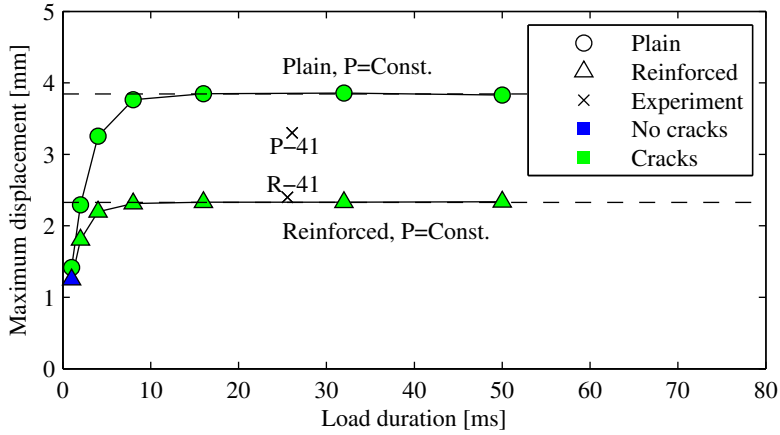

(b) Abaqus

Figure 10.4: *Maximum displacement versus load duration for plates subjected to triangular load pulses. The equivalent load duration of the experiments has been calculated by setting the impulse of the experiment equal to the impulse of a triangular pressure pulse, i.e.* $I_+ = \frac{1}{2} P_r t_d$, *and solving for* t_d.

Chapter 11

Concluding Remarks

The purpose of this thesis has been to examine how the behavior of concrete structures subjected to blast loads may be predicted. A comprehensive experimental study has been conducted, where concrete cubes, cylinders and beams have been tested in compression and tension, and concrete plates have been subjected to blast loads in the shock tube facility at SIMLab. The shock tube experiments have been filmed with a stereoscopic camera setup, such that 3D Digital Image Correlation (DIC) could be utilized to measure the deformation field of the plates during the blast loading. Moreover, the stochastic variation in concrete strength has been investigated by performing 20 cube compression tests.

The response of the concrete plates has been calculated analytically by thin plate theory and the yield line method. Elastic finite element analysis was also performed to study the boundary conditions of the concrete plates mounted in the shock tube. By inverse-modeling the material tests, the appropriate material input constants were found, before detailed numerical studies were initiated to assess the performance of the Concrete Damaged Plasticity (CDP) and Karagozian and Case (K&C) models in Abaqus and LS-DYNA, respectively, with regard to blast loaded plates. The effects of element size, element erosion, strain rate dependent material formulation, stochastically distributed element strength and mesoscale modeling of the concrete were studied with the goal of replicating the experimental results. Finally, it was looked into how the behavior of the plates would change under different loads, as predicted by the two finite element codes.

The main findings during the work of this thesis will be presented in the following.

Experimental Work

The material tests showed that significant variation was present in the strength between otherwise similar concrete specimens. From 20 cube compression tests, it was determined that the mean 28 day strength of the concrete was 46.35 MPa with

a standard deviation of 0.73 MPa, and even larger variations were observed in the tensile splitting tests. Cube compression tests were performed at 2, 7, 14, 28, 49 and 84 days after casting to establish the evolution of strength with ageing of the concrete, so that the ageing effect could be taken into account when simulating the concrete plates later.

The shock tube experiments were conducted on two plain and two reinforced plates at low and high blast pressures, and produced surprising results in that none of the plates collapsed or even developed through-cracks. Since experiments in a preceding Master's thesis on the subject experienced this with a stronger concrete mix and under similar test conditions, it was expected to occur also for the experiments in this thesis. Furthermore, it was observed that the reinforced plates were stiffer and developed less damage than the plain plates. A different displacement history was measured for the shock tube experiments at high blast pressures compared with the low pressure tests, for which no definite explanation could be presented. Moreover, it could not be explained that the two reinforced plates experienced almost no difference in damage and initial displacement, despite one being subjected to a significantly stronger blast load. Thus, while the shock tube experiments provided much valuable experimental data, a number of uncertainties were also present in the data.

Preliminary Analyses

From the analytical thin plate calculations, it was found that assuming fully clamped boundary conditions for the concrete plates in the shock tube would not be accurate, as this would entail more severe cracking at the front surface of the plates than was observed in the experiments. In fact, compared with a simulation of the full clamping assembly of the shock tube in Abaqus/Standard, it was seen that simply supported boundary conditions correlated better. Still, it was ultimately decided that the full clamping assembly would have to be included in order to accurately capture the boundary conditions. Additional analyses with these models were conducted in order to determine the pressure at which incipient cracking would occur, as well as characterizing the dynamic response of the plates. Moreover, the residual capacity of the reinforced plates after cracking was calculated by yield line theory, but this was found to be inapplicable to the problem at hand due to the small amount of damage that was achieved in the experiments.

The CDP and K&C material models were used to inverse-model the material tests in Abaqus and LS-DYNA, respectively. The material constants for the CDP model were found in the literature, and scaled accordingly to correlate with the concrete strength obtained in the physical tests, while the automatic parameter generation capability was used in the K&C-model. Simulations of the material tests showed that both models were able to represent the main features of the experiments, such as the confinement effect in cube compression, and that the tensile strength in a bending test is higher than in a tensile splitting test. From a qualitative view,

however, it was found that the post-peak load softening behavior of concrete was best represented by the CDP-model.

Two stochastic methods were programmed in order to capture the stochastic behavior observed in the material tests. The first method, dubbed the random element strength method, assigns a random strength to each element in a finite element mesh according to a normal distribution. By running sets of 20 simulations with random element strength, it could be determined which values of mean element strength and standard deviation reproduced the strength distribution seen in the cube compression tests. In this process, it was found that the relationship between element strength distribution and cube strength distribution was not straightforward, but that the weight of the left tail of the element strength distribution seemed to have a major influence on the mean cube strength. It was also found that the random element strength method had to be calibrated for each mesh size, and that finer meshes caused a more narrow cube strength distribution when the element strength distribution was kept constant. When the random element strength method was applied to the K&C-model it resulted in less ductile behavior, while no changes in post-peak response was observed when applied to the CDP-model. The second method, dubbed the mesoscale method, divides a finite element mesh into aggregates and cement, in an attempt to represent the physical mesostructure of the concrete directly. This method was able to recreate the experimental cube strength distribution, as well as produce remarkably intricate and physically reasonable crack patterns when the mesh was refined.

Simulations of Concrete Plates

Reasonable results were obtained from the simulations in both Abaqus and LS-DYNA. The extent of cracking was generally exaggerated, but many of the simulated cracks were in very good agreement with the experiments. In addition, the simulations were able to capture the difference in crack patterns due to rebar in the concrete. The simulated displacement histories were not in perfect correlation with the DIC measurements, but it was observed that better correlation prevailed for the low pressure simulations. Moreover, LS-DYNA was best at simulating plain concrete plates, while Abaqus was most accurate in simulating reinforced concrete. It is likely that this can be attributed to the strain softening regularization scheme in the K&C-model, and the lack thereof in the CDP-model. A simple strain based element erosion criterion was implemented in Abaqus, and this was seen to make it easier to assess the inflicted damage, at the cost of overly reducing the capacity of the plates. The effect of strain rate dependent material formulation was looked into in LS-DYNA, but the strain rate enhancement curve suggested in the LS-DYNA manual caused an overprediction in the strength of the plates.

Introducing random element strength caused little change in the simulated displacement histories of the plates, and also predicted no change in displacement with different spatial distributions of element strength. However, it was observed that the crack patterns became more erratic when random element strength was

included, which improved the correlation in some of the simulations. It was finally recognized that the random element strength method may be a useful tool to induce erratic crack patterns in simulations where a fully regular mesh is employed. The mesoscale simulations overestimated the damage inflicted to the plates, and thus showed that further work is needed to fully determine the tensile properties of the method. However, the results were still highly promising. In particular, the mesoscale method captured vastly intricate crack patterns and predicted realistic collapse mechanisms.

Finally, the predicted ultimate load capacity in both Abaqus and LS-DYNA was investigated. Incipient cracking was predicted to occur at around 7 bar of peak reflected pressure in Abaqus, which was in good agreement with the analytical and elastic calculations in the preliminary analysis. LS-DYNA predicted somewhat higher cracking pressures, but was more conservative in terms of the collapse pressure. Abaqus predicted much higher collapse pressures than LS-DYNA, and by comparison with previous tests in the Master's thesis by Haug and Osnes from 2015 [4], it was concluded that the collapse pressures predicted by LS-DYNA seemed the most realistic. The effect of changing the blast load impulse was also investigated, from which it was found that Abaqus was in good agreement with the theory of dynamic response to blast loads, while the simulations in LS-DYNA were not.

The simulations of concrete plates subjected to blast loads in Abaqus and LS-DYNA also showed that it was difficult to obtain optimal energy balances, as both codes experienced significant fractions of hourglass energy in the simulations. Different formulations of hourglass control were attempted in LS-DYNA to deal with the problem, but this affected the simulation results greatly. Hence, it seems that achieving acceptable energy balances is not straightforward when simulating concrete materials.

Chapter 12

Further Work

Further study of the mesoscale model. In the mesoscale model developed in this thesis, both the aggregate particles and the cement matrix were modelled using the K&C model. Since the mechanical properties of cement and rock can be very different, this approach may be too simple. In particular, the tensile properties of the mesoscale model are largely unknown. An interesting study would thus be to calibrate the mesoscale method after the material tests, and perhaps test different material models for the aggregate particles and the cement. Moreover, since the mechanical properties of the aggregate particles vary greatly, it would be interesting to implement stochastic variation of the aggregate strength in the mesoscale model. It could also be of interest to employ the mesoscale model in Abaqus.

Further study of the method of random element strength. This method proved to be very mesh sensitive, and must therefore be calibrated for each mesh. Consequently, more sophisticated approaches should be looked into, for instance imposing a probability field on the mesh instead of distributing element strength randomly. Weibull weakest link theory could also be interesting to study in this regard.

Conduct more three-point bending tests. A better statistical basis for the tensile properties of the concrete should be obtained. It would make more sense to calibrate a stochastic model with respect to the tensile properties of the concrete rather than the compressive properties, since the tensile strength is considered to be a critical parameter in the shock tube experiments.

Investigate the effect of erosion criteria. Excessive damage was seen in the simulations with erosion. The erosion criterion may be a critical variable in these simulations, and should therefore be studied further. More sophisticated criteria where multiple parameters are taken into account may be necessary when modelling fracture of blast loaded concrete.

Account for FSI in the simulations. The blast load can be modelled more

realistically by performing FSI simulations. This may have a substantial impact on the collapse sequence of the plates when element erosion is enabled.

Conduct more shock tube experiments. The shock tube experiments should be conducted at a wider range of pressures, in addition to testing several plates at the same pressure. This would create a better basis for comparison with the simulations. Furthermore, measuring the midpoint deflection of the plates with a laser would validate the displacement fields obtained from the DIC.

Perform more compression tests. In order to get a better understanding of the stochastic behavior of concrete with regards to the size of the sample, compression tests on cubes with different sizes could be performed. Moreover, it would be interesting to directly measure the stress-strain curves during compression, such that the simulation results can be better compared with real behavior.

Further investigation of the shock tube boundary conditions. There are still some uncertainties regarding the boundary conditions in the shock tube assembly. In order to obtain a more accurate description of the boundary conditions, the bolt preload should be measured, and the shock tube displacement should be measured with a laser.

Experiments with contact charges. The behavior of concrete subjected to contact charges should be investigated, as contact charges may potentially cause much local damage to the concrete walls of a submerged floating tunnel. The performance of the K&C and CDP-models is not known under such conditions, and should therefore be investigated.

Blast load experiments of concrete tubes. Scaled experiments of concrete tubes should be conducted. Simulations of the experiments could then be used to assess how well a material model predicts the response in more realistic blast load scenarios. Moreover, this would be a highly relevant experiment in regards to a submerged floating tunnel.

Include the shear rebar. A shear rebar was used in all of the concrete plates in the experiments. This has not been included in any of the models in the simulations, therefore it would be interesting to investigate the effect of including it in the simulations.

Bibliography

[1] Statens vegvesen, *Statusrapport, ferjefri E39*, 2015. Vegdirektoratet.

[2] Statens vegvesen/Vianova. http://www.vegvesen.no/vegprosjekter/ferjefriE39, [cited: 30.05.2016].

[3] Teknisk Ukeblad. http://www.tu.no/artikler/voldsom-brann-etter-eksplosjon-i-tunnel-i-bremanger/197007, [cited: 30.05.2016].

[4] S. R. Haug and K. Osnes, "Submerged floating tunnels subjected to internal blast loading," Master's thesis, Norwegian University of Science and Technology, Trondheim, Norway, 2015.

[5] F. Toutlemonde, P. Rossi, C. Boulay, C. Gourraud, and D. Guedon, "Dynamic behaviour of concrete: tests of slabs with a shock tube," *Materials and Structures*, vol. 28, no. 5, pp. 293–298, 1995.

[6] S. C. Woodson and J. T. Baylot, "Structural collapse: quarter-scale model experiments," tech. rep., DTIC Document, 1999.

[7] J. Magnusson and M. Hallgren, "Reinforced high strength concrete beams subjected to air blast loading," in *8th International Conference on Structures Under Shock and Impact, Iraklion, GREECE, MAR, 2004*, pp. 53–62, Wit Press, 2004.

[8] J. Magnusson, *Structural concrete elements subjected to air blast loading*. PhD thesis, KTH, 6 2007.

[9] A. Schenker, I. Anteby, E. Gal, Y. Kivity, E. Nizri, O. Sadot, R. Michaelis, O. Levintant, and G. Ben-Dor, "Full-scale field tests of concrete slabs subjected to blast loads," *International Journal of Impact Engineering*, vol. 35, no. 3, pp. 184 – 198, 2008.

[10] G. Thiagarajan, A. V. Kadambi, S. Robert, and C. F. Johnson, "Experimental and finite element analysis of doubly reinforced concrete slabs subjected to blast loads," *International Journal of Impact Engineering*, vol. 75, pp. 162 – 173, 2015.

[11] W. Wang, D. Zhang, F. Lu, S. chuan Wang, and F. Tang, "Experimental study and numerical simulation of the damage mode of a square reinforced concrete slab under close-in explosion," *Engineering Failure Analysis*, vol. 27, pp. 41 – 51, 2013.

[12] J. Li and H. Hao, "Numerical study of concrete spall damage to blast loads," *International Journal of Impact Engineering*, vol. 68, pp. 41 – 55, 2014.

[13] V. Aune, T. Børvik, and M. Langseth, *Impact Mechanics: An Introduction to Blast Mechanics*. Trondheim, Norway: Structural Impact Laboratory (SIMLab), 1 ed., 2015.

[14] P. W. Cooper, *Explosives Engineering*. Alberquerque, NM: Wiley-VCH, 1 ed., 1996.

[15] T. Krauthammer, *Modern Protective Structures*. the United States of America: CRC Press, 1 ed., 2008.

[16] C. N. Kingery and G. Bulmash, *Air blast parameters from TNT spherical air burst and hemispherical surface burst*. Ballistic Research Laboratories, 1984.

[17] Aune, Vegard, Børvik, Tore, and Langseth, Magnus, "Behaviour of plated structures subjected to blast loading," *EPJ Web of Conferences*, vol. 94, p. 01015, 2015.

[18] V. Aune, E. Fagerholt, M. Langseth, and T. Børvik, "A shock tube facility to generate blast loading on structures," *International Journal of Protective Structures, Special Issue on Blast Load Characterisation*, 2016.

[19] W. E. Baker, P. Cox, J. Kulesz, R. Strehlow, and P. Westine, *Explosion hazards and evaluation*. Elsevier, 1983.

[20] R. D. Cook, D. S. Malkus, M. E. Plesha, and R. J. Witt, *Concepts and Applications of Finite Element Analysis*. the United States: John Wiley & Sons, Inc., 4 ed., 2002.

[21] O. S. Hopperstad and T. Børvik, *Impact Mechanics: Material Behaviour and explicit FEM*. Trondheim, Norway: Structural Impact Laboratory (SIMLab), 1 ed., 2015.

[22] Z. Tu and Y. Lu, "Evaluation of typical concrete material models used in hydrocodes for high dynamic response simulations," *International Journal of Impact Engineering*, vol. 36, no. 1, pp. 132 – 146, 2009.

[23] Y. Wu, J. E. Crawford, and J. M. Magallanes, "Performance of LS-DYNA concrete constitutive models,"

[24] X. Lin, Y. Zhang, and P. J. Hazell, "Modelling the response of reinforced concrete panels under blast loading," *Materials & Design*, vol. 56, pp. 620 – 628, 2014.

[25] J. Lubliner, *Plasticity Theory*. Macmillan Publishing Company, 1990.

[26] O. S. Hopperstad and T. Børvik, *Materials Mechanics Part 1.* Trondheim, Norway: Structural Impact Laboratory (SIMLab), 1 ed., 2014.

[27] J. Lubliner, J. Oliver, S. Oller, and E. Onate, "A plastic-damage model for concrete," *International Journal of solids and structures*, vol. 25, no. 3, pp. 299–326, 1989.

[28] S. Murakami, *Continuum Damage Mechanics. A Continuum Mechanics Approach to the Analysis of Damage and Fracture.* Springer Science + Business Media B.V, 2012.

[29] R. E. Walpole, R. H. Myers, S. L. Myers, and K. Ye, *Probability and statistics for engineers and scientists, 9th edition*, vol. 9. Pearson Education, 2012.

[30] P. Mehta and P. J. Monteiro, *Concrete. Structure, Properties, and Materials.* Englewood Cliffs, New Jersey: Prentice-Hall, Inc., 2 ed., 1993.

[31] A. Neville, *Properties of Concrete.* Edinburgh Gate, Harlow: Pearson Education Limited, 4 ed., 1999.

[32] W.F.Chen, *Plasticity in Reinforced Concrete.* United States of America: McGraw-Hill, Inc., 1 ed., 1982.

[33] J. Weerheijm, *Understanding the tensile properties of concrete.* Sawston, Cambridge: Woodhead Publishing Limited, 4 ed., 2013.

[34] M. Pająk, "The influence of the strain rate on the strength of concrete taking into account the experimental techniques," 2011.

[35] C. A. Ross, D. M. Jerome, J. W. Tedesco, and M. L. Hughes, "Moisture and strain rate effects on concrete strength," *Materials Journal*, vol. 93, no. 3, pp. 293–300, 1996.

[36] L. J. Malvar and J. E. Crawford, "Dynamic increase factors for concrete," tech. rep., DTIC Document, 1998.

[37] T. Ngo, P. Mendis, A. Gupta, and J. Ramsay, "Blast loading and blast effects on structures - an overview," *Electronic Journal of Structural Engineering*, vol. 7, pp. 76–91, 2007.

[38] T. Børvik, O. S. Hopperstad, and M. Langseth, *Impact Mechanics: An Introduction to Penetration and Perforation Mechanics.* Trondheim, Norway: Structural Impact Laboratory (SIMLAB), 1 ed., 2015.

[39] Z. P. Bazant and J. Planas, *Fracture and size effect in concrete and other quasibrittle materials*, vol. 16. CRC press, 1997.

[40] L. J. Malvar, J. E. Crawford, J. W. Wesevich, and D. Simmons, "A Plasticity Concrete Material Model for DYNA3D," *International Journal of Impact Engineering*, vol. 19, pp. 847–873, 1 1997.

[41] J. M. Magallanes, Y. Wu, L. J. Malvar, and J. E. Crawford, "Recent improvements to release III of the K&C concrete model," in *11th International LS-DYNA Users Conference, Michigan (USA)*, pp. 3–37, 2010.

[42] J. Lee and G. L. Fenves, "Plastic-damage model for cyclic loading of concrete structures," *Journal of engineering mechanics*, vol. 124, no. 8, pp. 892–900, 1998.

[43] A. S. Genikomsou and M. A. Polak, "Finite element analysis of punching shear of concrete slabs using damaged plasticity model in abaqus," *Engineering Structures*, vol. 98, pp. 38–48, 2015.

[44] T. Tysmans, M. Wozniak, O. Remy, and J. Vantomme, "Finite element modelling of the biaxial behaviour of high-performance fibre-reinforced cement composites (hpfrcc) using concrete damaged plasticity," *Finite Elements in Analysis and Design*, vol. 100, pp. 47–53, 2015.

[45] Dassault Systémes, "Abaqus analysis user's guide."

[46] Dassault Systémes, "Abaqus theory guide."

[47] Standard Norge, *NS-EN 12350-2:2009 Testing fresh concrete - Part 2: Slump-test*, 2009.

[48] Standard Norge, *NS-EN 12350-7:2009 Testing fresh concrete - Part 7: Air content - Pressure methods*, 2009.

[49] Standard Norge, *NS-EN 12390-2:2009 Testing hardened concrete - Part 2: Making and curing specimens for strength tests*, 2009.

[50] European Standard, *Eurocode 2: Design of concrete structures - Part 1-1: General rules and rules for buildings*, 12 2004.

[51] Standard Norge, *NS-EN 12390-6:2009 Testing hardened concrete - Part 6: Tensile splitting strength of test specimens*, 2009.

[52] R. L. Taylor and S. Govindjee, "Solution of clamped rectangular plate problems," *Communications in numerical methods in engineering*, vol. 20, no. 10, pp. 757–765, 2004.

[53] E. H. Mansfield, *The bending and stretching of plates*. Cambridge University Press, 2005.

[54] R. C. Hibbeler, *Mechanics of materials*. Pearson, 2011.

[55] F. Irgens, *Formelsamling, mekanikk*. Tapir Akademisk Forlag, 1999.

[56] R. Park and W. L. Gamble, *Reinforced Concrete Slabs*. John Wiley & Sons, Inc., 2 ed., 2000.

[57] K. Johansen, "Beregning af krydsarmerede jernbetonpladers brudmoment," *BSM 3-1 Bygningsstatiske Meddelelser*, 1931.

[58] K. Johansen, *Pladeformler*. Copenhagen: Polyteknisk Forlag, 1968.

[59] S. I. Soerensen, *Betongkonstruksjoner. Armbert betong og spennbetong.* Trondheim: Tapir Akademisk Forlag, 2 ed., 2005.

[60] T. Jankowiak and T. Łodygowski, "Identification of Parameters of Concrete Damage Plasticity Constitutive Model," *Foundations of Civil and Environmental Engineering*, 2005.

[61] A. Caballero, C. López, and I. Carol, "3D meso-structural analysis of concrete specimens under uniaxial tension," *Computer Methods in Applied Mechanics and Engineering*, vol. 195, no. 52, pp. 7182 – 7195, 2006. Computational Modelling of Concrete.

[62] Z. P. Bazant, M. R. Tabbara, M. T. Kazemi, and G. Pijaudier-Cabot, "Random particle model for fracture of aggregate or fiber composites," *Journal of engineering mechanics*, vol. 116, no. 8, pp. 1686–1705, 1990.

[63] P. Grassl, D. Grégoire, L. R. Solano, and G. Pijaudier-Cabot, "Meso-scale modelling of the size effect on the fracture process zone of concrete," *International Journal of Solids and Structures*, vol. 49, no. 13, pp. 1818–1827, 2012.

[64] X. Wang, Z. Yang, J. Yates, A. Jivkov, and C. Zhang, "Monte carlo simulations of mesoscale fracture modelling of concrete with random aggregates and pores," *Construction and Building Materials*, vol. 75, pp. 35–45, 2015.

[65] E. Syroka-Korol, J. Tejchman, and Z. Mróz, "FE investigations of the effect of fluctuating local tensile strength on coupled energetic-statistical size effect in concrete beams ," *Engineering Structures*, vol. 103, pp. 239 – 259, 2015.

[66] R. M. Brannon, J. M. Wells, and O. E. Strack, "Validating theories for brittle damage," *Metallurgical and Materials Transactions A*, vol. 38, no. 12, pp. 2861–2868, 2007.

[67] P. Grassl and Z. P. Bažant, "Random lattice-particle simulation of statistical size effect in quasi-brittle structures failing at crack initiation," *Journal of engineering mechanics*, vol. 135, no. 2, pp. 85 – 92, 2009.

[68] S. Eckardt, S. Häfner, and C. Könke, "Simulation of the fracture behaviour of concrete using continuum damage models at the mesoscale," 2004. In Proceedings of ECCOMAS 2004, Jyväskylä.

[69] L. Shuguang and L. Qingbin, "Method of meshing {ITZ} structure in 3D meso-level finite element analysis for concrete," *Finite Elements in Analysis and Design*, vol. 93, pp. 96 – 106, 2015.

[70] Y. Tai, T. Chu, H. Hu, and J. Wu, "Dynamic response of a reinforced concrete slab subjected to air blast load," *Theoretical and applied fracture mechanics*, vol. 56, no. 3, pp. 140–147, 2011.

[71] K. Xu and Y. Lu, "Numerical simulation study of spallation in reinforced concrete plates subjected to blast loading," *Computers & Structures*, vol. 84, no. 5, pp. 431–438, 2006.

[72] H. Jiang and M. G. Chorzepa, "An effective numerical simulation methodology to predict the impact response of pre-stressed concrete members," *Engineering Failure Analysis*, vol. 55, pp. 63–78, 2015.

[73] L. E. Schwer, "Modeling Rebar: The Forgotten Sister in Reinforced Concrete Modeling," in *13th International LS-DYNA conference*, 2014.

[74] Livermore Software Technology Corporation (LSTC), *LS-DYNA Keyword User's Manual, Volume 2*. Livermore Software Technology Corporation, 2015.

[75] Livermore Software Technology Corporation (LSTC), *LS-DYNA Keyword User's Manual, Volume 1*. Livermore Software Technology Corporation, 2015.

Appendices

Appendix A

Concrete data

A.1 Concrete receipt

NorBetong A/S avd. Heggstadmyra
Heggstadmyra 6
7080 Heimdal

Tel.: 815 11 302
W..: www.norbetong.no - @..: svein.nisja@norbetong.no

Følgeseddel opplysninger

Flgsdl: **377499** Dato: **25-01-2016 14:04:54**
K/P: **1011160 - NTNU Felles fakturamottak / 160591 - RICHARD BIRKELANDSV 1 A (KONST**
Bil: **2160**
Type: **Almindelig resept** Synkmål: **210 mm**
Satse: **1** Satsstr: **1,00** Prod m³: **1,00**
VC forhold: **0,670** Flg m³: **1,00/(1,002)** Standard: **NS206**
Resept: **203200 B20 M90 D16 25%RED FA+SIL P/SP**

Vekt sats opplysninger

Materiale Ønsket mat/silo i 1. sats fra resepten	Silo	**Sats 1** Ønsket	Sats korr.	Oppnådd	Afvikelse %	FUKT %	Vanninnhold	**Less** Ønsket	Oppnådd	Afvikelse %
RAMLO 0-8	1	1196		1172		6,30[M]	68,89	1196	1172	-2,00
RAMLO 8-16	4	703		691		0,80[M]	5,46	703	691	-1,69
RAMLO 0-2	6	85		83		5,00[M]	3,92	85	83	-2,25
Tilslag total		1984		1946	**-1,90**			1984	1946	**-1,90**
Norcem Standard FA	2	276,1		305,9				276,1	305,9	**10,77**
Kaldt vann	1	0,00		**0,00**			0,00	0,00	0,00	0,00
Varmt vann	2	70,28		69,11			69,11	70,28	69,11	-1,66
Slamvann	1	23,99		22,47		84,08[M]	18,89	23,99	22,47	-6,35
Vann total		94,27		91,58	**-2,86**			94,27	91,58	**-2,86**
Rescon Dynamon SR-N	3	2,105		2,100	**-0,25**		1,69	2,105	2,100	**-0,25**
Skyllevann		13,0		**13,0**			13,00	13,0	13,0	
Ekstra vann				9,0			9,00		9,0	
Total Kg		**2370**		**2368**			**189,95**	**2370**	**2368**	

Utefinerede Kg Satsnr.	Tilslag	Sement	Vann	Tilset. 2	Slamvann
1	4,88	1,83	2,20	0,18	4,88
Ialt	4,88	1,83	2,20	0,18	4,88

Øvrige sats opplysninger

	Blander				
Satsnr.	Blandetidspedvann	Efter anta	Wattmeter	Blander	Temperatur
Ønsket	60,0				21,0
1	88,0	32,7	11,0	Blander 1	22,6

Øvrige less opplysninger

	Ønsket	Oppnådd	Afvikelse
VC-Forhold	0,670	0,621	-0,049
Totale kg i less	2370	2368	-0,1
Frit vann	185,00	189,95	2,7 %
Ekv.cem.mengde	276,12	305,86	10,8 %

Tørstof (EN1008)		Oppnådd	
Tørstof Kg (Ukendt materiale)		3,58	Kg
Tørstof / Tilslag forhold	Krav <1,00%	0,19	%

NorBetong A/S avd. Heggstadmyra
Heggstadmyra 6
7080 Heimdal

Tel.: 815 11 302
W..: www.norbetong.no - @..: svein.nisja@norbetong.no

BRÅNEL

NS-EN 206:2013+NA:2014

	Oppnådd ialt	Pr. m³	Ikke godkendt
Max. VC-Forhold:	0,621		Ok (Krav:0,900)
Min. fiberindhold:	0,000		Ok (Ingen krav)
Min. Ekvivalent sementinnhold:	305,861	304,858	Ok (Krav:225,00)
Max. Klorid/Pulver forhold:	0,070		Ok (Krav:0,100)
Max. alkali innhold:	4,611		Ok (Krav:7,023)
SCC robusthed nedre tolerance:	4,952		Ok (Ingen krav)
SCC robusthed øvre tolerance:	4,952		Ok (Ingen krav)
Sil% av Cem ved CEM I:	0,000		Ok (Ingen krav)
Sil% av Cem ved CEM II/A-V:	0,000		Ok (Ingen krav)
Min. sement SV (c):	305,861	304,858	Ok (Ingen krav)
Flyveaske/pulver forhold:	0,180		Ok (Krav:0,350)
Silika/pulver forhold:	0,000		Ok (Krav:0,110)

Doseringtoleranse:	Tilslag : Afvikelse fra ønsket : -1,90% (Krav 3,49%)	Ok
	Norcem Standard FA Doseringstoleranse overskredet : 10,77% > 3,49%	
	Vann : Afvikelse fra ønsket : -2,86% (Krav 3,49%)	Ok
	Rescon Dynamon SR-N : Afvikelse fra ønsket : -0,25% (Krav 5,49%)	Ok

Bemerkninger

Feiltype	Bruker	Dato	Bemerkning
Dos.tol.(less) Vekt ,Silo 2 - Norcem Standard FA Doseringstoleranse overskredet : 10,77% > 3,49%			

A.2 Concrete test results

			Density		*Strength*	
Test	*Test type*	*Age* [days]	*Demould* [kg/m^3]	*Testing* [kg/m^3]	f_c [MPa]	f_t [MPa]
1	C	29	2387.1	2407.2	40.55	-
2	C	29	2431.8	2451.7	40.15	-
3	C	29	2414.2	2432.0	39.90	-
4	C	29	2427.1	2445.1	38.90	-
5	C	29	2449.0	2467.6	38.59	-
6	TS	29	2408.6	2377.8	-	4.06
7	TS	29	2402.7	2422.9	-	3.63
8	TS	29	2393.4	2413.3	-	3.43
9	TS	29	2401.5	2421.1	-	3.36
10	TS	29	2417.5	2435.7	-	3.04

C - Uniaxial compression
TS - Tensile splitting

Table A.1: *Density and strength of concrete cylinders tested in compression and tensile splitting.*

		Density		
Test	*Age* [days]	*Demould* [kg/m^3]	*Testing* [kg/m^3]	f_c [MPa]
1	2	-	-	25.53
2	2	-	-	25.27
3	2	-	-	26.04
4	7	-	-	37.63
5	7	-	-	36.66
6	7	-	-	37.03
7	14	-	-	42.28
8	14	-	-	43.27
9	14	-	-	43.39
10	28	2425.6	2442.7	46.86
11	28	2427.3	2443.9	46.78
12	28	2421.4	2440.4	46.54
13	28	2432.5	2451.1	46.52
14	28	2410.1	2428.2	45.49
15	28	2430.2	2450.5	46.55
16	28	2434.3	2453.3	45.76
17	28	2431.1	2450.5	46.24
18	28	2405.4	2425.3	46.31
19	28	2430.4	2448.8	46.97
20	28	2435.6	2453.8	48.15
21	28	2430.4	2450.5	46.63
22	28	2413.0	2433.0	45.84
23	28	2444.1	2463.3	46.92
24	28	2426.9	2444.3	46.14
25	28	2429.0	2448.0	46.18
26	28	2426.6	2446.6	47.01
27	28	2408.8	2429.6	44.66
28	28	2422.1	2442.9	45.16
29	28	2429.7	2449.0	46.28
30	49	2414.3	2434.3	49.05
31	49	2436.2	2455.9	49.54
32	49	2422.2	2443.1	48.66
33	49	2433.5	2453.7	49.15
34	49	2422.9	2445.4	49.05
35	84	2421.1	2441.9	55.96
36	84	2413.8	2436.1	57.51
37	84	2394.4	2416.3	55.61

Table A.2: *Density and strength of concrete cubes tested in compression.*

Appendix B

Simulation input data

B.1 Concrete Damaged Plasticity material data

E [MPa]	υ	ρ [kg/mm^3]	β	m	f	γ
19700	0.19	2.36E-009	38°	1	1.12	0.666

Table B.1: *Concrete elasticity and CDP parameters.*

Stress [MPa]	*Crushing strain* [-]	*Damage* [-]	*Crushing strain* [-]
15.0	0.0	0.0	0.0
20.197804	0.0000747307	0.0	0.0000747307
30.000609	0.0000988479	0.0	0.0000988479
40.303781	0.000154123	0.0	0.000154123
50.007692	0.000761538	0.0	0.000761538
40.236090	0.002557559	0.195402	0.002557559
20.236090	0.005675431	0.596382	0.005675431
5.257557	0.011733119	0.894865	0.011733119

Table B.2: *Compression hardening and damage data.*

Stress [MPa]	*Cracking strain* [-]	*Damage* [-]	*Cracking strain* [-]
1.99893	0.0	0.0	0.0
2.842	0.00003333	0.0	0.00003333
1.86981	0.000160427	0.406411	0.000160427
0.862723	0.000279763	0.69638	0.000279763
0.226254	0.000684593	0.920389	0.000684593
0.056576	0.00108673	0.980093	0.00108673

Table B.3: *Tension stiffening and damage data.*

Appendix C

Code

C.1 VUSDLFD user subroutine

```
      subroutine vusdfld(
! Read only variables
     . nblock, nstatev, nfieldv, nprops, ndir, nshr,
     . jElem, kIntPt, kLayer, kSecPt,
     . stepTime, totalTime, dt, cmname,
     . coordMp, direct, T, charLength, props,
     . stateOld,
! Write only variables
     . stateNew,field)
      include 'vaba_param.inc'
!      implicit double precision (a-h,o-z)
!      parameter (j_sys_Dimension = 2)
!      parameter( n_vec_Length = 544  )
!      parameter( maxblk = n_vec_Length  )
      dimension jElem(nblock),coordMp(nblock,*),direct(nblock,3,3),
     .          T(nblock,3,3),charLength(nblock),props(nprops),
     .          stateOld(nblock,nstatev),stateNew(nblock,nstatev),
     .          field(nblock,nfieldv)
      character*80 cmname
c
      real*8 straindata(maxblk*(ndir+nshr))
      integer jSData(maxblk*(ndir+nshr))
      character*3 cPData(maxblk),cSData(maxblk*(ndir+nshr))
      integer jStatus
      real*8 PE(nblock,6)
      real*8 tr,e1,e2,e3,e4,e5,e6,f1,f2,f3,f4
      real*8 epsp1(nblock),epsp1crit
      integer failactive
!-----------------------------------------------------------------------
!     Read material properties
!-----------------------------------------------------------------------
      epsp1crit  = props(1)
```

```
      failactive = props(2)
!-----------------------------------------------------------------------
!     Call history variables
!-----------------------------------------------------------------------
      call vgetvrm(  'PE', straindata,jSData,cSData,jStatus)
!-----------------------------------------------------------------------
!     Extract data
!-----------------------------------------------------------------------
      do k=1,nblock
         PE(k,1) = straindata(k)
         PE(k,2) = straindata(k+nblock)
         PE(k,3) = straindata(k+nblock*2)
         PE(k,4) = straindata(k+nblock*3)
         PE(k,5) = straindata(k+nblock*4)
         PE(k,6) = straindata(k+nblock*5)
      enddo
!-----------------------------------------------------------------------
!     Compute principal plastic strains
!-----------------------------------------------------------------------
      do k=1,nblock
         tr = (PE(k,1)+PE(k,2)+PE(k,3))*one3
         e1 = PE(k,1)-tr
         e2 = PE(k,2)-tr
         e3 = PE(k,3)-tr
         e4 = PE(k,4)
         e5 = PE(k,5)
         e6 = PE(k,6)
         f1 = 0.5d0*(e1*e1+e2*e2+e3*e3)+e4*e4+e5*e5+e6*e6
         f2 = e1*e5*e5+e2*e6*e6+e3*e4*e4-e1*e2*e3-2.0d0*e4*e5*e6
         f3 =-sqrt(27.d0/f1)*f2*0.5/f1
         f3 = sign(min(abs(f3),1.0d0),f3)
         f4 = acos(f3)/3.0
         epsp1(k) = tr+2.0*sqrt(f1/3.0)*cos(f4)
      enddo
!-----------------------------------------------------------------------
!     Check if erosion criterion is met
!-----------------------------------------------------------------------
      do k=1,nblock
         if((epsp1(k).gt.epsp1crit).and.(failactive.eq.1))then
            stateNew(k,nstatev) = 0
         else
            stateNew(k,nstatev) = 1
         endif
      enddo
!-----------------------------------------------------------------------
!     End of subroutine
!-----------------------------------------------------------------------
      return
      end
```

C.2 Statistical variation code for Abaqus

```
%%%%%%%%%%%%%%%%%%%%%%%%%%%%%%%%%%%%%%%%%%%%%%%%%%%%%%%%%%%%%%%%%%%%%%%%%%%%%%%%
% This script modifies an Abaqus input file such that a statistical dist- %
% ribution of element strength is incorporated. This includes the creati- %
% on of N different materials, the creation of material sets and element  %
% sets                                                                    %
%%%%%%%%%%%%%%%%%%%%%%%%%%%%%%%%%%%%%%%%%%%%%%%%%%%%%%%%%%%%%%%%%%%%%%%%%%%%%%%%

N =20; %Number of materials
s = 50; %Strength
var = 60; %Variation in strength, 6x std.dev [MPa]

% Scaling parameters
S = 50;
base_strength = 50;
new_strength = 50;
str_frac = new_strength/base_strength;

% Assign 'tension' or 'compression' to variate either the tensile or
% compressive strength
LOAD_TYPE = 'compression';

fid = fopen('STATISTIKK.inp','r'); %Old input file
fid2 = fopen('terning_statistisk.inp','w'); %Modified input file
i=1; %Counter
while ~feof(fid)
    a = fgetl(fid);

    % Materials
    if ~isempty(regexp(a,'*Material,','ONCE'))
        i=1;
        matvec{i,1} = a;
        i=i+1;
        a = fgetl(fid);
        while i<40      %Read material card
            matvec{i,1} = a;
            i=i+1;
            a = fgetl(fid);
        end
        for j=1:N       %Define materials
            fracX = str_frac*((s-(var/2)+var*(j-1)/(N-1))/s);
            FRAC(j)=fracX*S;
            for k=1:i-1
                format long
                if k==1
                    if j>9
                        matvec{k,1}(41:42) = num2str(j);
                    else
                        matvec{k,1}(41) = num2str(j);
                    end
                    fprintf(fid2,'%s\n',matvec{k,1})
                else

                    % Compression hardening
```

```
if strcmp(LOAD_TYPE,'compression') == 1
    if k > 8 && k < 17
        NumSwap1 = str2num((matvec{k,1}(1:8)))*fracX;
        NumSwap2 = str2num((matvec{k,1}(10:21)))*fracX;
        StrSwap1 = num2str(NumSwap1);
        StrSwap2 = num2str(NumSwap2);
        if isinf(1/NumSwap1)
            StrSwap1 = '0.';
        end
        if isinf(1/NumSwap2)
            StrSwap2 = '0.';
        end
        fprintf(fid2,'%s, %s\n',StrSwap1,StrSwap2)
    elseif k > 24 && k < 33
        NumSwap1 = str2num((matvec{k,1}(1:8)));
        NumSwap2 = str2num((matvec{k,1}(10:22)))*fracX;
        StrSwap1 = num2str(NumSwap1);
        StrSwap2 = num2str(NumSwap2);
        if isinf(1/NumSwap1)
            StrSwap1 = '0.';
        end
        if isinf(1/NumSwap2)
            StrSwap2 = '0.';
        end
        fprintf(fid2,'%s, %s\n',StrSwap1,StrSwap2)

    else
        fprintf(fid2,'%s\n',matvec{k,1})
    end

% Tension hardening
elseif strcmp(LOAD_TYPE,'tension') == 1
    if k > 17 && k < 24
        NumSwap1 = str2num((matvec{k,1}(1:8)))*fracX;
        NumSwap2 = str2num((matvec{k,1}(10:22)))*fracX;
        StrSwap1 = num2str(NumSwap1);
        StrSwap2 = num2str(NumSwap2);
        if isinf(1/NumSwap1)
            StrSwap1 = '0.';
        end
        if isinf(1/NumSwap2)
            StrSwap2 = '0.';
        end
        fprintf(fid2,'%s, %s\n',StrSwap1,StrSwap2)
    elseif k > 33 && k < 40
        NumSwap1 = str2num((matvec{k,1}(1:8)));
        NumSwap2 = str2num((matvec{k,1}(10:22)))*fracX;
        StrSwap1 = num2str(NumSwap1);
        StrSwap2 = num2str(NumSwap2);
        if isinf(1/NumSwap1)
            StrSwap1 = '0.';
        end
        if isinf(1/NumSwap2)
            StrSwap2 = '0.';
        end
        fprintf(fid2,'%s, %s\n',StrSwap1,StrSwap2)
    else
```

```
                        fprintf(fid2,'%s\n',matvec{k,1})
                    end
                else
                    error('ASSIGN LOAD TYPE!!');
                end
            end
        end
    end

% Sections
elseif ~isempty(regexp(a,'*Solid Section, elset=matset-1','ONCE'))
    i=1;
    secvec{i,1}=a;
    i=i+1;
    a = fgetl(fid);
    while i<3
        secvec{i,1} = a;
        i=i+1;
        a = fgetl(fid);
    end             % Read section card
    for j=1:N       % Define sections
        for k=1:i-1
            if k==1
                if j>8
                    secvec{k,1}(30:31) = num2str(j+1);
                    secvec{k,1}(32) = ',';
                    if j == 9
                        secvec{k,1}(66) = num2str(j);
                    else
                        secvec{k,1}(66:67) = num2str(j);
                    end
                else
                    secvec{k,1}(30) = num2str(j+1);
                    secvec{k,1}(66) = num2str(j);
                end
            end
            fprintf(fid2,'%s\n',secvec{k,1})
        end
    end

% Elements
elseif ~isempty(regexp(a,'*Element, type','ONCE'))
    i = 1;
    elevec{i,1} = a;
    fprintf(fid2,'%s\n',a);
    i = i+1;
    a = fgetl(fid);
    while isempty(regexp(a,'*Nset,','ONCE'))
        fprintf(fid2,'%s\n',a);
        elevec{i,1} = a;
        element_nodes(i,:) = str2num(elevec{i}(6:end));
        i=i+1;
        a = fgetl(fid);
    end       % Read Element card.
elseif ~isempty(regexp(a,'*Elset, elset=matset-1,','ONCE'))
    i = 1;
    elsetvec{i,1} = a;
```

```
fprintf(fid2,'%s\n',a);
i = i+1;
a = fgetl(fid);
fprintf(fid2,'%s\n',a);

els = str2num(elevec{end,1}(1:5));              % Find #elements
[nd,EleSet,PlotInput] = ElementSet(els,N);      % Call EleSet matrix
[row,col] = size(EleSet);

% Create element matrix
for i = 1:col
    for j = 2:row
        if (EleSet(j,i)) == 0
            break
        else
            element = num2str(EleSet(j,i));
            element(length(element)+1:length(element)+2)=', ';
            ELEMENT{j,i} = element;
        end
    end
end

% Write elements
for i = 1:col

    % Set names
    MatNum = EleSet(1,i);
    linje = '*Elset, elset=matset-';
        if MatNum > 8
            linje(22:23) = num2str(MatNum+1);
        else
            linje(22) = num2str(MatNum+1);
        end
    fprintf(fid2,'%s\n',linje);

    % Assign elements to sets
    x = 2;
    teller = 0;
    while ~isempty(ELEMENT{x,i})        % Break condition
        if teller > 10
            fprintf(fid2,'%s\n',ELEMENT{x,i})
            teller = 0;
        else
            fprintf(fid2,'%s',ELEMENT{x,i})
        end
        teller = teller + 1;
        x = x+1;

        % Safety break condition if while condition violates matrix
        % size
        if str2double(ELEMENT{x-1,i}) == EleSet(end,i)
            break
        end
    end
    fprintf(fid2,'%s\n','')
end
a = fgetl(fid);
```

```
    end
    fprintf(fid2,'%s\n',a)

end


% This function creates the EleSet matrix. Each column represent a
% material, wherein the numbers indicate the elements assigned  to
% the given material. The first row of the matrix indicates the material
% number.
%
% Input:    els — number of elements
%           N — number of materials
%
% Output:   EleSet — the element set matrix.


function [nd,EleSet,PlotInput] = ElementSet(els,N)

nd = ceil(normrnd(N/2,N/6,[els,1]));

if max(nd) > N
  index = find(nd > N);
  for i = 1:length(index)
      nd(index(i),1) = N;
  end
end
if min(nd) < 1
  index = find(nd < 1);
  for i = 1:length(index)
      nd(index(i),1) = 1;
  end
end

for i = 1:N
    numbering = find(nd == i);
    if isempty(numbering)
        EleSet(:,i) = 0;
    else
        for j = 1:length(numbering)
            EleSet(j+1,i) = numbering(j);
        end
    end
    EleSet(1,i) = i;
    PlotInput(i)=length(numbering);
end
end
```

C.3 Mesoscale generation code

```
%%%%%%%%%%%%%%%%%%%%%%%%%%%%%%%%%%%%%%%%%%%%%%%%%%%%%%%%%%%%%%%%%%%%%%%%%%%%%%%%
% This script generates a mesostructure for a concrete %
% plate and divides a regular FE-mesh into aggre-      %
% gates and cement matrix                              %
%%%%%%%%%%%%%%%%%%%%%%%%%%%%%%%%%%%%%%%%%%%%%%%%%%%%%%%%%%%%%%%%%%%%%%%%%%%%%%%%
% Load matrices containing nodal positions and element connectivity.
% A separate script reads the FE-input file and generates these matrices.
load meshdata.mat;
% Define geometry of the concrete plate
L = 625e-3; %Plate length [m]
B = 625e-3; %Plate width [m]
H = 50e-3;  %Plate thickness [m]
% Define minimum and maximum aggregate radius
rmin = 4e-3; %Min radius [m]
rmax = 8e-3; %Max radius [m]
% Calculate volume of plate and define desired volume fraction of
% aggregates.
V=L*B*H; %Volume of plate [m^3]
V_fr_max=0.35; %Desired volume fraction of aggregates [-]
%Set reinforcement wire diameter and positions
r_rc = 1.25e-3;
rx = [-0.24059 -0.1671 -0.0936 -0.02009 0.05341 0.13021 0.20041 0.27451] + 0.5*L;
ry = [-0.240416 -0.166916 -0.0934161 -0.0199161 0.053584 0.130384 ...
    0.200584 0.275084] +0.5*B;
rz = [0.09325 0.05675]-H;
%Preallocate and set counters
agg=[];
miss=0;
V_fr=0;
k=1;
%% Start aggregate generation
while miss<100 && V_fr <V_fr_max
    %Calculate random position
    x = rmin + rand(1,1)*(L-2*rmin);
    y = rmin + rand(1,1)*(B-2*rmin);
    z = rmin + rand(1,1)*(H-2*rmin);
    tmp = [x y z];
    %Calculate wall clearance
    wall_clear = [x, L-x, y, B-y, z, H-z];
    %Calculate reinforcement clearance
    rcx = abs(rx-x);
    rcy = abs(ry-y);
    rcz = abs(rz-z);
    proj_x = sqrt((min(rcx))^2 + (min(rcz))^2);
    proj_y = sqrt((min(rcy))^2 + (min(rcz))^2);
    % Place first aggregate
    if k==1
        agg(k,:) = [tmp, min([min(wall_clear), rmax])];
        k=k+1;
        continue
    end
    % Calculate clearance to other aggregates
    for i = 1:length(agg(:,1))
```

```
        mindist(i) = sqrt(sum((agg(i,1:3)-tmp).^2)) - agg(i,4);
    end
    % Calculate the smallest clearance
    md = min(mindist);
    mw = min(wall_clear);
    mp = min(proj_x, proj_y)-r_rc;
    mvec=[md, mw, mp];
    [ma, mpos] = min(mvec);
    % Place aggregate
    if ma>rmax %Dmax aggregate does not interfere with anything
        agg(k,:)=[tmp, rmax];
        k=k+1;
        miss=0;
    elseif ma>rmin % Dmin aggregate does not interfere with anything
        agg(k,:) = [tmp, mvec(mpos)];
        k=k+1;
        miss=0;
    else % Dmin aggregate interferes -> reject aggregate
        miss=miss+1;
        continue
    end
    % Calculate current volume fraction
    V_agg = 0;
    for i = 1:length(agg(:,1))
        V_agg = V_agg + 4/3*pi*agg(i,4).^3;
    end
    V_fr = V_agg/V;
end
%% End of aggregate generation algorithm
% Correct for different CSYS in FE-model and aggregate system
elpos(:,1) = elpos(:,1)+0.5*L;
elpos(:,2) = elpos(:,2)+0.5*B;
elpos(:,3) = elpos(:,3)-H;
%% Calculate which elements are inside the aggregates
agg_elm =[]; %This matrix contains all the elements that are aggregates
for i = 1:length(agg(:,1))
    % Calculate distance from each aggregate to all elements
    el_dist = sqrt((elpos(:,1)-agg(i,1)).^2 + (elpos(:,2)-agg(i,2)).^2 ...
    +(elpos(:,3)-agg(i,3)).^2) - agg(i,4);
    % Find elements with negative distance
    el_clust{i,1} = find(el_dist<=0);
    % Add elements to aggregate element matrix
    agg_elm=[agg_elm; el_clust{i,1}];
end
%% Generate new input file with mesostructure
trig=0;
% Open original input file
fid = fopen('mesh_plate.k','r');
% Make new input file
fid2 = fopen('Plate_modified.k','w');
while ~feof(fid)
    a = fgetl(fid);
    % Duplicate original input-file until element card is reached
    if ~isempty(regexp(a,'*ELEMENT','ONCE')) &&~trig
        trig=true;
        fprintf(fid2,'%s\n',a);
        a = fgetl(fid);
```

```
        fprintf(fid2,'%s\n',a);
        a = fgetl(fid);
        i=1;
        while i<(eln+1) %Loop through all elements of concrete part
            i=i+1;
            if ~isempty(find(agg_elm==i-1))
                a(16) = num2str(2); %Assign PID=2 for aggregate
            else
                a(16) = num2str(1); %Assign PID=1 for cement matrix
            end
            fprintf(fid2,'%s\n',a);  % Print line to input file
            a=fgetl(fid);
        end
        fprintf(fid2,'%s\n',a);
    else
        fprintf(fid2,'%s\n',a);
    end
end
% Close input files
fclose(fid);
fclose(fid2);
```